Numerical modelling of intra-wave sediment transport on sandy beaches using a wave-resolving, non-hydrostatic model

Giulia Mancini

Thesis submitted to the University of Nottingham
for the degree of Doctor of Philosophy

September 2021

Abstract

The mutual feedback between the swash zone and the surf zone is known to affect morphodynamic processes, such as breaker bars formation and migration on sandy beaches. To resolve this feedback in a process-based manner, the morphodynamics in the swash zone and due to swash-swash interactions must be explicitly solved, e.g., by using wave-resolving numerical models. Currently, few existing models are able to resolve the complex morphodynamics in the swash zone of sandy beaches, and none is practically applicable for engineering practice. Wave-resolving models can be depth-averaged or depth-resolving. The former type requires lower computational cost compared to the latter one, therefore, it is preferred for engineering purposes.

This research work aims at improving the numerical modelling of the intra-wave sediment transport on sandy beaches, and in turn, of the exchange of sediments between the swash and surf zones under extreme events (e.g., storms, clusters of storms and tsunamis). A non-hydrostatic, wave-resolving model based on the open-source depth-averaged Non-hydrostatic XBeach framework is developed. An intra-wave advection-diffusion equation for the suspended sediment concentration, including erosion and deposition rates, is newly implemented in the model. A wave breaking-generated turbulence model together with a near-bed turbulence model are also developed. The effects of turbulence are included in both the hydrodynamics and sediment transport governing equations by means of the bed shear stress modelling.

The newly implemented sediment transport and wave breaking-induced turbulence models are verified with a semi-analytical solution and existing laboratory experiments, respectively. The hydro-morphodynamics model herein proposed is then validated with data of laboratory experiments for three test cases. The first two case studies consist of simulating i) bichromatic waves groups and ii) consecutive, isolated solitary waves over sloped sandy beaches. In the former swash-swash interactions are clearly present. The third test case involves plunging breaking waves over a barred sandy beach.

Numerical results show an improvement in the prediction of the intra-wave sediment transport, and in turn, of bed changes, especially in the swash zone with respect to the

available sediment transport formulations in Non-hydrostatic XBeach. However, the process of the breaker bar development is not accurately predicted yet by the model herein developed. In particular, results indicate that for monotonic sloping beaches the model performs better when the initial bed profile is closer to the equilibrium compared to an initial uniform sloped bed. Instead, for different bed configurations, e.g., where a long bore-like propagation is allowed to develop, the proposed model shows a poor response in terms of velocity and morphodynamics modelling. The need of including additional physical processes to better capture the sediment transport in addition to the lack of modelling processes that have a vertical structure (i.e., vertical structure of the flow and sediment concentration) are highlighted in this thesis.

Acknowledgements

I would like to take the opportunity to acknowledge all the people that helped me to reach this important milestone, for the time and knowledge that they generously shared with me. I wish to express my extreme gratitude to my supervisor, Dr. Riccardo Briganti, who gave me the opportunity to undertake this PhD study, for guiding me through this journey and always believing in me. My gratitude also goes to my second supervisor, Prof. Nicholas Dodd, for his helpful suggestions and encouragement he provided at every stage. I would like to thank my internal assessor, Dr. Valentin Heller, for his valuable advice and feedback throughout these years, especially during the annual reviews. I also would like to thank my external assessor, Dr. Giovanni Besio, for accepting to review this PhD thesis. I wish to thank Dr. Robert McCall who supervised my work alongside the Department of Applied Morphodynamics at Deltares, the Netherlands. I value his precious insights and ongoing help. I am also thankful to all the people of the Department of Applied Morphodynamics for their warm welcome when I arrived in Delft; I enjoyed the stimulating time I spent at Deltares. I would like to thank Dr. Fangfang Zhu for her helpful suggestions. I also would like to thank Dr. Francesco Enrile for his help with the XBeach model compilation.

Additionally, I would like to acknowledge the funding for this research from the University of Nottingham. I wish to thank all the people of the Environmental Fluid Mechanics and Geoprocesses (EFMG) research group. It has been a pleasure to be part of this group and I enjoyed the stimulating discussions we had throughout these years. My gratitude goes also to my colleagues from the C1 and C2 rooms for the shared time and for making the office a pleasant place. I am thankful to my long-time friends, and to the new friends from all around the world that I met in Nottingham and Delft for giving me the chance to explore new cultures. In particular, I wish to thank my friends, Gioele, Florentia, Aziz, Maha and Vladimir, for being always there for me. I also would like to thank Joshua and Ravshan for being my little family in Nottingham. I wish to express my endless gratitude to my parents, my sister and my grandma, because I would never have reached this point without them. Last but not least, I would like to thank Fabrizio, who crossed my path in Nottingham three years ago, for being always by my side and showing me the world from his perspective.

Author's declaration

The present thesis was written during my PhD study at the University of Nottingham, UK as a member of the Environmental Fluid Mechanics and Geoprocesses (EFMG) research group within the Faculty of Engineering.

This study was financed with the aid of the Vice Chancellor's Scholarship for Research Excellence from the University of Nottingham and of the Faculty of Engineering, the University of Nottingham.

The Non-hydrostatic extension to the XBeach model, including the XBeach-G for gravel beaches, was primarily developed by Dr. P. Smit, Dr. M. Zijlema, Prof. G. Stelling and Dr. Robert McCall. In this study new subroutines and additional parts to the original code, regarding the wave-resolving sediment transport, wave breaking-induced turbulence and the horizontal viscosity modelling, have been implemented and validated for applications on sandy beaches.

Laboratory data reported in this thesis from the Coupled high frequency measurements of Swash Sediment transport and Morphodynamics (CoSSedM) project were collected at the wave flume at the Universitat Politecnica de Catalunya, Barcelona, Spain, as part of the European Community's Seventh Framework Programme through the grant of the Integrating Activity HYDRALAB IV within the Transnational Access Activities; contract no. 261520. Laboratory data were provided by Dr. Yin Lu Young and Dr. Heng Xiao for the consecutive, non-interacting solitary waves. Laboratory data reported in this thesis from the Sand Transport under Irregular and Breaking Wave Conditions (SINBAD) project, jointly sponsored by the Engineering and Physical Sciences Research Council (EPSRC, EP/J00507X/1, EP/J005541/1) in the UK and by STW (12058) in the Netherlands, were provided by Dr. Dominic A. Van Der A.

Relevant scientific seminars and conferences were attended at which the ongoing work was presented. A first-author paper has been published in a refereed journal as well as a first-author conference proceeding.

First-authour journal publication:

Mancini, G., Briganti, R., McCall, R., Dodd, N., Zhu, F., 2021. Numerical modelling of intra-wave sediment transport on sandy beaches using a non-hydrostatic, wave-resolving

model. *Ocean Dynamics*, 71(1), 1-20.

First-author conference proceedings:

Mancini, G., Briganti, R., Ruffini, G., McCall, R., Dodd, N., Zhu, F., 2020. Analysis of the performance of different sediment transport formulations in Non-Hydrostatic XBeach. *Coastal Engineering Proceedings*, (36v), 35-35.

Posters and conference presentations:

Virtual "International Conference of Coastal Engineering" (ICCE). *Oral presentation.* October 2020.

"Engineering Showcase", the University of Nottingham, UK. *Three Minutes Thesis (3MT) presentation.* May 2020.

Virtual "Young Coastal Scientists and Engineers Conference" (YCSEC). *Oral presentation.* April 2020.

"Engineering Showcase", the University of Nottingham, UK. *Poster presentation.* Outcome: runner-up. May 2019.

"Delft Software Days", Deltares, the Netherlands. *Oral presentation.* November 2018.

Scholarships:

"BESTS: Building Experience and Skills Scholarship", Graduate School, the University of Nottingham, UK. 2018.

"Vice Chancellor's Scholarship for Research Excellence", the University of Nottingham, UK. 2017.

Table of Contents

List of Figures

List of Tables

Notation

Units of the variables or parameters are given in [ ]; for dimensionless symbols a hyphen is left between the brackets; when multiple units are possible, an asterisk is left between the brackets.

Latin

$A_{b,s}$	[-]	Bed load and suspended load coefficient in XBNH-WAST
A_R	[L^2]	Roller volume per unit width
B	[-]	Rouse number
c	[L/T]	Wave celerity
C	[L^3/L^3]	Depth-averaged suspended sediment concentration
c_f	[-]	Dimensionless friction coefficient
$c_{f,ref}$	[-]	Reference dimensionless friction coefficient
cov	[*]	Covariance
C_{eq}	[L^3/L^3]	Total equilibrium concentration
$C_{eq,b}$	[L^3/L^3]	Bed load equilibrium concentration
$C_{eq,s}$	[L^3/L^3]	Suspended load equilibrium concentration
C_{max}	[L^3/L^3]	Maximal suspended sediment concentration
C_{nb}	[L^3/L^3]	Near-bed suspended sediment concentration
C_s	[-]	Smagorinsky's constant
C_z	[L^3/L^3]	Parametric vertical sediment concentration
d	[L]	Still water depth
d_{nb}	[L]	Near-bed reference height
d'_{nb}	[L]	Dimensionless near-bed reference height
d_z	[L]	Vertical distance above the bed
D	[L/T]	Deposition rate
D_b	[L^3/T^3]	Wave energy dissipation rate due to wave breaking
D_C	[L/T]	Sediment diffusion coefficient
D_f	[L^3/T^3]	Wave energy dissipation rate due to bed friction
D_r	[L^3/T^3]	Roller energy dissipation rate
D_w	[L^3/T^3]	Total wave energy dissipation rate
D_{50}	[L]	Median grain diameter

E	[L/T]	Erosion rate
E_k	[L/T]	Erosion rate including TKE effects
E_r	[L^3/T^2]	Roller kinetic energy normalised by density
E_w	[L^3/T^2]	Wave energy normalised by density
f_g	[T^{-1}]	Wave group frequency
f_1	[T^{-1}]	First component primary wave frequency
f_2	[T^{-1}]	Second component primary wave frequency
F_w	[L^4/T^3]	Flux of wave energy
g	[L/T^2]	Gravitational acceleration
h	[L]	Total water depth
H	[L]	Wave height
H_{rms}	[L]	Root-mean-square wave height
H_1	[L]	First component primary wave height
H_2	[L]	Second component primary wave height
K_C	[-]	Shape factor
k	[L^2/T^2]	Depth-averaged wave breaking-generated TKE
k_b	[L^2/T^2]	Near-bed wave breaking-generated TKE
$k_{b_{tot}}$	[L^2/T^2]	Total near-bed wave TKE
k_w	[L^{-1}]	Wave number
l_m	[L]	Mixing length
L	[L]	Wave length
m_{cr}	[-]	Slope of the surface roller
m_e	[L/T]	Mobility parameter
n	[-]	Manning's coefficient
n_p	[-]	Bed porosity
$n_{p,d}$	[-]	Bed porosity for a fluidised bed
N	[-]	Number of samples
p_h	[L^2/T^2]	Normalised hydrostatic pressure
p_{nh}	[L^2/T^2]	Normalised dynamic pressure
p_{tot}	[L^2/T^2]	Normalised total pressure
q_b	[L^3/L/T]	Sediment transport rate for bed load
q_s	[L^3/L/T]	Sediment transport rate for suspended load

q_{sed}	[L^3/L/T]	Sediment transport rate
q_{tot}	[L^3/L/T]	Total sediment transport rate
$q_{tot,mean}$	[L^3/L/T]	Wave-averaged total sediment transport rate
Q	[L^2]	Sediment volume per unit width for RMSTE
R	[-]	Exponent in Pritchard and Hogg (2003)
s_{y_m}	[*]	Standard deviation of the modelled quantity
$s_{y_{ref}}$	[*]	Standard deviation of the reference quantity
S_{sl}	[-]	Bed slope effects term
$Sink_k$	[-]	Sink term in the TKE balance equation
$Source_k$	[-]	Source term in the TKE balance equation
t	[T]	Time
t_f	[T]	Final time
t_i	[T]	Initial time
T_g	[T]	Wave group period
T_{pr}	[T]	Mean primary wave period
T_r	[T]	Repeat period
T_s	[T]	Adaptation time in XBNH-WAST
u	[L/T]	Depth-averaged cross-shore flow velocity
u_{mean}	[L/T]	Wave-averaged depth-averaged cross-shore flow velocity
u_{ref}	[L/T]	Reference scale velocity
u_{rms}	[L/T]	Orbital root-mean-square wave velocity
u_*	[L/T]	Friction velocity
w	[L/T]	Vertical flow velocity
w_s	[L/T]	Sediment settling velocity
x	[L]	Cross-shore coordinate
x_0	[L]	Model upstream boundary cross-shore coordinate
y_m	[-]	Modelled quantity
y_{ref}	[-]	Reference quantity
z	[L]	Vertical coordinate
z_b	[L]	Bed level
z_{b_f}	[L]	Final bed level
$z_{b_{f,m}}$	[L]	Modelled final bed level for RMSTE

$z_{b_{f,ref}}$	[L]	Reference final bed level for RMSTE

Greek

α_{br}	[-]	Local surface steepness in the HFA
α_{sl}	[-]	Calibration coefficient for bed slope effects
β	[-]	Dissipation coefficient in the roller energy model
β_{br}	[-]	Secondary local surface steepness in the HFA
γ_d	[-]	Decay coefficient in the KW92-A09 turbulence model
γ_k	[-]	Calibration factor in bed shear stress modelling
γ_l	[-]	Mixing length coefficient
γ_1	[-]	Calibration factor in XBNH-WAST
γ_2	[-]	Calibration factor in XBNH-WAST
δ_R	[L]	Roller thickness
Δ	[-]	Relative density
Δt	[T]	Computational time interval
Δt_{SEG2}	[T]	Duration of SEG2
Δx	[L]	Computational x-grid size
Δz_b	[L]	Bed changes
Δz_{b_f}	[L]	Final bed changes
$\Delta z_{b_{SEG2}}$	[L]	Difference between final and initial bed level of SEG2
η	[L]	Water surface elevation
η_{cr}	[L]	Critical surface elevation in the R13 turbulence model
θ	[-]	Shields parameter
θ_{cr}	[-]	Critical Shields parameter
θ_k	[-]	Shields parameter including TKE effects
κ	[-]	von Karman constant
λ	[L]	Reference length scale
μ	[-]	Numerical parameter in the S13 viscosity model
ν_h	[M/L/T]	Horizontal viscosity
$\nu_{h,s}$	[M/L/T]	Smagorinsky's horizontal viscosity
ρ	[M/L^3]	Water density
ρ_{mr}	[-]	Pearson's cross-correlation coefficient

ρ_s	[M/L^3]	Sediment density
τ_b	[M/L/T^2]	Total bed shear stress
$\tau_{b,cr}$	[M/L/T^2]	Critical bed shear stress
$\tau_{b,k}$	[M/L/T^2]	Total bed shear stress including TKE effects
τ_{ref}	[M/L/T^2]	Reference bed shear stress
ϕ	[-]	Generic mathematical function
ϕ_t	[-]	Phase shift in Nielsen (2002)
ω_{rep}	[M/L]	Representative wave angular velocity
Ω	[-]	Dean's number

Abbreviations

ACVP	Acoustic Concentration and Velocity Profilers
ADV	Acoustic Doppler Velocimeter
AWG	Acoustic Wave Gauge
BBL	Bottom Boundary Layer
BC	Boundary Condition
BE1_2	Broad-banded wave condition
BE4_2	Narrow-banded wave condition
CCM+	Conducivity Concentration Measurements
CN	Courant Number
CoSSedM	Coupled high frequency measurements of Swash Sediment transport and Morphodynamics
DS	Distance Sonic
HFA	Hydrostatic Front Approximation
IWST	Intra-Wave Sediment Transport
K42-P45	Kolmogorov (1942)-Prandtl (1945) viscosity model
KW92-A09	Kobayashi and Wurjanto (1992)-Alsina et al. (2009) turbulence model
LDA	Laser-Doppler Anemometer
MOC	Method Of Characteristics
NLSWE	Non Linear Shallow Water Equations
nRMSE	normalised Root-Mean-Square Error

OBS	Optical Back-Scattering sensor
RMSTE	Root-Mean-Square Transport Error
R13	Reniers et al. (2013) turbulence model
SEG	Segment
SINBAD	Sand Transport under Irregular and Breaking Wave Conditions
S13	Smit et al. (2013) viscosity model
TKE	Turbulent Kinetic Energy
WG	Wave Gauge
WAST	Wave-Averaged Sediment Transport
XBH	Hydrostatic XBeach
XBNH	Non-Hydrostatic XBeach
ZD15	Zhu and Dodd (2015)
1DH	One-dimensional horizontal
2DH	Two-dimensional horizontal
3D	Three-dimensional

1 Introduction

1.1 Context and motivations

Sandy beaches evolution plays a key role in the coastal vulnerability, influencing the stability of ecosystems and coastal communities economy and safety. The behaviour of sandy beaches in terms of accretion and erosion processes is very complex. According to recent estimates, 24% of the world's sandy beaches are affected by chronic erosion driven by natural and anthropogenic causes of varying time and spatial scales (Luijendijk et al., 2018). Extreme forcing conditions, such as storms, the presence of coastal structures in the littoral zone, and climate change are some of the causes of shoreline changes. However, beaches morphological evolution and response to drivers, such as the increased frequency of storms, remain difficult to predict (see e.g., Coco et al., 2014; Wong et al., 2014; Ciavola and Coco, 2017). The shape of the beach profile determines the vulnerability of the coast to storms and the extent of the beach that can be used for habitat and recreation. Beach profile monitoring provides important information to assess if a shoreline is eroding or accreting, and consequently, the amount of erosion during a storm and how the beach recovers after those events.

The evolution of a beach profile is the result of the cross-shore sediment transport. In this context breaker bars, which can develop during storms, behave as a natural mechanism for the beach protection. These morphological features play a crucial role in the large amount of sediment which is exchanged during extreme events between the swash zone (see Fig. 1.1), which is the region of the beach where waves run up (uprush phase) and run down (backwash phase), and the offshore area.

Figure 1.1: Maccarese Lido, Fiumicino (Rome), Italy. The picture shows a swash uprush approaching the shore.

For this reason, numerical models are essential tools to predict the morphological evolution of beaches. In particular, process-based models are representations of the physical processes occurring in coastal regions, and therefore, they should provide the most realistic results. However, few existing models are able to resolve the complex morphodynamics of the nearshore zone, including the shoreline, which requires a wave-by-wave modelling approach, and none is applicable for engineering practice.

Wave-resolving models are of two types: depth-averaged and depth-resolving models. At present, validation of the latter type of models is limited to relatively simple wave and morphodynamics conditions, or to a limited coastal area mainly by simulating laboratory experiments (e.g., Jacobsen et al., 2014; Jacobsen and Fredsoe, 2014; Li et al., 2019; Kim et al., 2019; Larsen et al., 2020), because of the high computational effort required. On the other hand, depth-averaged models are the most widely used wave-resolving models by coastal engineers. The lack of a fully three-dimensional description of the velocity profile makes this type of models less computationally demanding. However, as the reader can see in Chapter 2, their modelling has not been sufficiently tested and understood for the swash zone of sandy beaches, and more comprehensively, for the mutual feedback between the swash zone and the surf zone.

For the aforementioned reasons, the present study wants to use a depth-averaged wave-resolving framework to model the intra-swash dynamics, and in turn, the morphological evolution of sandy beaches using computing resources that are widely accessible in the engineering community. A validated process-based wave-resolving model able to predict the shoreline evolution and the beach profile development under storms conditions can help coastal managers to decide what measures can be adopted to reduce the impact of such storms and maintain coastal safety. More general, multidisciplinary and comprehensive approaches for climate change risk assessment and adaptation processes are necessary, and an accurate impact modelling is required in such approaches (Toimil et al., 2020).

1.2 Aims and objectives

The overall aim of this work is to improve the numerical modelling of intra-swash dynamics, and in turn, the simulation of the sediment exchange between the swash and surf zones on sandy beaches. In particular, this work aims at developing a numerical

model, which is able to simulate the cross-shore intra-wave sediment transport, and in turn, the morphodynamic evolution of sandy beaches profiles at time-scales of storms for research and engineering practice.

The aforementioned aims are pursued by means of the following objectives:

- to improve a depth-averaged non-hydrostatic, wave-resolving framework (e.g., open-source Non-hydrostatic XBeach, Smit et al., 2010) in order to represent the complexity of the swash zone and its mutual feedback with the surf zone (e.g., to simulate the process of breaker bars development);
- to verify the performance and robustness of the developed model against semi-analytical solutions from the literature and experimental studies;
- to model relevant engineering scenarios by simulating laboratory experiments involving representative wave conditions in order to compare numerical results with measurements;
- to compare the morphodynamic response of the improved model with the available sediment transport formulations in the selected framework.

1.3 Thesis outline

Chapter 1 provides the research context and motivations, and presents the aims and objectives, which are developed in the following chapters.

Chapter 2 presents a review of the main hydro-morphodynamics processes in the surf and swash zones on sandy beaches and a focus on the breaker bars development. This chapter also discusses the state of the art of wave-resolving hydro-morphodynamics numerical models.

Chapter 3 describes the numerical methodology adopted in this study by presenting the governing equations used in the improved model, which now solves the intra-wave sediment transport and wave breaking-generated turbulence.

Verification of the aforementioned equations implemented in the selected framework against a semi-analytical solution and experimental data is described in Chapter 4.

Chapter 5 presents three validation tests for the developed model. Two of them involve solitary waves (i.e., isolated waves) and waves trains, where swash-swash inter-

actions are present, over sloped sandy beaches; the third test case concerns the hydro-morphodynamic modelling of regular waves over a barred sandy beach.

Finally, the discussion of results and final conclusions with recommendation for future works are presented in Chapters 6 and 7, respectively.

2 Literature review

2.1 Introduction

This chapter presents a literature review of the main hydro-morphodynamic processes in the surf and swash zones on sandy beaches that contribute to the cross-shore sediment transport, and in turn, to the beach profile development at short time scales, e.g., storms, clusters of storms and tsunamis (see Fig. 2.1). Following the review, the state of the art of wave-resolving hydro-morphodynamics models applied to the nearshore region is reported.

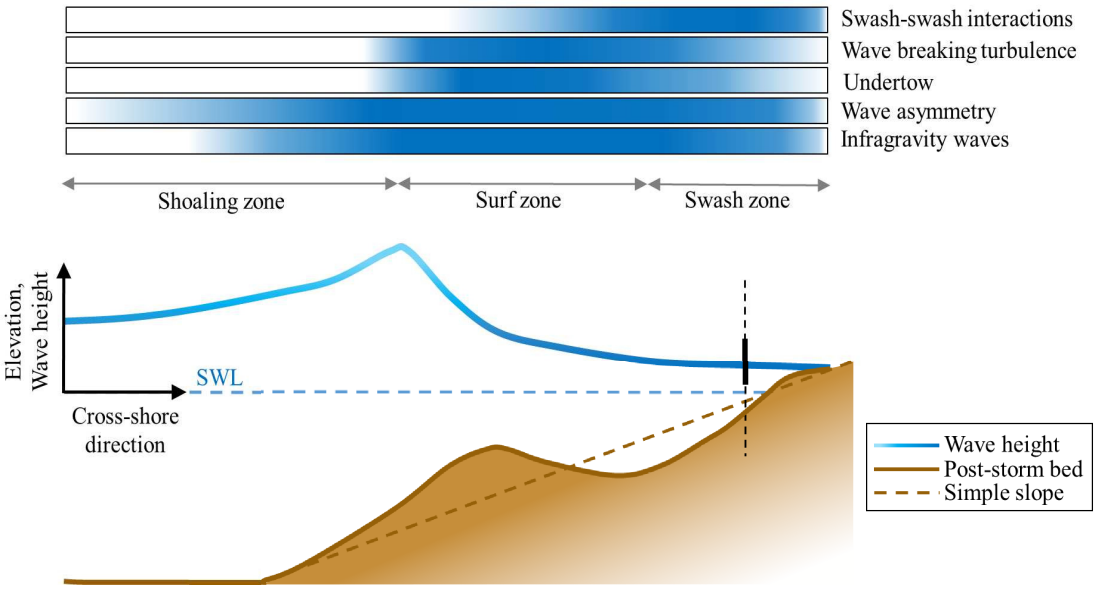

Figure 2.1: Schematisation of a barred beach profile under storm conditions and the main mechanisms contributing to the beach evolution. The intensity of the colour of the bar chart indicates the relative influence of each mechanism throughout the cross-shore direction; the solid-dashed line indicates a cross-shore location in the swash zone, and its dynamics are shown in Fig. 2.2.

Nearshore waves mobilise a significant amount of sediment, and therefore, they are the driving forces for beach erosion and accretion. As waves propagate shoreward into a decreasing water depth, their interactions with the sediment bottom become stronger. In the shoaling zone, before breaking, waves tend to steepen due to non-linear effects, while frequency dispersion counteracts this steepening. The initially sinusoidal waves shape develops into horizontally asymmetric profiles (skewness) with high, narrow crests and long, flat troughs. In this region, turbulence is mostly generated by wave friction with the bed, which is restricted to the near-bed boundary layer. The frictional force

expended by the flow per unit area of bed is expressed as bed shear stress. On non-flat beds the total bed shear stress is determined by two contributions, which are the skin-friction component produced by the sediment grains and the form drag component due to the pressure field acting on bedforms, such as ripples. As waves propagate to shallower water, they transform into pitched forward profiles (vertical asymmetry), until they become unstable and break in the surf zone. Wave breaking generates a reduction of wave energy and production of turbulence, with an increasing amount of suspended sediment. Broken waves propagate shoreward as bores (i.e., surface rollers), allowing significant sediment transport. Once bores reach the shore, they run up on the beach and then, retreat after reaching the maximum excursion point during the backwash phase. The region of the beach, which is intermittently wet and dry due to waves run-up/down is called swash zone. During both onshore and offshore-directed flow stages, the flow strongly interacts with the sediment, mobilising it and leading to rapid bed changes within this region.

2.2 Cross-shore sediment transport and beach profile evolution

The swash and surf zones behave as interacting and co-evolving subsystems, exchanging sediment in the cross-shore direction, and affecting morphodynamic processes, such as breaker bars development and their offshore/onshore migration on sandy beaches (Masselink and Puleo, 2006; Brocchini and Baldock, 2008; Alsina et al., 2012).

Beach profiles can be classified in relation to the dominant wave climate by using the Dean's number (Gourlay and Van Der Meulen, 1969), defined as: $\Omega = H_{rep}/(w_s T_{rep})$, where H_{rep} and T_{rep} are the representative wave height and wave period, respectively, and w_s is the sediment settling velocity. A dissipative state of the beach is determined by $\Omega \geq 6$; while for $\Omega \leq 1$ a cross-shore beach profile is defined as reflective. Finally, for $1 < \Omega < 6$ beaches are classified as intermediate and usually present moderate mean slopes.

The beach profile evolution is mathematically described using a morphological model based on the balance between the temporal evolution of bed level and the spatial gradient of sediment transport. Therefore, a sediment transport formulation, which takes into account the mechanisms affecting sediment dynamics is necessary for a correct prediction of the beach morphodynamics.

Sediment transport in the nearshore region can occur as bed load and suspended load. In the former transport mode the sand particles move in direct proximity to the bed due to the instantaneous action of the bed shear stress (Bagnold, 1956); whereas the latter transport mode consists of sediment suspended by the fluid turbulence and advected at the flow velocity. Suspended sediment load is generally expressed in terms of sediment volume concentration (Van Rijn, 2007). The suspended load regime entails a phase lag between particles entrainment/settling and changes in the flow (Pritchard and Hogg, 2005). Moreover, in condition of strong bed shear stress (i.e., in the surf and swash zones), bed load transport can occur as a mobilisation of a thin near-bed layer with high concentration of sand particles referred to as sheet flow (see e.g., Puleo et al., 2014; Van Der Zanden et al., 2015; Mieras et al., 2017).

2.2.1 Surf zone dynamics

The surf zone can be divided into two sub-regions. The first is the outer surf zone, which extends immediately shoreward of the breaking point over a region of 5-10 times the breaking depth, and here waves change rapidly. The second is the inner surf zone, which extends between the outer region and the swash zone and is the region where broken waves propagate as bores (Svendsen, 2006). Breaking waves can be of different types (i.e., spilling, plunging and surging), depending on the wave and bed profile characteristics (Battjes, 1975). Once waves break, part of their energy is converted into turbulent kinetic energy in the surface roller near the surface, which is transported by the mean flow depending on the type of breaker (e.g., Ting and Kirby, 1994), and then gradually dissipated into heat. Turbulence production is associated with eddies, which contribute to the exchange of momentum (eddy viscosity) and of mass (eddy diffusivity). The net mass transport over a wave period next to the surface due to breaking is compensated by a depth-varying mean return current in the offshore direction (undertow). The result is a velocity profile, which is offshore directed near the bed, allowing the seaward transport of the sediment. The suspended sediment concentration can be described using a prescribed profile along the water column depending on the assumptions about the variation of the eddy diffusivity on the height above the bed (e.g., Van Rijn, 1984; Pritchard and Hogg, 2003).

The turbulence is produced under breaking waves both at the surface due to break-

ing and at the near-bed boundary layer due to bed shear stress. The wave breaking-induced turbulence can significantly increase the near-bed turbulence, by invading the wave boundary layer, and affecting near-bed sediment transport processes (e.g., Van der Zanden et al., 2016). The intra-wave suspended load transport in the surf zone is characterised by concentrations spanning over the whole water column with values ranging between 0.001 m^3/m^3 and 0.08 m^3/m^3 (i.e., between 2.65 kg/m^3 and 212 kg/m^3 for a sediment density equal to 2650 kg/m^3) from the highest point reached by the sediment in the water column to the top of the sheet layer, respectively. Its contribution can be of the same order of magnitude of that given by the intra-wave sheet flow transport. The latter is characterised by high sediment concentrations with values spanning from 0.08 m^3/m^3 to 0.64 m^3/m^3 (i.e., from 212 kg/m^3 to 1696 kg/m^3 for a sediment density equal to 2650 kg/m^3) at the top and bottom of the sheet layer, respectively, and a small mobile bed layer thickness compared to the total water depth (e.g., Mieras et al., 2017). Therefore, a correct description of the suspended and near-bed sediment concentrations in the surf zone requires the inclusion of a wave breaking-induced turbulence model. Furthermore, intra-wave near-bed sediment concentrations are phase coherent with the near-bed turbulent kinetic energy. Consequently, parametrisations of near-bed turbulence effects on the sediment entrainment could improve the prediction of the sediment concentration profile in the breaking region (Van Der Zanden et al., 2017b).

2.2.2 Swash zone dynamics

The swash zone is characterised by the periodic exposure to uprush and backwash of waves approaching the shoreface (Masselink and Puleo, 2006). Low-frequency non-breaking waves (i.e., infragravity waves associated with the propagation of wave groups) can also dominate swash motions depending on the beach morphology (Longuet-Higgins and Stewart, 1962; Symonds et al., 1982). Due to rapid flow changes during each wave cycle, the swash zone is the most dynamic region of the nearshore region, where large sediment transport rates and rapid morphological changes occur. Several processes influence the mutual interaction between the flow and sediment in this region. The uprush sediment transport is promoted by infiltration and exfiltration effects, flow acceleration, wave breaking-induced and bed-related turbulence, settling lag and sediment advection. Their relative effect depends on the type of swash zone (see Chardón-Maldonado

et al., 2016 for a comprehensive review). Infiltration and exfiltration effects are found more important for coarser sediment (Turner and Masselink, 1998), which is not object of this study. Flow acceleration generates strong pressure gradients that act on sand particles, contributing to their motion (Hoefel and Elgar, 2003). For instance, flow acceleration effects were taken into account in the expression of the bed shear stress formula by Nielsen (2002). The roles of bore turbulence and advection are crucial on sloped beaches dominated by incident swashes (e.g., Masselink and Puleo, 2006). A correct modelling of turbulence generation and advection is relevant to consider the contribution of pre-suspended sediment to the net sediment transport in the swash zone (e.g., Alsina et al., 2009). Reniers et al. (2013) also took into account the bore turbulence by using a simplified breaking-induced turbulence model to investigate swash zone processes.

The modelling of the Bottom Boundary Layer (BBL) is also an important aspect in the modelling of sediment transport in the region. The logarithmic profile model (see e.g., Barnes and Baldock, 2010; Briganti et al., 2011 among others) is deemed to provide accurate values of the bed shear stress in the swash zone. However, this model does not take into account important features of the velocity vertical profile during the swash. In fact, the near bed flow reverses before the upper part of the water column along the swash lens; this effect, simulated numerically by Zhang and Liu (2008) using a model based on the Raynolds Averaged Navier-Stokes Equations (RANSE), is not captured when the logarithmic profile is used.

Fig. 2.2 shows a schematisation of the sediment dynamics for a single swash event (i.e., individual, isolated wave). As the bore collapses on the beach during the uprush, the sediment is entrained in the water column and moved shoreward. At this stage the suspended sediment concentration rapidly increases in the water depth. Settling lag effects can promote onshore transport and together with the advected pre-suspended concentration play a key role in the deposition on the beachface (Pritchard and Hogg, 2005). Due to the high level of turbulence, sheet flow is also relevant, with sediment concentrations ranging between 0.08 and 0.5 m^3/m^3 from the top to the bottom of the sheet layer, respectively (e.g., Alsina et al., 2012). Close to the maximum run-up point, where the flow velocity decreases, gravity allows sediment deposition. Herein, contributions of suspended load and sheet flow become similar (see Fig. 2.2). During

the backwash, whose duration is generally longer than that of the uprush, turbulence is locally generated due to the bottom presence, linked to the bottom boundary layer evolution. Therefore, the bed load and sheet flow regimes exceed the sediment suspension over the whole rundown phase. In the last stage of the backwash, due to the decreasing flow acceleration, which is no longer capable of stirring sand particles, the suspension of the sediment does no longer occur (see e.g., Puleo et al., 2000; Masselink and Puleo, 2006; Chardón-Maldonado et al., 2016). Moreover, the offshore-directed sediment transport, which leads to the erosion of the beachface, is facilitated by the action of gravity by bed-slope effects. These effects increase with the beach steepness and generally lead to an equilibrium beach slope by balancing excess onshore transport (Walstra et al., 2007).

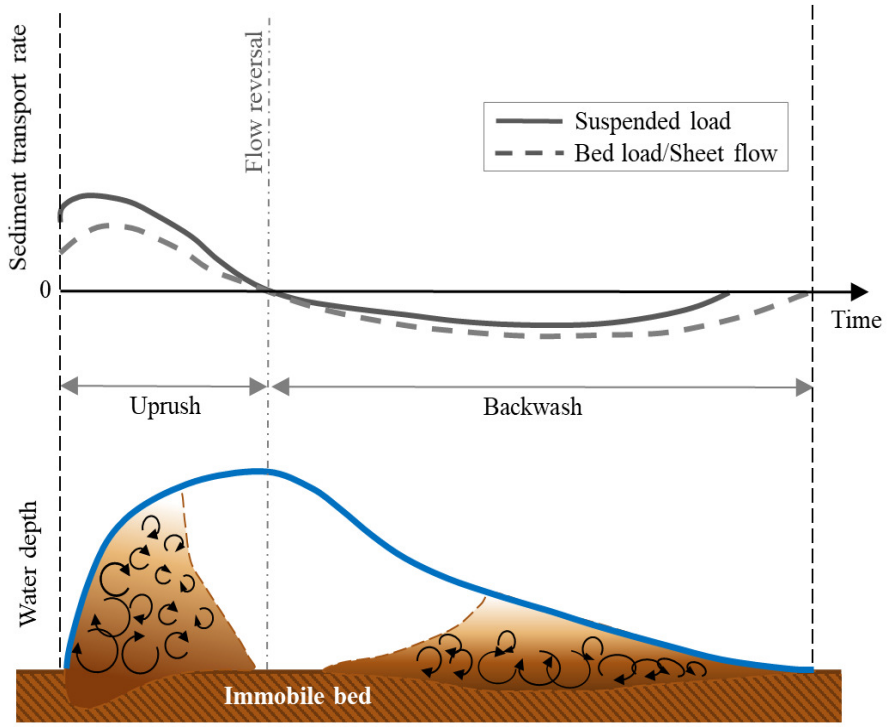

Figure 2.2: Schematisation of sediment dynamics for a single swash event at a cross-shore location in the swash zone (see Fig. 2.1); the figure is modified from Fig. 3 of Chardón-Maldonado et al. (2016).

Sediment dynamics are further complicated when swash-swash interactions are present. These interactions occur either when a wave interacts with the previous uprush event ("wave-capture"), or when the wave interacts with the previous backwash event ("wave-backwash" interaction). Wave-backwash interactions can be weak or strong. In the former type the incident wave overrides a preceding backwash, whereas the latter type is characterised by a stronger backwash than the upcoming uprush, hence resulting in a

hydraulic jump and an offshore-directed flow. Wave-capture mechanisms can reduce the onshore sediment advection; on the other hand, seaward sediment transport is inhibited by weak wave–backwash interactions (Alsina et al., 2018).

2.2.3 Breaker bars dynamics

Breaker bars generated in the surf zone of dissipative and intermediate beaches play a crucial role in the exchange of sediment between the beach and the shoreface (Masselink and Gehrels, 2014). Generation of a breaker bar in the inner surf zone occurs as the development of a trough shoreward and a bar crest accretion further seaward. The resulting erosion/deposition pattern is generated by large cross-shore gradients in the sediment transport rate (Aagaard et al., 2008). According to Roelvink and Stive (1989), breaker bars formation occurs at the converging point (i.e., in the breaking zone) of the offshore-directed undertow and wave non-linearities effects on sediment motions. They showed that in addition to the undertow-induced flow, which is the main driver of nearshore bars development, offshore-directed sediment transport and beach erosion, several mechanisms contribute to bars formation, such as wave breaking-induced turbulence, wave-induced asymmetric oscillatory flow, and wave grouping-induced long waves flow, i.e., infragravity waves (see Fig. 2.1). The last two mechanisms usually promote the shoreward motion of the sediment (e.g., Baldock et al., 2010; Dubarbier et al., 2015), and are not object of this study. Changes in swash dynamics also lead to variations in the surf zone morphodynamics, and consequently, affect the process of breaker bars development: a more reflective swash zone is dominated by more intense backwashes with large offshore-directed suspended sediment transport; instead a more dissipative swash zone leads to a larger number of swash-swash interactions, reducing the backwash intensities and the offshore suspended sediment transport (Alsina et al., 2012).

Breaker bars are very dynamic morphological features and observations showed that they typically move slowly shoreward when wave energy is low and move more rapidly offshore during storms (see e.g., Gallagher et al., 1998; Hsu et al., 2006). This study focuses on the latter condition. Under erosive wave conditions there is a linear relationship between the bar height and the bar location, whereas under accretive wave conditions bars can either migrate shoreward without decaying, or decrease in height during their onshore migration, depending on the influence of wave conditions on the

bar evolution (see e.g., Baldock et al., 2017; Eichentopf et al., 2018). Moreover, the initial beach profile occurring at the start of a considered sea state has an important influence on the rate of shoreline changes and sediment transport needed to reach an equilibrium condition (Eichentopf et al., 2020).

2.3 Hydro-morphodynamics numerical models

The modelling of the complex mechanisms previously described is crucial for an accurate prediction of the mutual feedback between the swash zone and the surf zone, and therefore, of position and shapes of breaker bars on sandy beaches. Two main modelling tools are available for the prediction of the nearshore morphological evolution. Empirical models are based on empirical equilibrium assumptions and relationships that use a parametric description of the physical processes. Process-based models are based on detailed representations of physical processes in the coastal region provided by the theoretical knowledge. Both types are usually calibrated using field measurements and laboratory experiments. Process-based models require a description of the wave field, while empirical ones require only a few parameters (e.g., significant wave height, spectral periods and main direction). The wave field can be described either using a wave-averaged or a wave-resolving approach. Wave-averaged models describe the hydrodynamics by using averaged quantities over the short-wave period. Therefore, processes such as wave breaking, skewness and asymmetry need to be parametrised using wave phase-averaged properties. These models are the most widely applied solvers for engineering purposes due to their robustness and computer-efficiency (e.g., XBeach, Roelvink et al., 2009, Delft3D, Lesser et al., 2004). However, they do not allow to fully solve the complexity of swash dynamics, which requires a wave-by-wave approach. On the contrary, wave-resolving hydro-morphodynamics models can resolve the flow and bed changes on the time scale of individual waves. As such they can capture intra-wave physical processes, including swash-swash interactions, which influence the offshore directed sediment transport that feeds the development of a beach profile.

2.3.1 Wave-resolving numerical models

Currently, a few existing numerical models are able to resolve the complex morphodynamics in the swash zone, therefore, limiting their use in coastal engineering practice.

Wave-resolving models are of two types: depth-averaged and depth-resolving models. The latter type can simulate the vertical structure of the flow and bed changes in the surf and swash zones, e.g., by using 3D (three-dimensional) the RANSE as governing hydrodynamics equations together with a turbulence closure and a morphological module. However, due to the large computational time required, their present validation is limited to less complex wave and morphodynamic conditions, such as sediment transport induced by isolated waves (e.g., Li et al., 2019), or to a limited coastal area mainly simulating laboratory experiments (e.g., Jacobsen et al., 2014; Jacobsen and Fredsoe, 2014; Kim et al., 2019; Larsen et al., 2020). The present study uses a depth-averaged wave-resolving framework, because this approach is the most practically used for engineering purposes, hence the most developed. The lack of a full 3D description of the velocity profile makes this type of models less computationally demanding. Depth-averaged wave-resolving models use as governing hydrodynamics equations one of the following alternatives: the Non Linear Shallow Water Equations (NLSWE), the non-hydrostatic NLSWE, or the Boussinesq-Type Equations (BTE).

NLSWE with hydrostatic pressure distribution cannot capture the waves dispersivity (i.e., waves with different frequencies travel at different speeds). To overcome this limitation, Boussinesq-types models (see Brocchini, 2013 for a comprehensive review) and solvers based on the NLSWE including a non-hydrostatic pressure term (see e.g., Stelling and Zijlema, 2003; Rijnsdorp et al., 2017) are used. BTE include both non-linearity and frequency dispersion. The latter is simulated by taking into account the effect of vertical accelerations on the pressure distribution. The vertical structure of the flow is modelled by assuming a second order polynomial shape. On the other hand, the non-hydrostatic NLSWE directly resolve the vertical structure of the flow in the governing equations, by using a discretization of the vertical domain into layers. This approach is thought to improve linear and non-linear wave properties and resolves more complex flow structures over the water column (Bai et al., 2018).

The number of layers in a multilayers model depends on the level of accuracy of the frequency dispersion description that one aims to achieve. The accuracy of one-layer non-hydrostatic models is comparable to that of weakly non-linear Boussinesq-type models in terms of waves dispersion. If the dispersivity parameter, $k_w d$, where k_w is the wave number (defined as: $k_w = 2\pi/L$, with L being the local wave length) and d is the still

water depth, is lower than 2.6, then the celerity error in the description of the frequency dispersion is of the order of 3%, which is acceptable for many engineering applications. Also, for non-hydrostatic NLSWE the effect of wave breaking can be captured without the use of a breaking model; whereas in Boussinesq-type models an empirical breaking mechanism and a dissipation model (e.g., application of surface roller concepts and artificial viscosity) are often used (see e.g., Kennedy et al., 2000).

To enable the computation of morphodynamics, these models require sub-models that compute suspended and bed load sediment transport based on intra-wave hydrodynamics, from which in turn, bed level changes can be computed. A state of the art of the available wave-resolving hydro-morphodynamics models is shown in Table 2.1.

Coupled Boussinesq-type wave and morphodynamics models are able to predict the bed evolution in the surf zone (see e.g., Xiao et al., 2010; Kim et al., 2017). However, the evolution of the berm in the upper swash zone is not accurately predicted (Kim et al., 2017). Additionally, Boussinesq-type wave models were coupled with phase-averaged morphology and wave-driven flow modules (Wenneker et al., 2011) in order to reduce the computational cost. Nevertheless, their application was limited to the prediction of the morphological evolution in the surf zone.

Wave-resolving hydro-morphodynamics models based on NLSWE are accurate in predicting swash zone dynamics (see e.g., Postacchini et al., 2012; Zhu and Dodd, 2015; Incelli et al., 2016), where they are primarily used because they cannot represent frequency dispersion. The non-hydrostatic NLSWE are used in the open-source Non-hydrostatic XBeach model (Smit et al., 2010). This model can simulate the depth-averaged wave-by-wave flow and surface elevation variations due to short waves similarly to the one-layer SWASH model (Zijlema et al., 2011). Also, it can model the intra-wave bed changes generated by isolated waves (e.g., tsunamis) or packets of waves and sea states at time scales of storms. Its morphological response has been extensively tested for gravel beaches (McCall et al., 2015), but not for sandy beaches. In fact, the available sediment transport formulations in Non-hydrostatic XBeach (Deltares, 2018) were originally developed for the wave-averaged version of the model, where the short wave energy is solved in a wave action balance. The reader is referred to Appendix A for a more detailed description of those sediment transport formulations and the limits related to their use in a wave-resolving framework.

Table 2.1: Main wave-resolving hydro-morphodynamics models; combined load refers to the combined modelling of bed load and suspended load transports.

Model	Open-source	Hydro-morphodynamics modelling	
		Hydrodynamics	Sediment transport modes
Xiao et al. (2010)		NLSWE + BTE	Combined load
Wenneker et al. (2011)		BTE + Wave-averaged flow module	Suspended load
Non-hydrostatic XBeach	✓	Non-hydrostatic NLSWE	Combined load
Jacobsen et al. (2014), Jacobsen and Fredsoe (2014)	✓	RANSE	Combined load
Zhu and Dodd (2015)		NLSWE	Combined load
Incelli (2016)		NLSWE	Combined load
Kim et al. (2017)		BTE	Combined load
Li et al. (2019)	✓	RANSE	Combined load
Kim et al. (2019)	✓	RANSE	Combined load
Larsen et al. (2020)	✓	RANSE	Combined load

Ruffini et al. (2020) showed that the application of the available wave-averaged sediment transport model (i.e., Van Thiel de Vries, 2009; Van Rijn et al., 2007 formulas) within Non-hydrostatic XBeach led to inaccurate simulated beach morphodynamics under bichromatic waves groups, which was related to inaccuracies in the modelled sediment concentrations. As shown in Figs. 10 and 12 of Ruffini et al. (2020), the model presents some limits in the representation of the intra-swash suspended sediment concentration. Unlike the observations, the modelled suspended sediment concentration drops to nearly zero values close to flow reversal. Consequently, the morphological evolution of the beach in the swash zone and the breaker bar development are not properly simulated (see also Figs. 7 and 8 of Ruffini et al., 2020).

2.4 Advancement in the state of the art of wave-resolving modelling

The novelty of this work is represented by the combined use of the non-hydrostatic NLSWE with wave-resolving sediment transport formulations. The open-source Non-hydrostatic XBeach model (Smit et al., 2010) is chosen for this study in order to improve the numerical modelling of the intra-wave sediment transport on sandy beaches. The development of the resulting hydro-morphodynamics model is intended to obtain an open-source storm-impact tool, for the use among the worldwide community of coastal engineers to solve the swash zone dynamics, and in turn, to accurately simulate the exchange of sediment between the swash and surf zones, which is of crucial importance for predicting the beach and shoreline evolution under extreme events. The governing equations of the model developed in this study are described in Chapter 3.

3 Numerical methodology

3.1 Introduction

In this chapter the wave-resolving hydro-morphodynamics model proposed in this study is described. The open-source Non-Hydrostatic XBeach (XBNH) model (Smit et al., 2010) is used and further developed to improve the prediction of the cross-shore intra-wave sediment transport in the swash and surf zones, and in turn, of the morphodynamic evolution of sandy beaches profiles. In particular, two new subroutines for the Intra-Wave Sediment Transport modelling (XBNH-IWST) are developed and implemented in the model. The first of them solves the wave-resolving Pritchard and Hogg (2003) transport equation for the suspended sediment concentration, including both advection and diffusion terms. The bed load transport is computed using the Meyer-Peter and Müller (1948) expression. The second subroutine solves a simple wave breaking-induced turbulence model together with a near-bed turbulence model. The effects of the wave breaking-generated turbulence can be included in the hydrodynamics and sediment transport governing equations through the bed shear stress modelling. Two additional models for the horizontal viscosity when breaking occurs are also included in XBNH-IWST.

Although XBNH can simulate hydrodynamics processes in both the cross-shore and long-shore directions, in this thesis only the former is considered. Therefore, the governing equations are applied and described only along the cross-shore direction, in their depth-averaged one-dimensional horizontal (1DH) form. Fig. 3.1 shows a schematisation of a typical cross-shore profile with the main variables used.

3.2 Hydrodynamics equations

The description of the hydrodynamics in XBNH is similar to the one-layer version of the SWASH model (Zijlema et al., 2011). The depth-averaged flow is computed using the non-hydrostatic 1DH NLSWE:

$$\frac{\partial \eta}{\partial t} + \frac{\partial hu}{\partial x} = 0, \tag{1}$$

$$\frac{\partial u}{\partial t} + u\frac{\partial u}{\partial x} - \frac{\partial}{\partial x}\left(\nu_h \frac{\partial u}{\partial x}\right) = -\frac{\partial(\tilde{p}_{nh} + g\eta)}{\partial x} - \frac{\tau_b}{\rho h}, \tag{2}$$

where x and t are the cross-shore horizontal coordinate (see Fig. 3.1) and time, respectively, η is the water surface elevation, $h = \eta + d$ is the total water depth (being d the still water depth), u is the depth-averaged cross-shore flow velocity, $g = 9.81$ m/s^2 is the gravitational acceleration, ρ is the density of water, $\tilde{p}_{nh}$ is the depth-averaged dynamic pressure normalised by the density. p_{nh} represents the non-hydrostatic contribution to the total pressure, $p_{tot} = g(\eta - z) + p_{nh} = p_h + p_{nh}$, where p_h is the hydrostatic pressure normalised by the density and z is the vertical coordinate (see Fig. 3.1). All depth-averaged quantities are intended to be averaged along the total water depth. τ_b is the total bed shear stress (discussed in Section 3.5.4). ν_h is the horizontal viscosity. In the available version of XBNH (see also Deltares, 2018) ν_h is computed by using the Smagorinsky (1963) model to account for the horizontal mixing at spatial scales smaller than the computational x-grid size, Δx, in the mean flow. The Smagorinsky (1963) model computes the viscosity, i.e., $\nu_{h,s}$, as follows:

$$\nu_h = \nu_{h,s} = (C_s \Delta x)^2 \sqrt{2\left(\frac{\partial u}{\partial x}\right)^2}, \tag{3}$$

where $C_s = 0.1$ is the Smagorinsky's constant. The development of an additional horizontal viscosity model, when wave breaking occurs, is presented in Section 3.5.3.

Similarly to the one-layer version of the SWASH model (Zijlema et al., 2011; Smit et al., 2010), $\tilde{p}_{nh}$ is computed from the mean of the dynamic pressure between the surface and the bed, using the free surface boundary condition: $p_{nh}|_\eta = 0$, and assuming a linear behaviour over the water depth. The dynamic pressure at the bed is computed using the vertical momentum balance, where advective and diffusive terms are considered negligible compared to the vertical acceleration determined by the gradient of the non-hydrostatic pressure, as follows:

$$\frac{\partial w}{\partial t} + \frac{\partial p_{nh}}{\partial z} = 0, \tag{4}$$

where w is the vertical velocity. The vertical velocity at the bed is computed by using the kinematic bottom boundary condition as follows:

$$w|_b = -u\frac{\partial d}{\partial x}. \tag{5}$$

Here the Keller-box method is applied to describe the pressure gradient in the vertical direction following Stelling and Zijlema (2003), hence:

$$p_{nh}|_b = -\frac{h}{2}\left(\left.\frac{\partial p_{nh}}{\partial z}\right|_\eta + \left.\frac{\partial p_{nh}}{\partial z}\right|_b \right), \tag{6}$$

Consequently, the vertical momentum balance at the surface is obtained by substituting Eq. (6) in Eq. (4) as:

$$\frac{\partial\, w|_\eta}{\partial t} = 2\frac{p_{nh}|_b}{h} - \frac{\partial\, w|_b}{\partial t}. \tag{7}$$

Finally, the conservation of local mass closes the system of equations as follows:

$$\frac{\partial u}{\partial x} + \frac{w|_\eta - w|_b}{h} = 0. \tag{8}$$

Eq. (8) together with the boundary conditions allows to solve Eqs. (1) and (2).

In the cases analysed in this study $k_w d$ (defined in Section 2.3.1) is usually lower than 0.5. Therefore, the celerity error in the description of frequency dispersion by the pressure correction is of the order of 1% (Bai et al., 2018). The highest value of $k_w d$ for the cases here considered is 0.8. Therefore, according to the cited study, the corresponding celerity error is of the order of 3%.

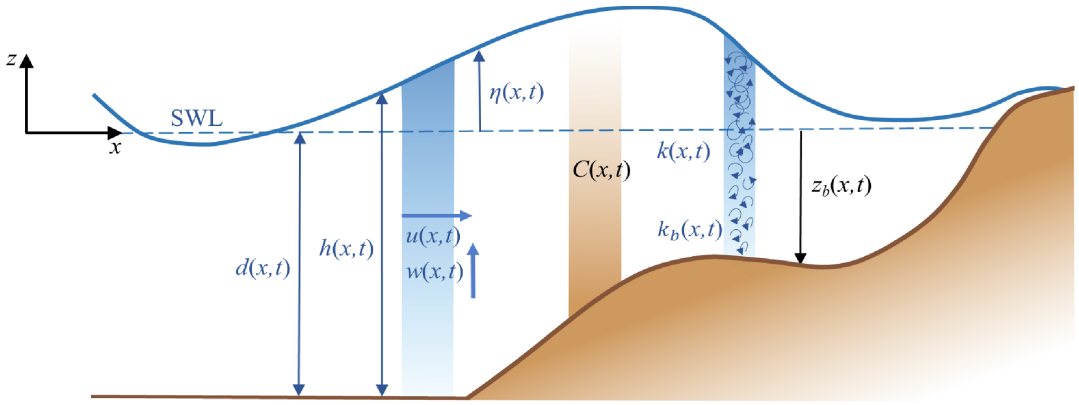

Figure 3.1: Schematisation of a cross-shore beach profile and main model variables considered

Wave breaking modelling in XBNH is improved by using the Hydrostatic Front Approximation (HFA), similarly to Smit et al. (2013), in which the non-hydrostatic pressure term is disabled when waves fronts exceed a certain steepness. As long as this condition is met they are modelled as hydrostatic bores, because the energy dissipation is in-

trinsically solved by the NLSWE through a bore-like propagation. Therefore, the HFA is applied where $\frac{\partial \eta}{\partial t} > \alpha_{br} c$, with c as the wave celerity in shallow water ($c = \sqrt{gh}$) and α_{br} the local threshold; waves are considered to reform where $\frac{\partial \eta}{\partial t} < \beta_{br} c$, with $\beta_{br} < \alpha_{br}$. According to the literature, $0.4 \leq \alpha_{br} \leq 0.8$ in XBNH; $\beta_{br} = 0.25\alpha_{br}$ (see also Smit et al., 2013 and Deltares, 2018). Roelvink et al. (2018) recommended $\alpha_{br} = 0.4$ for XBNH. This approach does not introduce either a separate roller model nor an artificial viscosity model to explicitly account for the wave breaking-induced turbulent kinetic energy.

3.3 Intra-wave sediment transport model development

In this section, the development of XBNH-IWST is described. The available formulations for suspended and bed load transport in XBNH (Deltares, 2018) were originally developed for the Wave-Averaged Sediment Transport (XBNH-WAST) modelling. Therefore, XBNH-IWST uses the newly implemented wave-resolving transport equation of Pritchard and Hogg (2003) for the suspended sediment concentration. The bed load transport rate in this study is computed using the Meyer-Peter and Müller (1948) formulation.

3.3.1 Bed load transport equation

The bed load transport rate, q_b, is calculated using the formulation derived by Meyer-Peter and Müller (1948), which is already available in XBNH (see McCall, 2015). Its implementation is summarised here following with the main equation:

$$q_b = 8(\theta - \theta_{cr})^{1.5} \sqrt{\Delta g D_{50}^3} \frac{\tau_b}{|\tau_b|} S_{sl}, \tag{9}$$

where θ is the Shields parameter, θ_{cr} is the critical Shields parameter, $\Delta = (\rho_s - \rho)/\rho$, in which ρ_s is the sediment density and D_{50} is the median sediment grain diameter. θ is computed as $\theta = \tau_b/(\Delta \rho g D_{50})$ and θ_{cr} is given by Soulsby (1997). S_{sl} represents the bed slope effects computed following Deltares (2018):

$$S_{sl} = 1 - \alpha_{sl} \frac{\partial z_b}{\partial x}, \tag{10}$$

where $\alpha_{sl} = 0.15$ according to Deltares (2018) and z_b is the bed level (see also Fig. 3.1).

The Meyer-Peter and Müller (1948) formula is considered appropriate for the swash zone (see Chardón-Maldonado et al., 2016 among others) and multiple versions of the formula have been tested, for example in Postacchini et al. (2012) for sand, while in O'Donoghue et al. (2016) and Briganti et al. (2018) for coarse sand. When compared to the original Meyer-Peter and Müller (1948) formula the Postacchini et al. (2012) formulation showed very similar results in terms of net bed changes (see e.g., Briganti et al., 2016). Therefore, other formulas were not tested in this study.

3.3.2 Intra-wave equation for suspended sediment concentration

The XBNH-IWST model developed here uses the newly implemented Pritchard and Hogg (2003) transport equation for the intra-wave suspended sediment concentration, with the addition of a diffusion term:

$$\frac{\partial hC}{\partial t} + \frac{\partial\left[\left(huC + D_C h\frac{\partial C}{\partial x}\right)S_{sl}\right]}{\partial x} = m_e\left(\frac{\tau_b - \tau_{b,cr}}{\tau_{ref}}\right)^R - w_s C_{nb} = E - D, \qquad (11)$$

where C is the depth-averaged suspended sediment concentration, D_C is the sediment diffusion coefficient, which is set equal to the horizontal viscosity (i.e., $D_C = \nu_h$). Therefore, the suspended sediment transport rate, q_s, is defined as: $q_s = \left(huC + D_C h\frac{\partial C}{\partial x}\right)S_{sl}$. In this study the maximal value of C, C_{max}, is considered as the higher physically possible sediment concentration for a fluidised bed and defined as: $C_{max} = 1 - n_{p,d}$, with $n_{p,d}$ the porosity for a fluidised bed. m_e is the mobility parameter, which determines the erodibility of the sediment as suspended load, $\tau_{b,cr}$ is the critical bed shear stress, τ_{ref} is the reference bed shear stress, $R > 0$ is a dimensionless numerical exponent (Pritchard and Hogg, 2003), w_s is the sediment settling velocity computed using the Ahrens (2000) formulations (see also Deltares, 2018) and C_{nb} is the near-bed suspended sediment concentration at a small near-bed reference height, d_{nb}, above z_b. The two terms on the right side in Eq. (11) represent the erosion rate, E, and the deposition rate, D, respectively. C_{nb} in D is computed as:

$$C_{nb} = CK_C, \qquad (12)$$

where the shape factor, K_C, represents the relative importance of sediment settling and mixing; for good mixing $K_C = 1$. According to Pritchard and Hogg (2003), K_C is assumed to depend only on sediment properties and the depth-averaged hydrodynamics. Consequently:

$$K_C = \frac{(1-B)}{d'_{nb}\left(d'^{B-1}_{nb} - 1\right)}, \tag{13}$$

where B is the Rouse number defined as:

$$B = \frac{w_s}{\kappa u_*}, \tag{14}$$

where $\kappa = 0.4$ is the von Karman constant and u_* is the friction velocity: $u_* = (\tau_b/\rho)^{1/2}$. For $B \ll 1$, K_C tends to 1 and the sediment can be considered as well-mixed in the water column, whereas for $B \geq 1$, the vertical structure of the sediment suspension must be taken into account (i.e., C_{nb} increases).

d'_{nb} is the dimensionless near-bed reference height, given by a simplified form of Van Rijn formula as shown in Soulsby (1997) with the relationship:

$$d'_{nb} = \frac{d_{nb}}{h} = 0.519\left(\frac{D_{50}}{\lambda}\right)^{0.3}, \tag{15}$$

with λ being a reference length-scale, which in this study is defined equal to the offshore wave height (see Chapter 5).

The model described above allows to express the vertical distribution of the suspended sediment (i.e., $C_z(d_z)$) by a power-law profile as in Soulsby (1997):

$$C_z(d_z) = C_{nb}\left(\frac{d_z}{d_{nb}}\right)^{-B} \quad \text{in which} \quad d_{nb} \leq d_z \leq h, \tag{16}$$

where d_z is the vertical elevation from z_b. The concentration profile described by Eq. (16) corresponds to a linearly increasing eddy diffusivity of the sediment with the height above the bed. Note that C_z is not a model output, but it is herein computed in the aftermath of the numerical simulations.

3.4 Bed-updating modelling

The bed-updating is modelled using an Exner-type equation that takes into account the storage of sediment in the water column as follows:

$$(1 - n_p)\frac{\partial z_b}{\partial t} + \frac{\partial q_b}{\partial x} = E - D, \tag{17}$$

where n_p is the bed porosity and q_b is computed as in Eq. (9).

3.5 Wave breaking-generated turbulence model development

In this section the development of the intra-wave wave breaking-generated turbulence model within XBNH-IWST is described. The newly implemented model for the additional horizontal viscosity for the HFA and the bed shear stress modelling, accounting for the effects of turbulence, are also described.

3.5.1 Intra-wave balance equation for the kinetic turbulent energy

The wave-resolving wave breaking-induced turbulence model developed here is based on the depth-averaged Turbulent Kinetic Energy (TKE) balance, where k is the depth-averaged TKE:

$$\frac{\partial hk}{\partial t} + \frac{\partial huk}{\partial x} = Source_k - Sink_k. \tag{18}$$

$Source_k$ and $Sink_k$ model the production and dissipation of TKE, respectively. Two alternative models are selected to compute $Source_k$ and $Sink_k$. The first turbulence model follows Reniers et al. (2013), and it is here referred to as the R13 model. This turbulence model is based on the roller surface model for the wave energy dissipation. The second turbulence model considered is similar to that used by Alsina et al. (2009), based on the time-depended wave energy model proposed by Kobayashi and Wurjanto (1992), and it is here referred as the KW92-A09 model.

R13 turbulence model

$Source_k$ is related to the dissipation of the organised wave energy and it is formulated as:

$$Source_k = g\delta_R \frac{\partial \eta_{cr}}{\partial t}, \tag{19}$$

where δ_R is the roller-thickness and η_{cr} is the critical surface elevation, which defines the threshold for the wave breaking, according to the time-depended criterion as follows:

$$\frac{\partial \eta_{cr}}{\partial t} = m_{cr}\sqrt{gh}, \tag{20}$$

where m_{cr} is the slope of the surface roller on the underneath flow. Reniers et al. (2013) used $m_{cr} = 0.07$. The surface roller is assumed to propagate at a velocity equal to the wave celerity in shallow water and δ_R is determined by:

$$\frac{\partial \delta_R}{\partial t} = \left[max\left(\frac{\partial \eta}{\partial t}, 0\right) - \frac{\partial \eta_{cr}}{\partial t}\right]. \tag{21}$$

$Sink_k$ is related to the dissipation of k and is determined as follows:

$$Sink_k = k^{1.5}. \tag{22}$$

KW92-A09 turbulence model

The KW92-A09 turbulence model considers the wave energy dissipation rates, D_b and D_f, due to breaking and bed friction, respectively, which are computed with a time-dependent wave energy model given (Kobayashi and Wurjanto, 1992) by:

$$\frac{\partial E_w}{\partial t} + \frac{\partial F_w}{\partial x} = -(D_b + D_f) = -D_w, \tag{23}$$

where D_w is the total dissipation rate, E_w is the wave energy density and F_w is the flux of energy. E_w is determined as:

$$E_w = \frac{1}{2}\left(hu^2 + g\eta^2\right), \qquad d > h, \tag{24}$$

and

$$E_w = \frac{1}{2}\left[hu^2 + g\left(\eta^2 - d^2\right)\right], \qquad d \leq h. \tag{25}$$

F_w is computed following Dingemans (1994) (page 194) as:

$$F_w = hu\left(g\eta + \frac{1}{2}u^2 + \tilde{p}_{nh}\right). \tag{26}$$

D_f is defined as:

$$D_f = c_f|u|u^2, \tag{27}$$

where c_f is the dimensionless friction coefficient. Consequently, D_b is implicitly determined as the difference between D_w and D_f. $Source_k$ is therefore, computed as:

$$Source_k = D_b. \tag{28}$$

$Sink_k$ is computed similarly to Alsina et al. (2009) as:

$$Sink_k = \frac{\gamma_d h k^{1.5}}{l_m}, \tag{29}$$

where γ_d is a decay coefficient, which was estimated to be approximately 0.08 for plane jets (see e.g., Launder and Spalding, 1972; Deigaard et al., 1992) and l_m is the turbulent mixing length assumed of order of h, hence, determined as:

$$l_m = max\big(\delta_R, \gamma_l h\big), \tag{30}$$

where δ_R is given by Eq. (21) and $\gamma_l = 0.3$ following Svendsen et al. (1987).

Note that a third model based on the roller energy balance similar to that used in Svendsen (1984) was also considered. However, results obtained showed that a model of this type is not suitable for a wave-resolving modelling approach. The reader is referred to Appendix B for a more detailed description of the aforementioned model implementation and results.

3.5.2 Near-bed turbulence modelling

The wave breaking-induced near-bed TKE, k_b, is computed similarly to Roelvink and Stive (1989), assuming an exponential decay of k from the surface:

$$k_b = k\left[min\left(\frac{1}{exp(\frac{h}{l_m}) - 1}, 1\right)\right]. \tag{31}$$

Therefore, the total near-bed turbulence, $k_{b_{tot}}$, including both the effects of wave breaking-generated turbulence and bed friction, is given as:

$$k_{b_{tot}} = k_b + u_*^2. \tag{32}$$

3.5.3 Additional horizontal viscosity modelling

Following Smit et al. (2013), an additional viscosity model is used if the HFA is activated (i.e., wave breaking occurs) in order to prevent the generation of high frequency noise in the wave profile due to the model adaptation to the enforced hydrostatic pressure distribution. Two alternative additional horizontal viscosity models are newly implemented. The first model is based on the theories of Kolmogorov (1942) and Prandtl (1945) and it is here referred to as the K42-P45 viscosity model; ν_h is determined as follows:

$$\nu_h = max\left(\nu_{h,s}, l_m\sqrt{k}\right). \tag{33}$$

The second viscosity model considered is based on the mixing length method used in Smit et al. (2013), where the aforementioned noise is related to local gradients in u, and therefore, it will be referred to as the S13 viscosity model:

$$\nu_h = max\left(\nu_{h,s}, (\mu h)^2\left|\frac{\partial u}{\partial x}\right|\right), \tag{34}$$

where μ is a numerical parameter. Smit et al. (2013) showed that within the range $0.75 \leq \mu \leq 3$ results are not significantly different in terms of spatial distribution of the computed wave height. If none of the two viscosity models described above are considered, the expression of ν_h returns to $\nu_h = \nu_{h,s}$.

3.5.4 Bed shear stress modelling

If wave breaking-induced turbulence is not taken into account, then τ_b is computed using the quadratic stress law as:

$$\tau_b = c_f \rho u|u|. \tag{35}$$

k_b is included in the computation of τ_b (i.e., $\tau_{b,k}$) as:

$$\tau_b = \tau_{b,k} = c_f \rho u|u| + c_f \rho \gamma_k k_b, \tag{36}$$

where γ_k is a calibration factor. When the effects of turbulence are not taken into account, the expression of τ_b returns to $\tau_b = c_f \rho u|u|$.

Relatively simple unsteady BBL models, such as the momentum integral method (Sumer et al., 1987) used also in NLSWE solvers (e.g., Briganti et al., 2011), could be also considered. However, the results in terms of τ_b are comparable with simpler formulations, such as the one considered in this study (see e.g., Briganti et al., 2018). Further evidence that supports the applicability of the quadratic stress law to compute the total bed shear stress for swash flows was recently provided by Howe et al. (2019). Phase differences could be significant and more complex BBL models should be used, especially prior to wave breaking (e.g., Rijnsdorp et al., 2017). Nevertheless, the detailed modelling of the BBL is outside the scope of the present study.

3.6 Inclusion of turbulence effects in the sediment transport model

In this section the inclusion of the wave breaking-induced turbulence effects in the intra-wave sediment transport modelling is described for both bed load and suspended load transports.

Inclusion of turbulence effects in the bed load transport model

k_b is included in the computation of q_b (see Eq. (9)) through τ_b (i.e., $\tau_{b,k}$), and in turn, θ (i.e., θ_k) as:

$$\theta = \theta_k = \frac{\tau_{b,k}}{\Delta \rho g D_{50}}. \tag{37}$$

If $k_b = 0$ then the expression of θ reduces to $\theta = \tau_b/(\Delta \rho g D_{50})$.

Inclusion of turbulence effects in the suspended load transport model

For the suspended sediment transport modelling, $\tau_{b,k}$ affects the computation of u_* in B by means of Eq. (14). Consequently, the computation of K_C, and in turn, of C_{nb}, are also affected by means of Eqs. (13) and (12), respectively. E including the effects of k_b

(i.e., E_k) is determined as:

$$E = E_k = m_e \left(\frac{\tau_{b,k} - \tau_{b,cr}}{\tau_{ref}} \right)^R. \tag{38}$$

Additionally, D_C is affected by the contribution of wave breaking-induced turbulence through the horizontal viscosity modelling (see also Section 3.3.2, page 21).

3.7 Coordinate system and computational grid

XBNH-IWST uses a computational coordinate system where the x-axis is cross-shore oriented and points to the coast. The numerical spatial discretisation in the model uses a staggered grid where depth, water level, and sediment concentration are defined in the cells center, and velocity and sediment flux at the cells interface. One layer is used in the vertical direction, therefore, the hydrodynamics and sediment concentration are computed as depth-averaged.

For the water flow, the numerical integration is performed by applying a flux limited version of the McCormack (1969) predictor-corrector scheme, which is second order accurate where the solution is smooth and reduces to first order accuracy in proximity of discontinuities (e.g., hydraulic jumps). Hence, a limiter parameter is incorporated in the solution procedure for adding artificial dissipation in the regions of steep gradients. The method is mass and momentum conservative. For the time integration XBNH-IWST uses a dynamically adjusted time step, Δt. The user defines a value for the maximum Courant Number, CN, and the program in turn, adjusts the time step in order to guarantee that $u\Delta t/\Delta x < \text{CN}$. This method allows to take largest possible Δt, resulting in a more efficient time integration.

3.8 Numerical implementation

The numerical implementation described in this study was carried out using the open-source XBeachX release (Deltares, 2018). The numerical model structure and procedure are described in the following sections.

3.8.1 Numerical model structure

Fig. 3.2 shows a flow chart, which describes the structure of the main XBNH program including XBNH-IWST. The initial values of the variables are computed at $t = t_i$ (t_i being the initial time). XBNH is forced using the time series of water surface elevation and velocity at the upstream boundary. If the wave breaking-generated turbulence is computed through the subroutine developed in this study, the flow is updated considering the effects of turbulence (i.e., through the bed shear stress and the additional horizontal viscosity modelling). XBNH can compute the sediment transport either by using XBNH-WAST, or XBNH-IWST. The latter computes the intra-wave sediment transport by considering the combined use of the Pritchard and Hogg (2003) and the Meyer-Peter and Müller (1948) expressions (referred to as PH03+MPM in Fig. 3.2) for solving the suspended and the bed load transport rates, respectively.

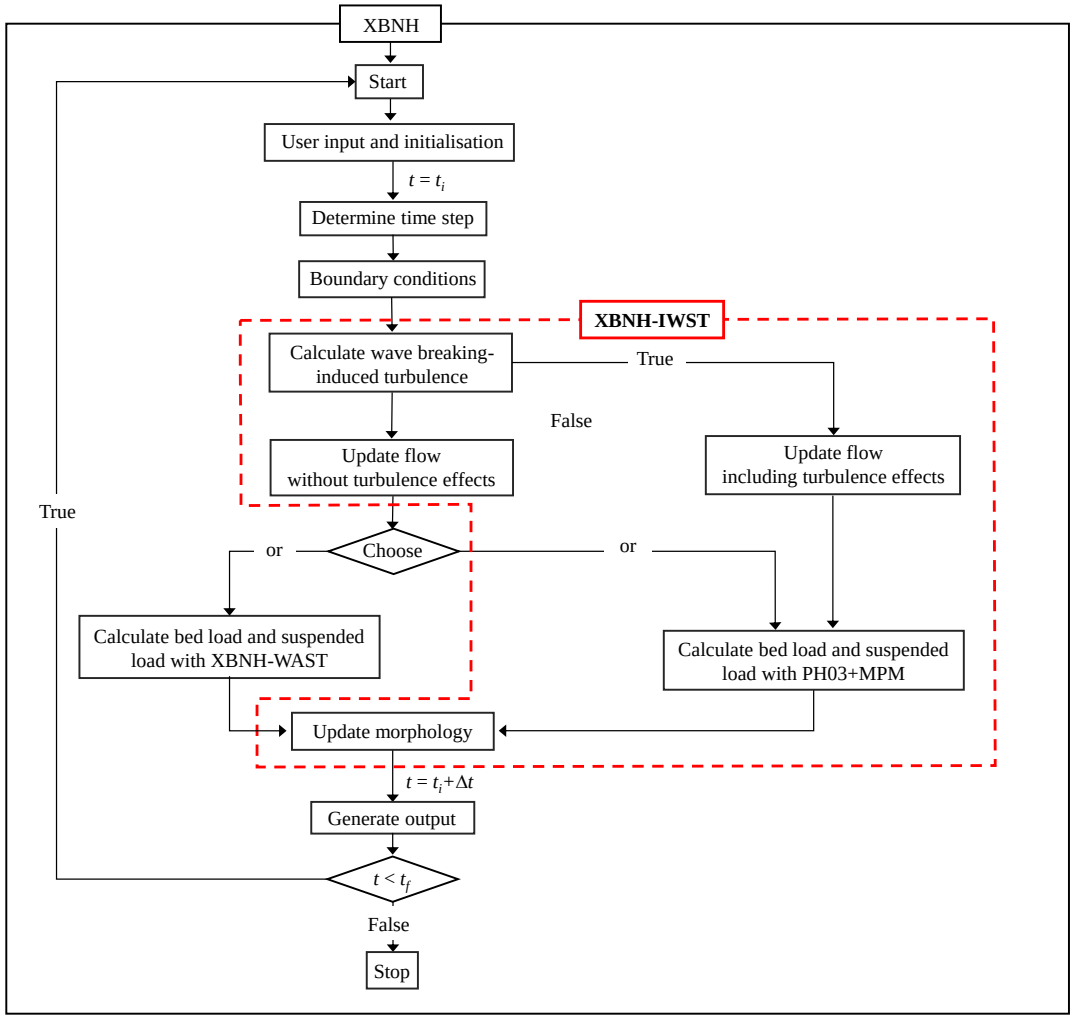

Figure 3.2: Flow chart showing the structure of the main program of XBNH including the newly implemented XBNH-IWST computations for the intra-wave sediment transport modelling

The morphology is finally updated and the variables are updated to the new time step (i.e., at $t = t_i + \Delta t$). The simulation ends if $t < t_f$ (with t_f being the stop time of the numerical simulation).

3.8.2 Numerical procedure

Fig. 3.3 shows how the new subroutines (i.e., XBNH-IWST) developed in this study were incorporated in the main XBNH numerical procedure. Note that only the modules and the subroutines which were modified/newly implemented in this study are herein shown.

The hydrodynamics and the horizontal viscosity are computed by the "flow_timestep" module. The latter uses the "nonh" module, which computes the non hydrostatic pressure correction, the "bedroughness" module, which computes the bed shear stress, and the "morphevolution" module, which solves the sediment transport with the "transus" subroutine and updates the bed elevation through the "bed_update" subroutine. The newly developed "waveturb_nonh_gm" and "pritchard_hogg_mpm_gm" subroutines for the wave breaking-generated turbulence and the intra-wave sediment transport, respectively, were included in the "morphevolution" module. The effects of the wave breaking-induced turbulence can be included in the computation of the bed shear stress through the "turbulence_boundary_layer_effect" subroutine, included in the "bedroughness" module. For a complete description of the XBNH numerical procedure the reader is referred to Deltares (2018).

For the numerical implementation of the Pritchard and Hogg (2003) equation the available Galappatti (1983) scheme (see Deltares, 2018) was used and adapted to the newly implemented formulation, so that the suspended sediment equilibrium concentration, $C_{eq,s}$, is expressed as:

$$C_{eq,s} = \frac{m_e}{w_s}\left(\frac{\tau_b - \tau_{b,cr}}{\tau_{ref}}\right)^R \frac{1}{K_C}. \tag{39}$$

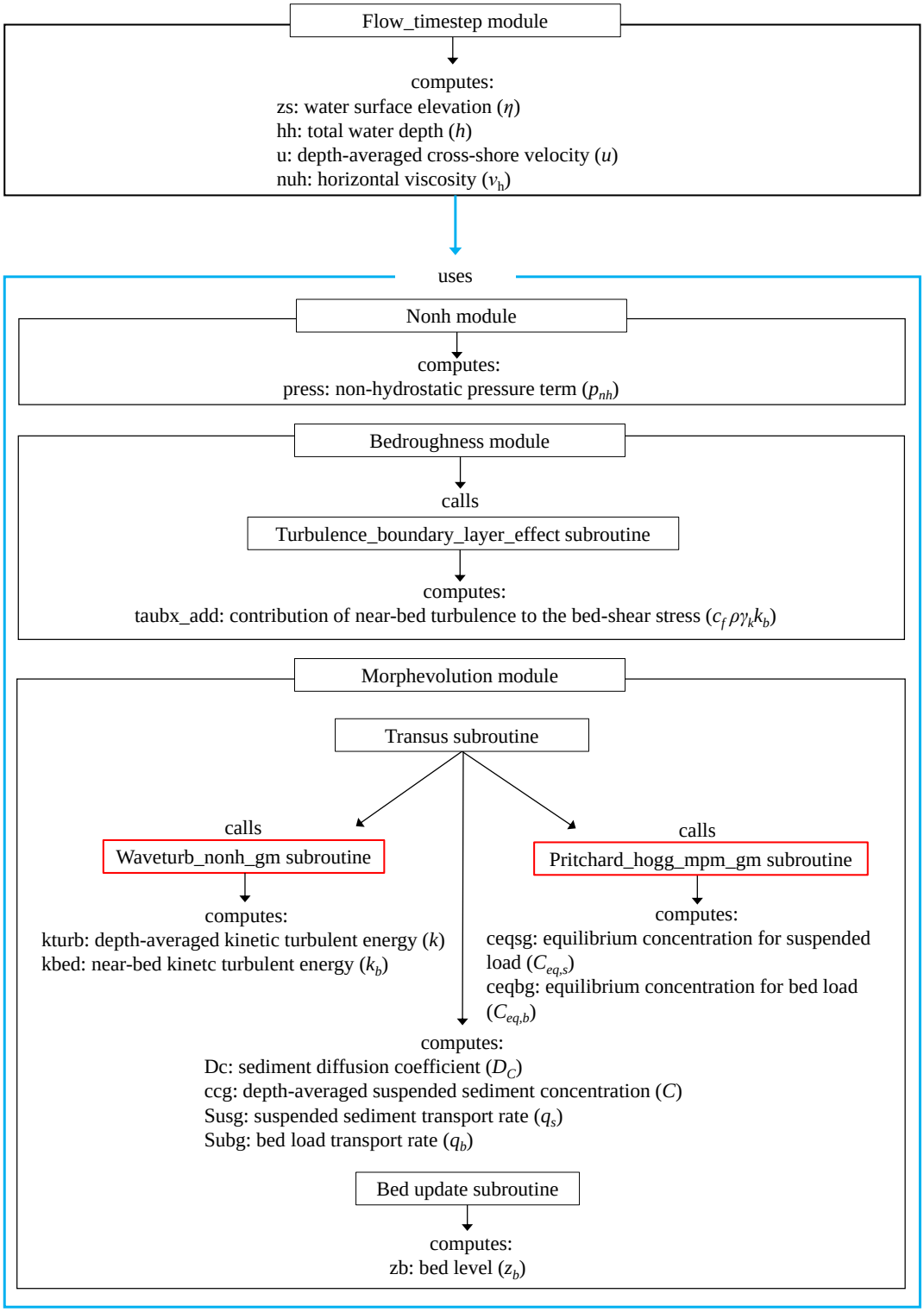

Figure 3.3: Inclusion of the newly developed subroutines (i.e., XBNH-IWST) in the XBNH numerical procedure for the hydro-morphodynamics computations; the newly implemented subroutines are highlighted with a red rectangle.

4 XBNH-IWST model verification

4.1 Introduction

In this chapter, the XBNH-IWST model is first verified against the high-accuracy solution of Zhu and Dodd (2015) for an idealised bore generated by a solitary wave over an erodible sloped beach. For this test case, the combined use of the intra-wave sediment transport Pritchard and Hogg (2003) formulation and the Meyer-Peter and Müller (1948) relationship (see Section 3.3) is tested in XBNH-IWST. Wave breaking-induced turbulence effects are, therefore, not considered in this verification. The two wave breaking-generated turbulence models included in XBNH-IWST (see Section 3.5) are subsequently verified against the experiments of Ting and Kirby (1994) involving spilling and plunging breakers over a non-erodible sloped bed. For the latter case, the two additional horizontal viscosity models for the HFA implemented for this study (see Section 3.5.3) are also tested.

The model performance is quantified by computing the normalised Root-Mean-Squared Error (nRMSE), defined as:

$$\text{nRMSE} = \frac{\sqrt{\frac{1}{N}\Sigma_i^N (y_{m,i} - y_{ref,i})^2}}{s_{y_{ref}}}, \tag{40}$$

where $y_{m,i}$ is the i-th sample of the modelled quantity, y_m and $y_{ref,i}$ is the i-th sample of the corresponding reference sample, y_{ref} (e.g., semi-analytical, experimental); N is the number of samples; $s_{y_{ref}}$ is the standard deviation of the reference quantity and it is defined as:

$$s_{y_{ref}} = \sqrt{\frac{1}{N-1}\Sigma_i^N (y_{ref,i} - \bar{y}_{ref})^2}, \tag{41}$$

with $\bar{y}_{ref} = (1/N)\Sigma_i^N y_{ref,i}$ being the mean value of y_{ref}. nRMSE = 0 indicates perfect agreement between model predictions and reference quantities.

Following Bosboom et al. (2020), the Root-Mean-Square Transport Error (RMSTE), measured in m^2, is also computed to quantify the model performance in terms of final bed changes. The RMSTE measures the mismatch between the predicted final bed level, $z_{b_{f,m}}$, and the reference one, $z_{b_{f,ref}}$, in terms of the minimum (i.e., optimal) quadratic sediment transport cost required to transform the predictions into the reference field.

It is computed as:

$$\text{RMSTE} = \sqrt{\frac{1}{N}\Sigma_i^N Q_i^2}, \tag{42}$$

where Q_i is the $i-$th sample (with $i = 1$ corresponding to the onshore boundary of the x-domain, located landward of the maximum run up) across the x-domain of the sediment volume per unit width, Q, required to transform $z_{b_{f,m}}$ into $z_{b_{f,ref}}$. The conservation of mass is satisfied so that $\partial Q/\partial x = z_{b_{f,m}} - z_{b_{f,ref}}$, and $Q_{i=1} = 0$ is assumed.

To further assess the correlation between the time series of the modelled and reference quantities the Pearson's cross-correlation coefficient, $-1 \leq \rho_{mr} \leq 1$, is used, and it is defined as:

$$\rho_{mr} = \frac{cov(y_{ref}, y_m)}{s_{y_{ref}} s_{y_m}}, \tag{43}$$

where $cov(y_{ref}, y_m)$ is the covariance of the time series of the modelled and reference quantities, and it is computed as:

$$cov(y_m, y_{ref}) = \frac{1}{(N-1)}\Sigma_i^N \left[(y_{m,i} - \bar{y}_m)(y_{ref,i} - \bar{y}_{ref})\right], \tag{44}$$

where $\bar{y}_m = (1/N)\Sigma_i^N y_{m,i}$ is the mean value of y_m and s_{y_m} is the standard deviation of the time series of the predicted quantity.

4.2 XBNH-IWST sediment transport model verification

4.2.1 The Zhu and Dodd (2015) test case

Zhu and Dodd (2015) proposed a semi-analytical solution of the flow and bed evolution generated by a solitary wave over an erodible sloped beach. The aforementioned study used the same expressions for the sediment transport and bed-updating modelling as in XBNH-IWST.

Fig. 4.1 shows the model domain in Zhu and Dodd (2015). For $x < -10$ m, the bed is flat, while for $x \geq -10$ m an erodible 1:15 sloped beach is considered. The initial shoreline position is located at $x = 5$ m. The initial condition of η and u throughout the x-domain were given by Mei (1989) and the hydrodynamic Riemann condition, respectively. As shown in Fig. 4.1, at the initial condition the wave crest is located at $x = -22$ m. The wave height, H, is equal to 0.60 m. The governing equations in Zhu and Dodd (2015) were solved using the Method Of Characteristics (MOC), and the

hydrodynamics were solved using the hydrostatic NLSWE, which included bed shear stress. The suspended sediment transport was computed using the Pritchard and Hogg (2003) transport equation, assuming a well-mixed condition (i.e., $K_C = 1$). The bed load was given by the Meyer-Peter and Müller (1948) formula. Moreover, in Zhu and Dodd (2015) numerical grid cells in the swash constantly remained wet once they had become wet for the first time (see also Antuono et al., 2012; Zhu et al., 2012).

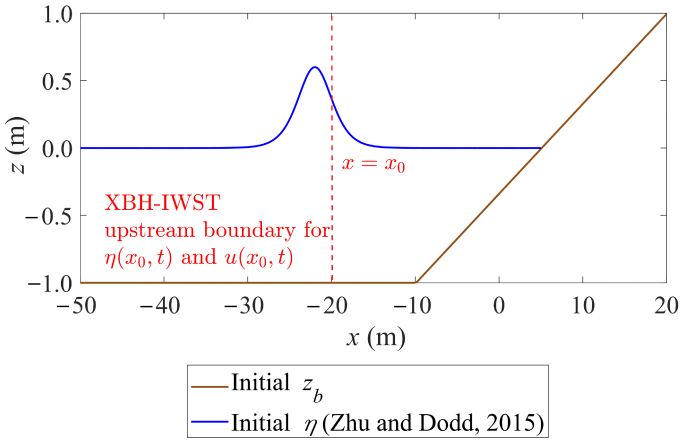

Figure 4.1: Model domain and initial condition in Zhu and Dodd (2015) and upstream boundary location in the XBH-IWST model domain (red-dashed line)

4.2.2 Model set-up

The model set-up and physical parameters followed closely those used in Zhu and Dodd (2015). Time series of η and u were provided by Zhu and Dodd (2015) at $x = x_0 = -20$ m, i.e., where the wave does not propagate as a bore, with a time resolution of 1×10^{-3} s. As shown in Fig. 4.1, the upstream boundary in the model domain is located at $x = x_0$; the computational domain extended to $x = 25$ m. $\Delta x = 0.05$ m was chosen. Unlike Zhu and Dodd (2015), in XNBH-IWST a minimum water depth, $h_{min} = 0.0001$ m, was defined (see Incelli et al., 2016), below which a grid point is considered dry. The simulated time was approximately 33 s. Table 4.1 shows a summary of the main parameters included and conditions assumed in the Pritchard and Hogg (2003) equation. Similarly to Zhu and Dodd (2015), the well-mixed condition was assumed (i.e., $K_C = 1$ was set). Consistently with the cited study, the diffusion term and bed slope effects in the computation of q_s and q_b were not taken into account. To compare the response of the model proposed in this study with Zhu and Dodd (2015) in terms of intra-wave sediment transport, the hydrostatic approach was considered by turning off the non-hydrostatic

pressure term. This model configuration is herein referred to as XBH-IWST.

Table 4.1: Main parameters and conditions in the Pritchard and Hogg (2003) transport equation

Parameters		Values
c_f	=	0.01
w_s	=	0.03 m/s
m_e	=	0.002 m/s
$\tau_{b,cr}$	=	0 N/m^2
λ	=	1 m
τ_{ref}	=	$\rho c_f u_{ref} \lvert u_{ref} \rvert$, where $u_{ref} = \sqrt{g\lambda}$
R	=	1
K_C	=	1 (set constant in XBH-IWST; assumption of well-mixing)

4.2.3 XBH-IWST modelling of the Zhu and Dodd (2015) solution

Part of the results shown in this section are included in Mancini et al. (2021). Comparison of XBH-IWST predictions and Zhu and Dodd (2015) for the hydrodynamics is illustrated in Fig. 4.2.

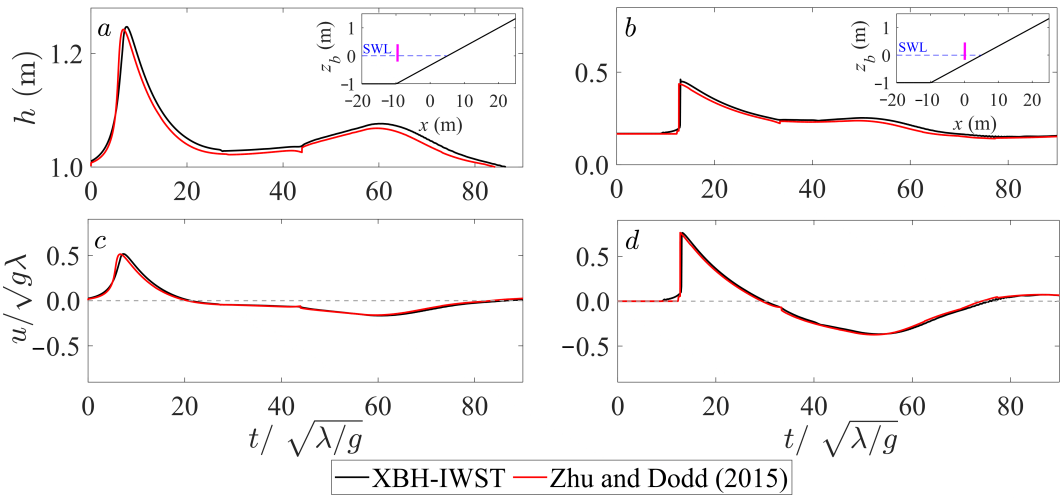

Figure 4.2: Time series of hydrodynamics; *a*: h at $x = -10$ m; *b*: h at $x = 0$ m; *c*: $u/\sqrt{g\lambda}$ at $x = -10$ m; *d*: $u/\sqrt{g\lambda}$ at $x = 0$ m; reference line: grey-dashed line; the two subplots in *a* and *b* show the two cross-shore locations in the model domain, respectively.

Results show a very good agreement in terms of hydrodynamics response between XBH-IWST and Zhu and Dodd (2015). This is quantitatively confirmed by the nRMSE and ρ_{mr} reported in Table 4.2.

Table 4.2: nRMSE and ρ_{mr} for h and $u/\sqrt{g\lambda}$ at two different cross-shore locations

	nRMSE		ρ_{mr}	
	h	$u/\sqrt{g\lambda}$	h	$u/\sqrt{g\lambda}$
$x = -10$ m	0.2078	0.1382	0.9881	0.9915
$x = 0$ m	0.2576	0.1684	0.9794	0.9860

Fig. 4.3*a* and *b* shows the final bed profiles, z_{b_f}, and the final bed changes, i.e., $\Delta z_{b_f} = z_b(t = t_f, x) - z_b(0, x)$, respectively; t_f is the time at the end of the simulation.

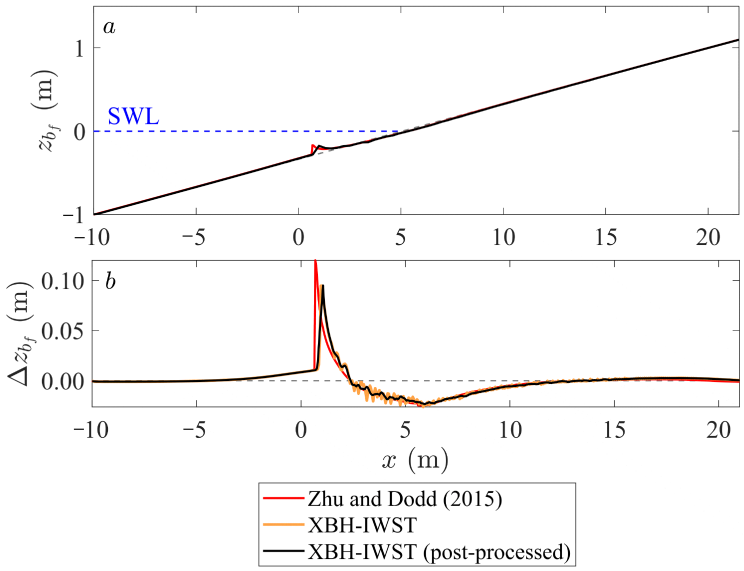

Figure 4.3: *a*: z_{b_f}; *b*: Δz_{b_f}; reference line: grey-dashed line

Despite the height of the bed step being underestimated by 20% with respect to Zhu and Dodd (2015), XBH-IWST captures the erosion and deposition well. nRMSE = 0.0085 for Δz_{b_f} and RMSTE = 0.003 m^2, showing good performances of XBH-IWST compared with Zhu and Dodd (2015). Similarly to Briganti et al. (2012), Δz_{b_f} were post-processed by using a moving average. Spurious oscillations are shown in the region $x > 2$ m, due to the backwash bore that runs down the beach and generates a sharp deposition at $x \simeq 2$ m. These results are consistent with the study of Kranenborg et al. (2019) where

a dam-break was simulated with XBNH. Additionally, a sensitivity analysis was carried out to find out the role of the maximum CN and Δx on these oscillations. In XBNH, the default value of CN is 0.7. For the sensitivity analysis CN was increased and decreased by 20%. Results shown in Fig. 4.4*a* indicate that CN does not affect the numerical oscillations. As shown in Fig. 4.4*a*, the oscillations can be reduced by increasing Δx by an order of magnitude (e.g., $\Delta x = 0.2$ m) with respect to $\Delta x = 0.05$ m. Nevertheless, as expected, it was found that the much lower resolution would lead to the underestimation of the height of the backwash step by 50%.

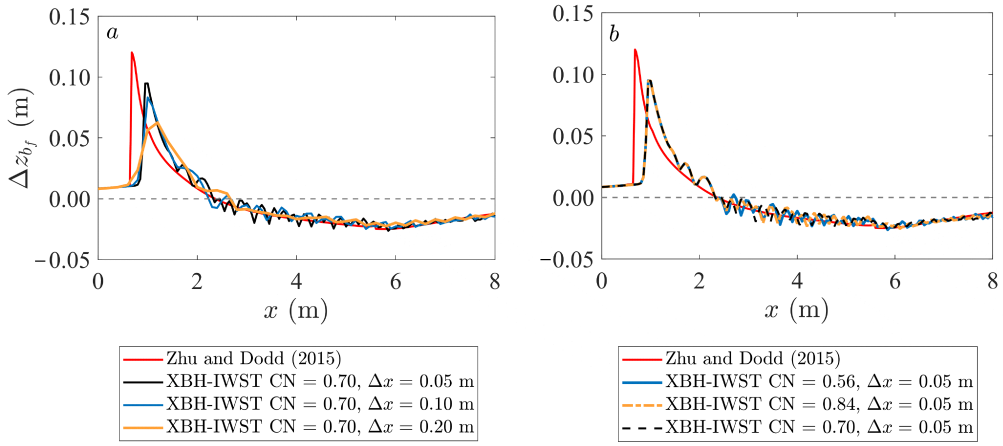

Figure 4.4: *a*: Δz_{b_f} for different values of Δx; *b*: Δz_{b_f} for different values of CN; reference line: grey-dashed line

Fig. 4.5 shows the time series of C at two different x-coordinates. The corresponding nRMSE are 0.2142 ($x = 0$ m) and 0.3200 ($x = 5$ m).

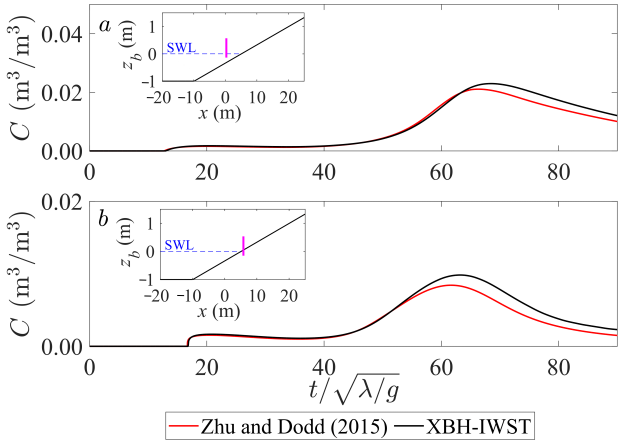

Figure 4.5: Time series of C at different x-coordinates; *a*: $x = 0$ m; *b*: $x = 5$ m; the two subplots in *a* and *b* show the two cross-shore locations in the model domain, respectively.

The high correlation between the predicted C and that computed by Zhu and Dodd (2015) is confirmed by $\rho_{mr} = 0.9922$ ($x = 0$ m) and $\rho_{mr} = 0.9877$ ($x = 5$ m). Small differences in terms of intra-wave Δz_b and C were found between the two models, possibly due to the different numerical approach used to solve the governing equations in XBH-IWST and Zhu and Dodd (2015), respectively. Fig. 4.6*a* shows the contour plots of the difference, $\Delta z_{b,diff}$, between Δz_b computed by XBH-IWST ($\Delta z_{b_{XBH-IWST}}$) and by Zhu and Dodd (2015) ($\Delta z_{b_{ZD15}}$); Fig. 4.6*b* shows the difference, ΔC, between C computed by XBH-IWST ($C_{XBH-IWST}$) and by Zhu and Dodd (2015) (C_{ZD15}). The former is computed as $\Delta z_{b,diff} = |\Delta z_{b_{XBH-IWST}}| - |\Delta z_{b_{ZD15}}|$; the latter is computed as $\Delta C = C_{XBH-IWST} - C_{ZD15}$. Results show that ΔC increases in the last stage of the uprush close to flow reversal, due to the different prediction of the maximum run-up between the two models. Also, $\Delta C > 0$ during the whole duration of the backwash. This means that XBH-IWST predicts a larger C than Zhu and Dodd (2015) at this stage of the flow. In terms of bed changes, the onshore deposition predicted by XBH-IWST during the uprush is slightly shifted in time and space (i.e., where $\Delta z_{b,diff} > 0$ for $30 < t/\sqrt{\lambda/g} < 50$ and $16 < x < 20$ m) with respect to Zhu and Dodd (2015). The larger magnitude of $\Delta z_{b,diff}$ is found for $1 < x < 2$ m where the backwash bed-step develops for both models. This reflects the lower height of the bed step predicted by XBH-IWST.

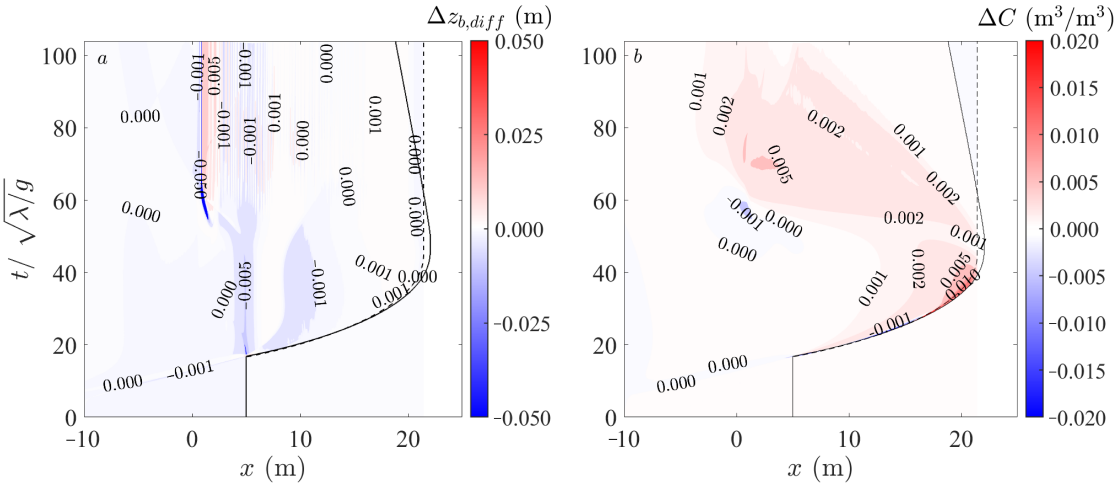

Figure 4.6: Contour plots of difference quantities; *a*: $\Delta z_{b,diff}$; *b*: ΔC; Zhu and Dodd (2015) shoreline: black-dashed line; XBH-IWST shoreline: black-solid line

4.3 XBNH-IWST wave breaking-generated turbulence model verification

4.3.1 The Ting and Kirby (1994) test case

In the laboratory experiments of Ting and Kirby (1994), cnoidal type-waves resulting in spilling and plunging breakers were simulated over a non-erodible 1:35 sloped bed. An offshore $d = 0.40$ m was used. The spilling breakers condition was characterised by a wave period, $T = 2$ s and an offshore $H = 0.125$ m; whereas, for the plunging breakers condition, $T = 5$ s and an offshore $H = 0.128$ m were used. Water surface elevations and flow velocities were measured using capacitance Wave Gauges (WG) and Laser-Doppler Anemometer (LDA) sensors, respectively. Velocity measurements were conducted mainly below the trough level and above the near-bed level. The turbulent velocities were obtained using the turbulent velocity fluctuations. The latter, in turn, were computed with the original time series of the flow velocity measured with the LDA sensors. Fig. 4.7 shows the experimental domain and the two x-coordinates considered for the model-data comparison for the spilling and plunging breakers, respectively.

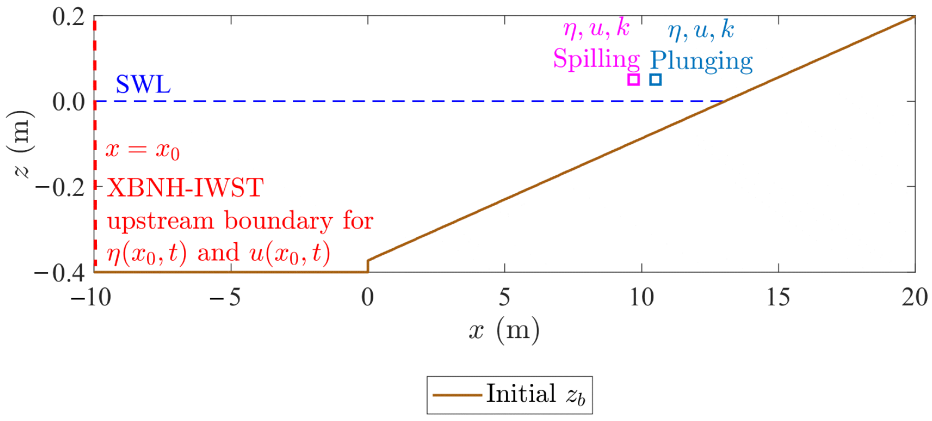

Figure 4.7: Ting and Kirby (1994) experimental domain with the two measurements cross-shore locations considered in this study for the spilling and plunging breakers indicated by the coloured squares, and the upstream boundary location in XBNH-IWST (red-dashed line)

Both x-coordinates are positioned shoreward of the breaking points, which were observed at $x = 6.400$ m and $x = 7.795$ m, for the spilling and plunging breakers, respectively. The reader is referred to Ting and Kirby (1994) for a more detailed description of the experimental procedure.

4.3.2 Model set-up

The model was set up following Ting and Kirby (1994). Both spilling and plunging breakers were simulated. Time series of η and u, with a resolution of $1{\times}10^{-3}$ s, were prescribed at the upstream boundary located 10 m from the toe of the sloped bed. η was determined using the 2^{nd}-order cnoidal wave theory as Svendsen (2006); u was computed using the shallow water theory. $\Delta x = 0.05$ m was used and $h_{min} = 0.001$ m was defined (see Incelli, 2016). $\alpha_{br} = 0.4$ was chosen for the HFA following Roelvink et al. (2018). $c_f = 0.002$ was chosen following Reniers et al. (2013).

Section 4.3.3 shows a comparison between the R13 and KW92-A09 wave breaking-induced turbulence models implemented herein, by considering the parameters included set to their reference values (i.e., $m_{cr} = 0.07$ and $\gamma_d = 0.08$). As shown in Section 4.3.3, the R13 and KW92-A09 turbulence models response is similar. Therefore, the sensitivity analysis and calibration were performed for the KW92-A09 turbulence model only, because it includes a higher number of parameters than the R13 turbulence model. Calibration of the KW92-A09 turbulence model was carried out following the sensitivity analysis shown in Section 4.3.4. A comparison between the performance of the the K42-P45 and S13 horizontal viscosity models for the HFA is illustrated in Section 4.3.5. Results shown in Sections 4.3.4 and 4.3.5 led to the choice of values for m_{cr} (= 0.1) and γ_d (= 0.4), while ν_h for the HFA was modelled using the S13 viscosity model with $\mu = 1$. $\gamma_k = 1$ was set according to Van Rooijen et al. (2012) and Reniers et al. (2013). Results for the performance of XBNH-IWST with the calibrated KW92-A09 turbulence model and the S13 viscosity model are shown in Section 4.3.6.

4.3.3 Comparison between the R13 and KW92-A09 turbulence models

In this section the performance of the R13 and KW92-A09 turbulence models (see also Section 3.5.1) included in XBNH-IWST is assessed for the spilling breakers. Fig. 4.8*a*, *b* and *c* shows the distribution of the maximum water surface elevation, η_{max}, the mean water level, η_{mean}, and the minimum water surface elevation, η_{min}, respectively, across the x-domain for both the R13 and KW92-A09 turbulence models. Note that $m_{cr} = 0.07$, $\gamma_d = 0.08$ and ν_h was computed using the K42-P45 viscosity model. Results show that differences in the effect of the two TKE models on η_{max}, η_{min} and $\bar{\eta}$ are almost indiscernible. This is also confirmed by the corresponding nRMSE presented in Table 4.3.

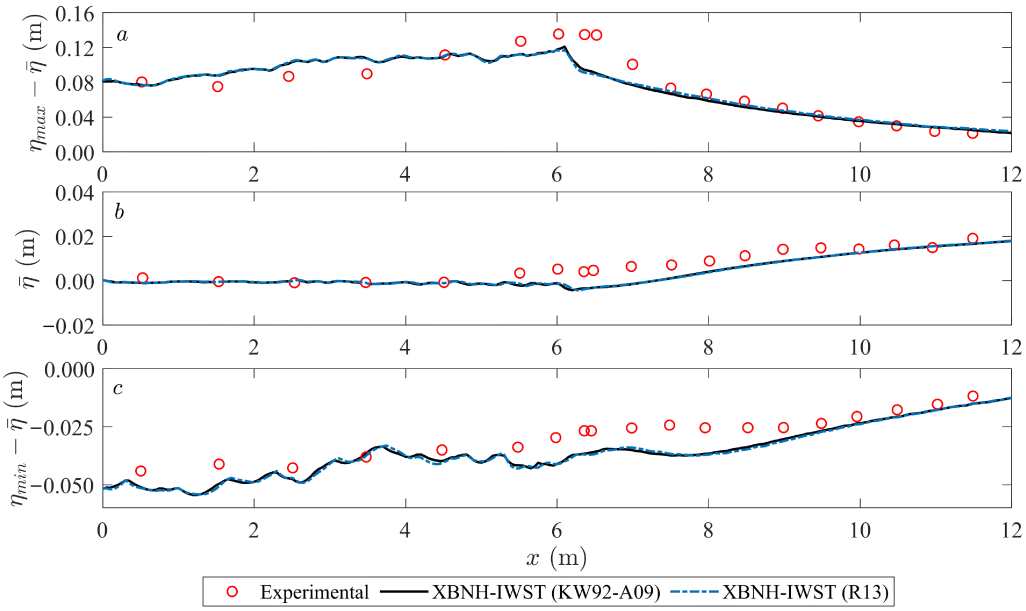

Figure 4.8: Distribution of surface elevation across the x-domain; a: η_{max}; b: η_{mean}; c: η_{min}

Table 4.3: nRMSE for η_{max}, η_{min} and $\bar{\eta}$

	nRMSE	
	KW92-A09	R13
η_{max}	0.3613	0.3654
η_{min}	1.1297	1.1612
$\bar{\eta}$	1.2216	1.2556

Fig. 4.9a, b, c and d shows the time-varying phase-averaged η, u, turbulent velocity, $k^{0.5}$, and near-bed turbulent velocity, $k_b^{0.5}$, respectively, at $x = 9.7$ m (i.e., in the inner surf zone). The corresponding nRMSE and ρ_{mr} are shown in Table 4.4. Results indicate that the hydrodynamics response of the model is very similar for both approaches from a qualitative and a quantitative point of view (see also Table 4.4). XBNH-IWST overestimates $k^{0.5}$ with both the R13 and KW92-A09 turbulence models.

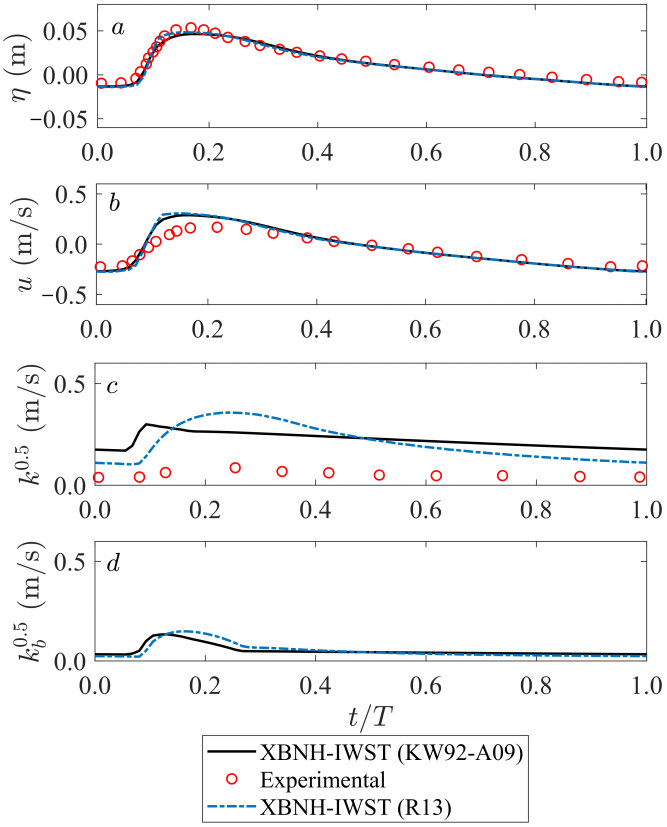

Figure 4.9: Time-varying phase-averaged quantities at $x = 9.7$ m; *a*: η; *b*: u; *c*: $k^{0.5}$; *d*: $k_b^{0.5}$; comparison between the KW92-A09 model and the R13 model

Table 4.4: nRMSE and ρ_{mr} for η, u and $k^{0.5}$

	nRMSE		ρ_{mr}	
	KW92-A09	R13	KW92-A09	R13
η	0.1284	0.1297	0.9962	0.9981
u	0.3276	0.3616	0.9845	0.9768
$k^{0.5}$	9.0634	9.1095	0.7554	0.9746

4.3.4 Sensitivity analysis of results to the parameters included in the KW92-A09 turbulence model

A sensitivity analysis of the results to the parameters included in the KW92-A09 turbulence model is herein shown for the spilling breakers. The parameters varied in the analysis were m_{cr} and γ_d. $m_{cr} = 0.07$ is considered as a reference value according to Reniers et al. (2013); m_{cr} is then increased and decreased within the range recommended by Deltares (2018) for the wave-averaged version of XBeach (i.e., $0.05 \leq m_{cr} \leq 0.3$).

As shown in Fig. 4.9, $k^{0.5}$ is found to be overestimated for $\gamma_d = 0.08$. By increasing γ_d, $Sink_k$ in Eq. (29) is expected to increase as well. Therefore, the sensitivity analysis for this parameter was carried out by increasing its value by two, five and ten times with respect to its reference value. Fig. 4.10 shows the results of the sensitivity analysis for the time-varying phase-averaged η (Fig. 4.10*a* and *e*), u (Fig. 4.10*b* and *f*), $k^{0.5}$ (Fig. 4.10*c* and *g*) and $k_b^{0.5}$ (Fig. 4.10*d* and *h*) at $x = 9.7$ m for m_{cr} and γ_d, respectively.

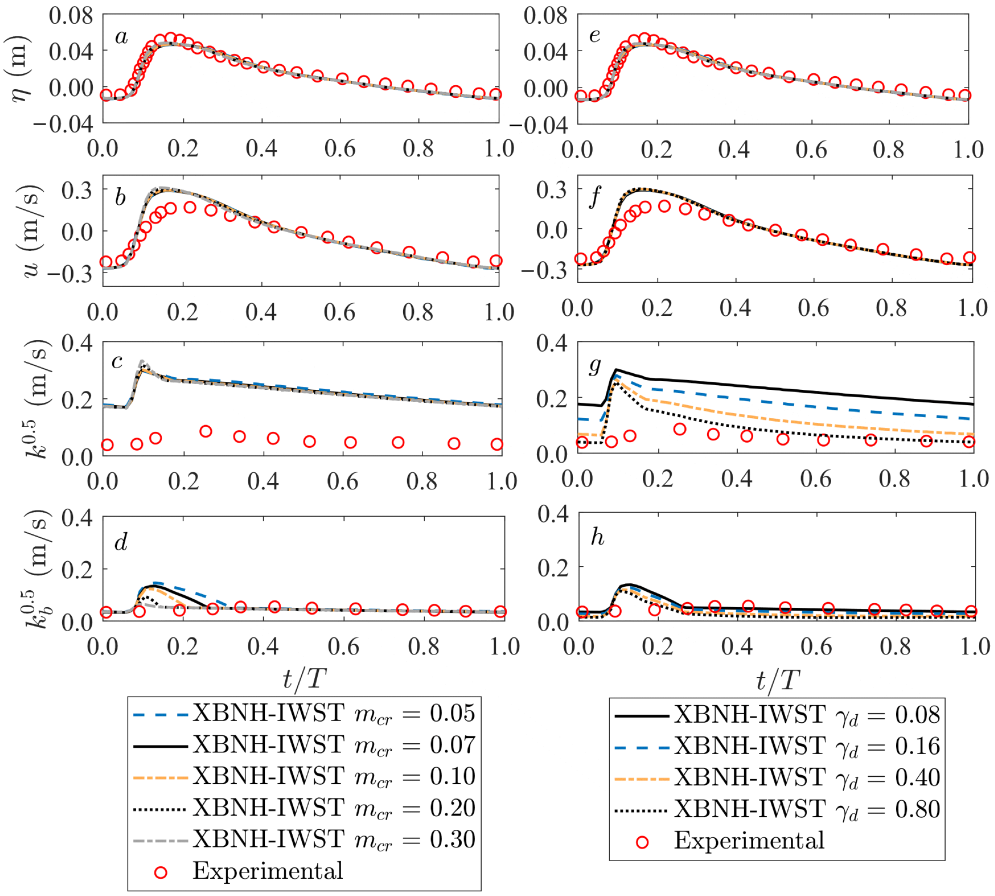

Figure 4.10: Time-varying phase-averaged quantities for different values of m_{cr} and γ_d, respectively, at $x = 9.7$ m; *a* and *e*: η; *b* and *f*: u; *c* and *g*: $k^{0.5}$; *d* and *h*: $k_b^{0.5}$

The two parameters m_{cr} and γ_d were varied one by one considering the other at its reference value. ν_h was computed using the K42-P45 viscosity model for the HFA. Results show that variations of m_{cr} and γ_d mostly affect the predictions of $k^{0.5}$ and $k_b^{0.5}$, while the direct effect on η and u is difficult to discern. Therefore, the nRMSE and ρ_{mr} are herein shown for $k^{0.5}$ and they are included in Tables 4.5 and 4.6. The nRMSE decreases if m_{cr} increases until $m_{cr} = 0.1$; the accuracy in terms of nRMSE is comparable for $m_{cr} \geq 0.1$. The nRMSE decreases if γ_d is increased. Instead, by

increasing m_{cr} or γ_d, respectively, the shape difference between the modelled and the observed $k^{0.5}$ becomes higher and ρ_{mr} decreases.

Table 4.5: nRMSE and ρ_{mr} for $k^{0.5}$ for different values of m_{cr}

	m_{cr}	0.05	0.07	0.1	0.2	0.3
$k^{0.5}$	nRMSE	9.3465	9.0634	8.9625	8.9151	8.9602
	ρ_{mr}	0.7681	0.7554	0.7356	0.6905	0.6631

Table 4.6: nRMSE and ρ_{mr} for $k^{0.5}$ for different values of γ_d

	γ_d	0.08	0.16	0.4	0.8
$k^{0.5}$	nRMSE	9.0634	6.7027	4.2648	2.9919
	ρ_{mr}	0.7554	0.7353	0.6785	0.5826

4.3.5 Comparison between the K42-P45 and S13 horizontal viscosity models

In this section a comparison between the K42-P45 and S13 viscosity models (see Section 3.5.3) for the HFA is illustrated. The KW92-A09 turbulence model within XBNH-IWST was used with $m_{cr} = 0.07$ and $\gamma_d = 0.08$. Fig. 4.11a, b and c shows η_{max}, η_{mean} and η_{min}, respectively, across the x-domain for the spilling breakers.

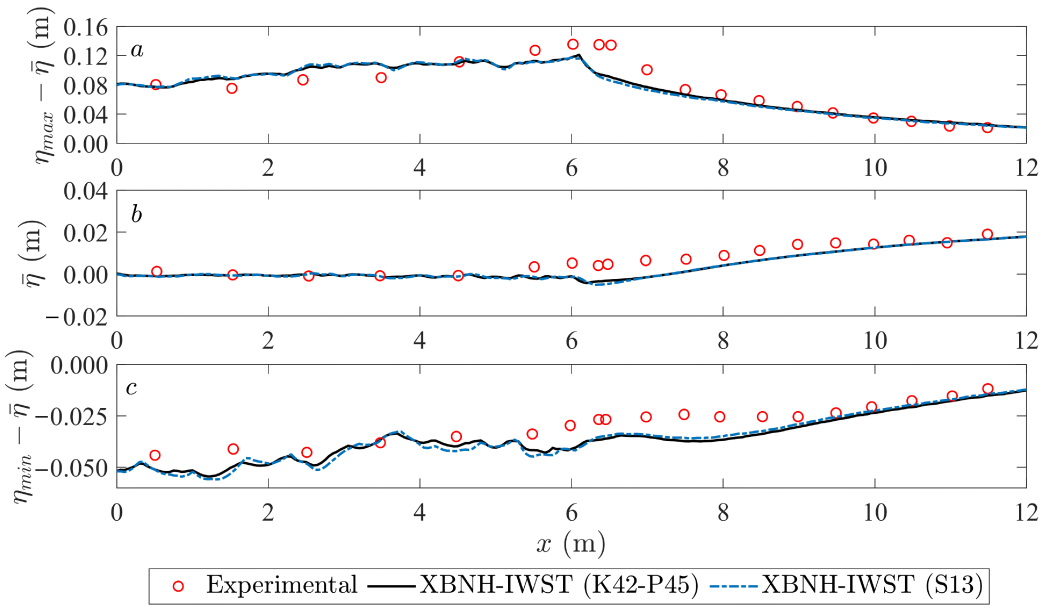

Figure 4.11: Distribution of surface elevation across the x-domain; a: η_{max}; b: η_{mean}; c: η_{min}

Results show that the turbulent dissipation is slightly higher when the S13 viscos-

ity model is applied. This is highlighted in Fig. 4.11*a* in the inner surf zone (i.e., for $x > 6.4$ m) and in Fig. 4.12*a*, *b*, *c* and *d* for the time-varying phase-averaged η, u, $k^{0.5}$ and $k_b^{0.5}$, respectively, at $x = 9.7$ m. The nRMSE and ρ_{mr} for η, u and $k^{0.5}$ are shown in Table 4.7. The S13 viscosity model within XBNH-IWST shows a higher accuracy in terms of nRMSE for u and $k^{0.5}$ compared to the K42-P45 viscosity model, while values of ρ_{mr} are similar for the two viscosity models.

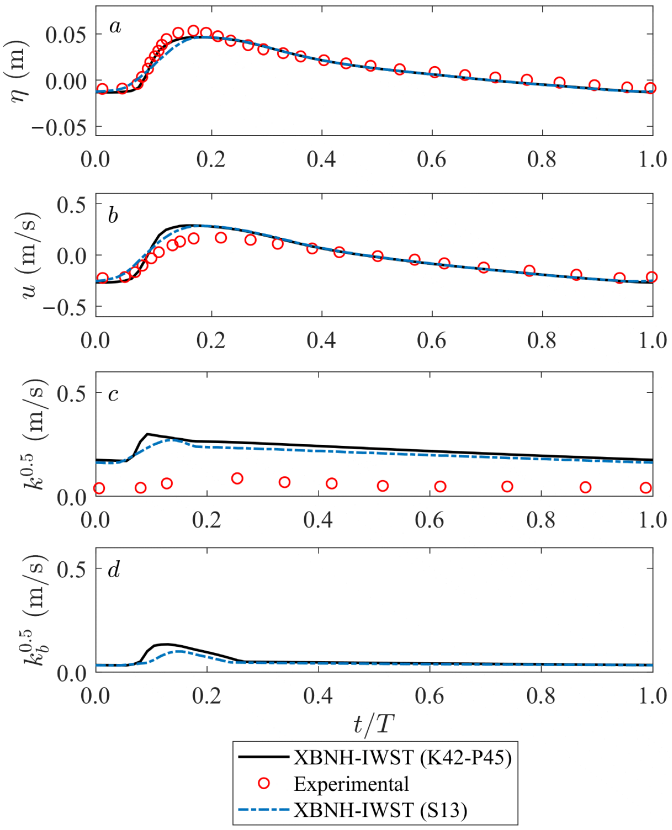

Figure 4.12: Time-varying phase-averaged quantities at $x = 9.7$ m; *a*: η; *b*: u ; *c*: $k^{0.5}$; *d*: $k_b^{0.5}$; comparison between the K42-P45 and S13 horizontal viscosity models

Table 4.7: nRMSE and ρ_{mr} for η, u and $k^{0.5}$

	nRMSE		ρ_{mr}	
	K42-P45	S13	K42-P45	S13
η	0.1284	0.1627	0.9962	0.9846
u	0.3276	0.2949	0.9845	0.9853
$k^{0.5}$	9.0634	7.9698	0.7554	0.7785

4.3.6 XBNH-IWST modelling of the Ting and Kirby (1994) experiments

In this section the XBNH-IWST predictions obtained with the calibrated KW92-A09 turbulence model and the S13 viscosity model set up as defined in Section 4.3.2 are compared with the experimental data of Ting and Kirby (1994) for both spilling and plunging breakers. Fig. 4.13*a*, *b* and *c* shows the distributions of η_{max}, η_{mean} and η_{min}, respectively, across the x-domain for the spilling breakers. The corresponding nRMSE are presented in Table 4.8. Results show that XBNH-IWST predicts the breaker point approximately 20 cm seaward of the observed one.

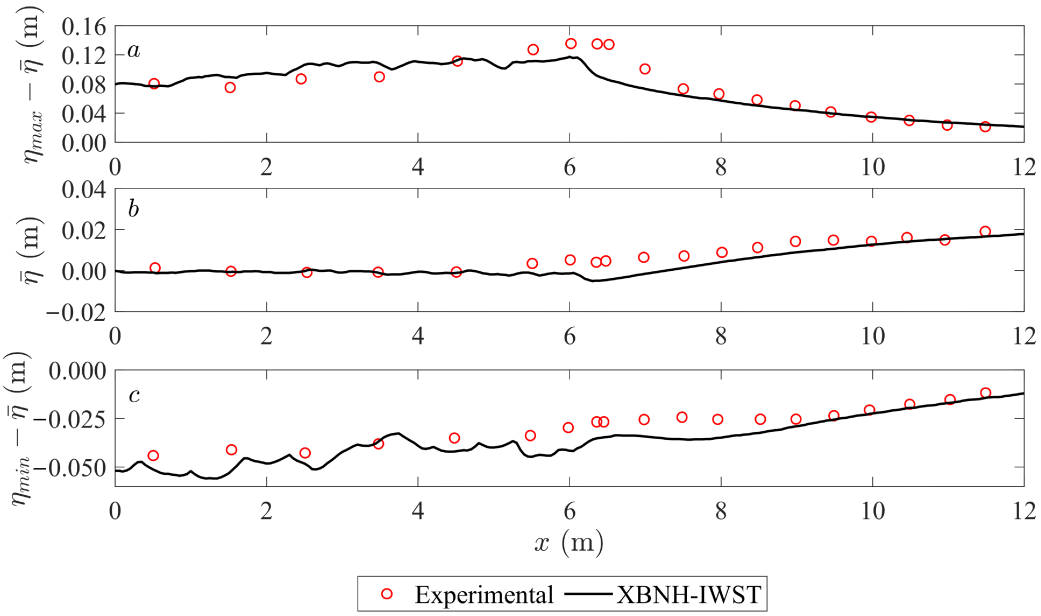

Figure 4.13: Distribution of surface elevation across the x-domain for the spilling breakers; *a*: η_{max}; *b*: η_{mean}; *c*: η_{min}

Table 4.8: nRMSE for η_{max}, η_{min} and $\bar{\eta}$

	nRMSE	
	Spilling	Plunging
η_{max}	0.3970	0.5332
η_{min}	1.0791	1.1107
$\bar{\eta}$	1.1669	0.5487

Fig. 4.14*a*, *b*, *c* and *d* shows the time-varying phase-averaged η, u, $k^{0.5}$ and $k_b^{0.5}$, respectively, at $x = 9.7$ m for the spilling breakers, with the corresponding nRMSE and ρ_{mr} in Table 4.9.

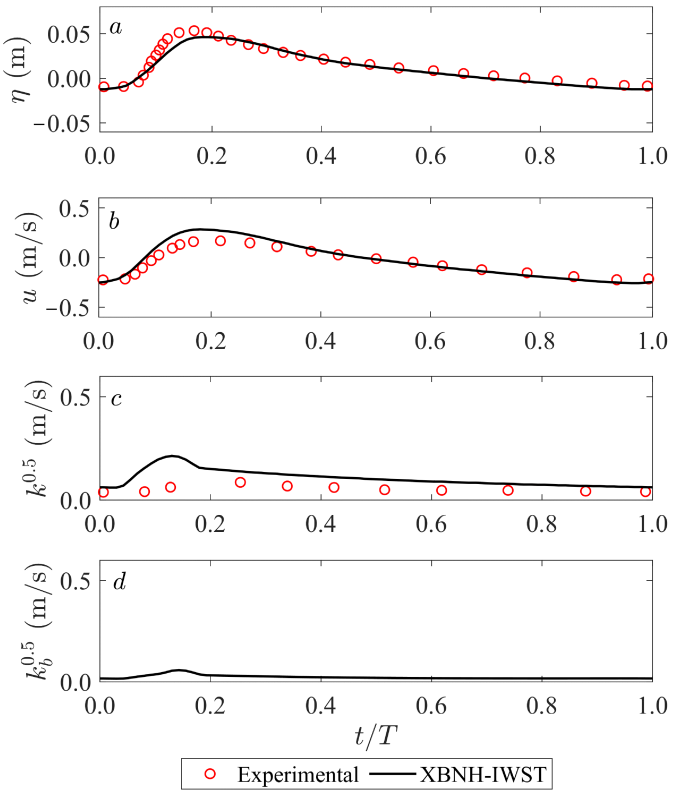

Figure 4.14: Time-varying phase-averaged quantities at $x = 9.7$ m for the spilling breakers; a: η; b: u; c: $k^{0.5}$; d: $k_b^{0.5}$

Table 4.9: nRMSE and ρ_{mr} for η, u and $k^{0.5}$

	Spilling		Plunging	
	nRMSE	ρ_{mr}	nRMSE	ρ_{mr}
η	0.1284	0.9962	0.4986	0.9640
u	0.3276	0.9845	0.3906	0.9818
$k^{0.5}$	3.2151	0.6548	1.5258	0.9828

Results for the plunging breakers are shown in Fig. 4.15a, b and c for η_{max}, η_{mean} and η_{min}, respectively, across the x-domain, with the corresponding nRMSE in Table 4.8. Fig. 4.16a, b, c and d shows the time-varying phase-averaged η, u, $k^{0.5}$ and $k_b^{0.5}$, respectively, at $x = 10.5$ m for the plunging breakers. The corresponding nRMSE and ρ_{mr} are presented in Table 4.9.

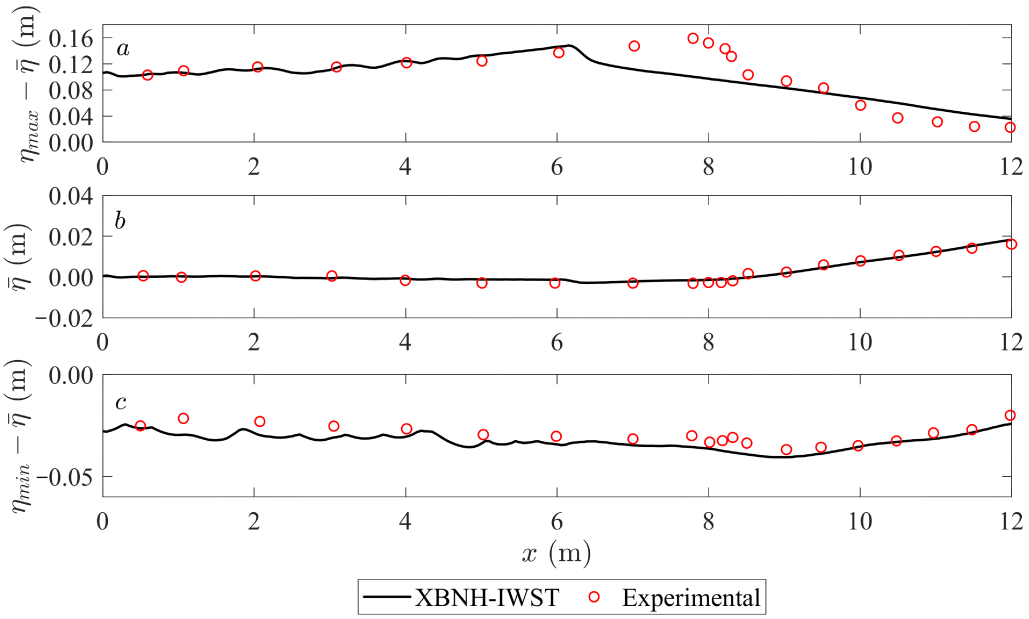

Figure 4.15: Distribution of surface elevation across the x-domain for the plunging breakers; *a*: η_{max}; *b*: η_{mean}; *c*: η_{min}

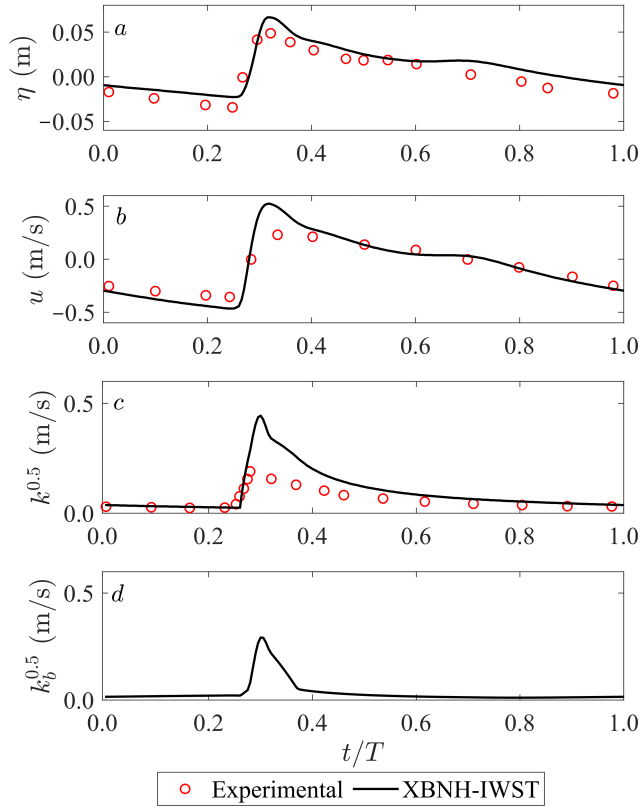

Figure 4.16: Time-varying phase-averaged quantities at $x = 10.5$ m for the plunging breakers; *a*: η; *b*: u; *c*: $k^{0.5}$; *d*: $k_b^{0.5}$

The accuracy of XBNH-IWST in the description of η_{max} for the plunging breakers is

lower by 25% compared to the spilling breakers. Due to the nature of its hydrodynamics governing equations, XBNH-IWST is not able to accurately capture the overturning jet observed for the plunging breakers, resulting in a discrepancy in η and u while the breaking-induced energy dissipation is quantitatively captured (see Fig. 4.15). The breaking point is predicted at a x-coordinate located more seaward of the observed one compared to the spilling breakers. As a consequence, the nRMSE for η is higher by 75% for the plunging breakers than the spilling breakers. XBNH-IWST overestimates the peak of u for the plunging breakers, whereas the shape of u is qualitatively well captured by the model for the spilling breakers. The nRMSE for u for the plunging breakers is higher by 18% than that for the spilling breakers.

For both cases, XBNH-IWST is able to qualitatively describe $k^{0.5}$. The accuracy in the prediction of $k^{0.5}$ in terms of nRMSE and ρ_{mr} is found to be higher for the plunging breakers, for which k was observed to vary over the water depth less than for the spilling breakers in the experiments.

5 XBNH-IWST model validation

5.1 Introduction

In this chapter, the hydro-morphodynamic model proposed in this study, i.e., XBNH-IWST, is validated by comparing its predictions to data from three laboratory experiments. The modelling of the intra-wave sediment transport, and in turn, of beach morphodynamics by XBNH-IWST is tested against two experimental case studies where sediment dynamics were studied for i) bichromatic wave groups and ii) consecutive, non-interacting solitary waves over sloped sandy beaches. For the former, a sensitivity analysis of the results to the parameters included in the Pritchard and Hogg (2003) sediment transport equation is also shown. For the two aforementioned test cases the XBNH-IWST performance is assessed both by considering the reference modelling configuration (i.e., without considering the effects of the wave breaking-generated TKE and $\nu_h = \nu_{h,s}$) and by taking into account the effects of TKE in combination with the additional horizontal viscosity model for the HFA (i.e., the S13 viscosity model). The former modelling configuration is similar to that used in Mancini et al. (2021); for the latter configuration the model set-up for the TKE and horizontal viscosity is the same as that used for the Ting and Kirby (1994) test case in Section 4.3.6.

The morphodynamic response of XBNH-IWST is also compared with the results obtained with XBNH-WAST (i.e., by using the Van Thiel de Vries, 2009; Van Rijn et al., 2007 sediment transport formulations). This comparison is also discussed in Mancini et al. (2021). In the cited study, results for XBNH-WAST are those obtained by Ruffini et al. (2020). Finally, the performance and robustness of XBNH-IWST is further assessed against laboratory experiments involving regular plunging breaker waves over a barred sandy beach, for which measurements of near-bed turbulence are also available. An overview of the three aforementioned test cases is first presented; then, the experimental set-up, model set-up and results for each case study are illustrated.

5.2 Test cases overview

The first two case studies considered in this chapter are the Alsina et al. (2016) and Young et al. (2010) experiments. The former involved bichromatic wave groups over an intermediate sandy beach, where swash-swash interactions were clearly present; in

the latter consecutive, non-interacting solitary waves were simulated over a 1:15 sloped sandy beach. The Alsina et al. (2016) experiments allow to assess the response of XBNH-IWST in terms of intra-swash sediment dynamics. The capability of the model proposed in this study to simulate the process of breaker bars development is also analysed. The Young et al. (2010) experiments are considered to further analyse the performance of XBNH-IWST to predict the intra-wave suspended sediment concentration and bed changes. For this test case measurements of the suspended sediment concentration are available at one location positioned a few meters seaward of the initial shoreline.

The third test case considered in this chapter concerns the Van der Zanden et al. (2016) experiments, which involved plunging breaking waves over a barred sandy beach where detailed measurements of velocities and turbulence in the surf zone were carried out. In the Van der Zanden et al. (2016) experiments a barred beach, where the bar trough was followed by a nearly horizontal mobile bed, was considered. This bed configuration is different from the monotonic sloping beach used in the previous two test cases. Therefore, the Van der Zanden et al. (2016) test is included to analyse the ability of XBNH-IWST to simulate the long bore-like propagation across the shelf extending shoreward of the bar trough where the vertical TKE decay is an important factor in the observed hydro-morphodynamics.

5.3 Numerical modelling of bichromatic wave groups over an intermediate beach

In this section, the performance of XBNH-IWST is assessed against the experiments conducted within the Hydralab IV - CoSSedM (Coupled high frequency measurement of Swash Sediment transport and Morphodynamics) project (see Alsina et al., 2016). The experimental and model set-up are first presented, then the sensitivity analysis for the parameters included in the Pritchard and Hogg (2003) equation and results are illustrated.

5.3.1 Experimental set-up

The Alsina et al. (2016) experiments studied the hydro-morphodynamics of bichromatic wave groups on a 1:15 sloped beach built at prototype scale with commercial sand (D_{50} = 0.25 mm, w_s = 0.034 m/s and n_p = 0.36), which showed clearly swash-swash

interactions. Two bichromatic wave groups conditions with the same energy content were generated in the flume: BE1_2 (broad-banded wave condition) and BE4_2 (narrow-banded wave condition), respectively, with varying wave group period, T_g, and repeat period, T_r. For BE1_2 $T_g = 15$ s and $T_r = 195$ s; whereas for BE4_2 $T_g = T_r = 27.7$ s (see also Alsina et al., 2018). $T_g = 1/f_g$ (with $f_g = f_1 - f_2$ being the group frequency, defined as the difference of the primary frequencies, f_1 and f_2). A summary of the simulated bichromatic wave groups is shown in Table 5.1, where H_1 and H_2 are the wave heights of the primary components.

Table 5.1: Wave periods, frequencies and wave heights for the bichromatic wave groups for wave conditions BE1_2 and BE4_2

	BE1_2	BE4_2
f_1 (Hz)	0.303	0.288
H_1 (m)	0.30	0.28
f_2 (Hz)	0.237	0.252
H_2 (m)	0.26	0.30
f_g (Hz)	0.067	0.036
T_g (s)	15	27.7
T_r (s)	195	27.7

For each wave condition, starting from the same initial z_b (1:15 uniform sloped bed), eight successive bichromatic waves sequences, from SEG1 to SEG8, each of 1800 s duration, were generated. Fig. 5.1 shows the initial z_b and the location of the instruments in the wave flume and selected for comparison. Wave Gauges (WG) and Acoustic Wave Gauges (AWG) measured η; Acoustic Doppler Velocimeters (ADV) measured the local flow velocity. Optical Back-Scattering (OBS) sensors and Conductivity Concentration Measurements (CCM$^+$) tanks measured C_z and time-dependent z_b in the swash zone, respectively. The offshore d in the horizontal part of the domain was 2.48 m for BE1_2 and 2.46 m for BE4_2. Following Gourlay and Van Der Meulen (1969) $1< \Omega <6$, therefore, the beach is classified as intermediate. Ω was computed using the definition in Section 2.2 and considering the root-mean-square wave height, H_{rms}, at WG3 (i.e., $H_{rms} = 0.39$ m for BE1_2 and $H_{rms} = 0.40$ m for BE4_2) and the mean primary wave period, $T_{pr} = 1/(f_1 + f_2)/2) = 3.70$ s, for both wave conditions. The reader is referred to Alsina et al. (2016) for a detailed description of the experimental procedure.

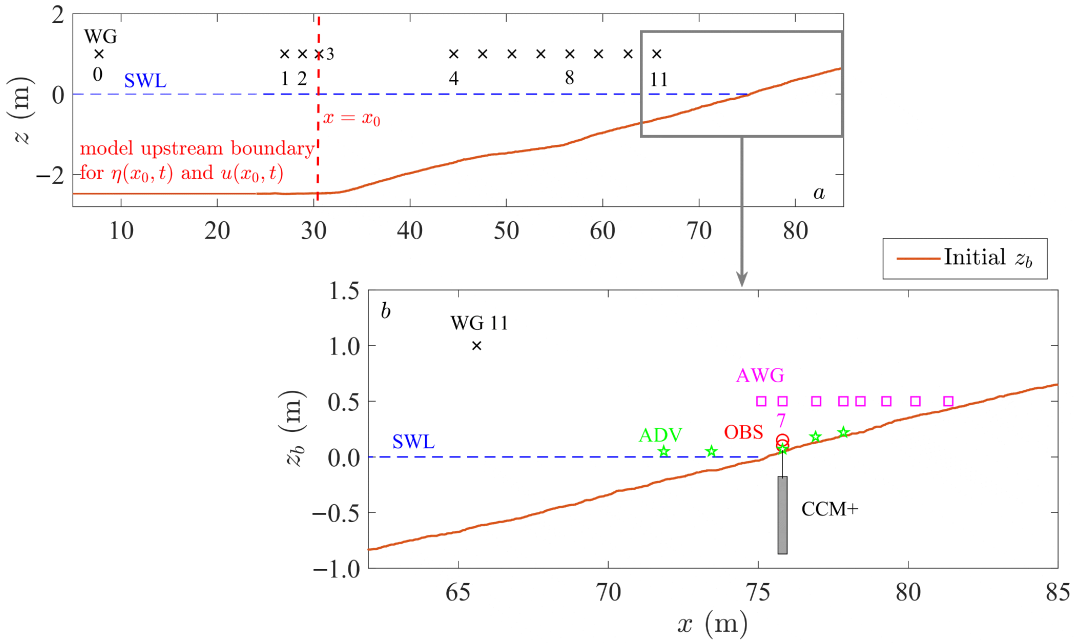

Figure 5.1: Alsina et al. (2016) experimental domain with the instrumentation considered for comparison with the present study and the upstream boundary location in the XBNH-IWST model domain (red-dashed line); *a*: whole domain; *b*: zoom-in of a portion of the domain in *a*

5.3.2 Model set-up

The model domain is shown in Fig. 5.1. The upstream boundary in the model is located at $x = x_0 = 30.55$ m, where the WG3 was installed. Hence, the model domain extended from WG3 to the end of the beach, located at $x = 85.05$ m and, following Ruffini et al. (2020), $\Delta x = 0.1$ m was defined. As in the Ting and Kirby (1994) case study, $h_{min} = 0.001$ m and $\alpha_{br} = 0.4$ were set. Time series of η and u (with a time resolution equal to $1{\times}10^{-3}$ s), provided as offshore forcing, were the same as those used in Ruffini et al. (2020) as boundary conditions. For the computation of c_f a slightly lower value of the Manning's coefficient, n, than in Ruffini et al. (2020) was used. $n = 0.018$ m$^{1/3}$s^{-1} was calibrated considering the best compromise between the accuracy of maximum run-up and morphological evolution. The value chosen reflects the characteristics of the considered sandy beach. As described in Section 3.3.2, $n_{p,d} = 0.6$ was chosen. Model parameters, which are not mentioned herein were set to their default values defined in Deltares (2018). The reader is referred to Appendix C for a full list of the model parameters and their values.

The calibration of the sediment transport model in XBNH-IWST was carried out

by varying m_e, R and λ. Table 5.2 summarises the main parameters included in the Pritchard and Hogg (2003) transport equation. This set of parameters was chosen as it provided the best modelling in the sensitivity analysis shown in Section 5.3.3.

Table 5.2: Main parameters and conditions in the Pritchard and Hogg (2003) transport equation

Parameters		Values
m_e	=	0.01 m/s
$\tau_{b,cr}$	=	0 N/m^2
λ	=	Considered wave height at the upstream boundary
τ_{ref}	=	$\rho c_{f,ref} u_{ref} \lvert u_{ref} \rvert$, where $c_{f,ref} = gn^2/\lambda^{1/3}$ and $u_{ref} = \sqrt{g\lambda}$
R	=	1.5
K_C	$\geq$	1 (computed by XBNH-IWST)

Simulations were carried out for both the reference modelling configuration (i.e., without considering the TKE effects and $\nu_h = \nu_{h,s}$), and by taking into account the contribution of the TKE. For the latter configuration, the model is set up as for the Ting and Kirby (1994) case for both the KW92-A09 turbulence model and the S13 viscosity model for the HFA. This modelling configuration is herein referred to as "*brkTurb*". This distinction is used only in Section 5.3.4. When not specified, the XBNH-IWST model takes into account the effects of the wave breaking-induced TKE and the additional ν_h modelling for the HFA. Table 5.3 summarises the parameters included in the KW92-A09 turbulence model and in the S13 horizontal viscosity model for the HFA within XBNH-IWST.

Table 5.3: Main parameters in the TKE and horizontal viscosity models

Parameters		Values
m_{cr}	=	0.1
γ_d	=	0.4
γ_k	=	1
μ	=	1

Only the first two segments, i.e., SEG1 and SEG2, were simulated for both BE1_2 and BE4_2, because they showed larger morphological changes than the subsequent ones. For BE1_2 the experimental bed evolution reached an equilibrium more rapidly

compared to BE4_2.

5.3.3 Sensitivity analysis of results to the parameters included in the Pritchard and Hogg (2003) transport equation

The sensitivity analysis of the results to the parameters used in the Pritchard and Hogg (2003) transport equation was carried out for SEG1 of BE1_2, without considering the effects of turbulence and by considering $\nu_h = \nu_{h,s}$. The aim of the sensitivity analysis is to show the relative effects of these parameters in terms of the modelled C and the bed changes after SEG1, i.e., $\Delta z_{b_f} = z_b(t = t_f, x) - z_b(0, x)$; t_f is the time at the end of SEG1. The parameters considered are m_e, R and λ. Note that λ also affects τ_{ref} (see Table 5.2) and K_C following Eqs. (13) and (15). According to Zhu and Dodd (2015), $\tau_{b,cr}$ is not analysed because the effect of a threshold for suspended load is negligible for fine sand, hence, $\tau_{b,cr} = 0$ N/m^2.

Each parameter is varied by keeping the others to their reference values as in Zhu and Dodd (2015) (i.e., $m_e = 0.002$ m/s, $\lambda = 1$ m and $R = 1$). m_e is the least well determined parameter due to the lack of data to provide its estimates. A back computation of m_e was previously carried out by using the experimental data of the CoSSedM project. Results are reported in Appendix D. Since $m_e = 0.002$ m/s is found to underestimate both Δz_{b_f} and C, the sensitivity analysis for m_e was carried out by increasing it by up to two orders of magnitude with respect to the reference value. $R > 0$ is a numerical parameter and it was increased and decreased with respect to $R = 1$ considering $R = 0.25$, 0.5 and 1.5. Values of λ were chosen to be physically representative of the Alsina et al. (2016) configuration. Therefore, $\lambda = H_{rms} = 0.39$ m and $\lambda = d = 2.48$ m at WG3 were selected.

Fig. 5.2 shows the sensitivity analysis for the parameters considered in terms of Δz_{b_f} (Fig. 5.2a, b and c) and C (Fig. 5.2d, e and f), respectively. The corresponding nRMSE, ρ_{mr} and RMSTE are presented in Tables 5.4 and 5.5. Note that the experimental C was computed as the average of the observed C_z at OBS4 and OBS7, which were located at two different d_z above the initial z_b at AWG7 (OBS4 at $d_z = 0.03$ m and OBS7 at $d_z = 0.08$ m). The OBSs did not measure when the free surface was lower than the instrument sensor. Therefore, the corresponding nRMSE and ρ_{mr} were computed when at least one of the two OBSs was submerged.

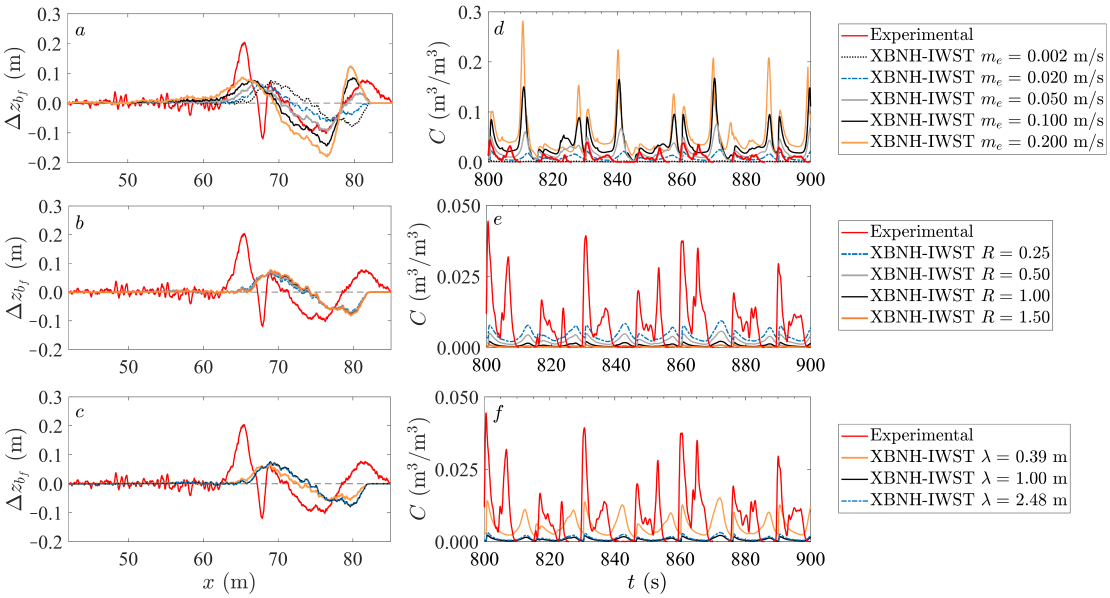

Figure 5.2: a, b and c: Δz_{b_f} after SEG1 for BE1_2 for different values of m_e, R and λ, respectively for; d, e and f: time series of C for different values of m_e, R and λ, respectively, for BE1_2; for each parameter the others are set to their reference values (i.e., m_e = 0.002 m/s, R = 1 and λ = 1 m); reference line: grey dashed-line. Note that the scale of the vertical axis of e and f is an order of magnitude lower than that of d.

The sensitivity analysis reveals that m_e is the most influencing parameter within the ranges considered in determining both the predicted C and Δz_{b_f}. Variations of λ and R affect C more than Δz_{b_f} in terms of nRMSE. By increasing λ or R, C decreases and the nRMSE increases due to the increasing underestimation of C. For both λ and R the maximum relative difference in terms of nRMSE is 14% (see Table 5.5). Instead, for m_e the difference between the maximum and minimum nRMSE is 73% (see Table 5.4). The sensitivity analysis shows that the variation of the parameters included in the Pritchard and Hogg (2003) equation leads to a variability of the peaks and magnitude of C, as a consequence of the variability of C. However, for all the parameters considered, the low ρ_{mr} indicates a poor correlation between the modelled and experimental C. In particular, the higher is the predicted C (and in turn its peaks), the lower is ρ_{mr}. For Δz_{b_f} variations of λ and R lead to negligible differences in terms of the corresponding nRMSE; differences in terms of RMSTE are lower than 6% and 2% for λ and R, respectively (see Table 5.5). Δz_{b_f} is quantitatively more sensitive to the variation of m_e, with the difference between the maximum and minimum RMSTE being 39% (see Table 5.4).

From a qualitative point of view, XBNH-IWST is able to capture the peak of the

accretion in the upper swash zone if m_e is increased by two orders of magnitude with respect to the values suggested in Zhu and Dodd (2015). In particular, the predicted erosion pattern in the upper swash region evolves into a deposition one for $m_e \geq 0.05$ m/s. Also, by increasing m_e, the erosion in the lower swash region increases and the peak of deposition in the surf zone moves seaward.

Table 5.4: nRMSE and ρ_{mr} for C; nRMSE and RMSTE for Δz_{b_f} for different values of m_e; note that the other parameters (i.e., R and λ) are considered at their reference values

		m_e (m/s)				
		0.002	0.02	0.05	0.1	0.2
C	nRMSE	1.1385	1.0195	1.7786	3.2594	3.8642
	ρ_{mr}	0.1319	−0.0784	−0.0997	−0.0688	−0.0532
Δz_{b_f}	nRMSE	0.0580	0.0484	0.0403	0.0397	0.0469
	RMSTE (m^2)	0.2836	0.2528	0.2541	0.2988	0.4178

Table 5.5: nRMSE and ρ_{mr} for C; nRMSE and RMSTE for Δz_{b_f} for different values R and λ; note that for each parameter the others are considered at their reference values

		R			λ (m)	
		0.25	0.5	1.5	0.39	2.48 m
C	nRMSE	1.0046	1.0696	1.1634	0.9757	1.1204
	ρ_{mr}	0.0344	0.0721	0.2164	0.1028	0.1486
Δz_{b_f}	nRMSE	0.0550	0.0565	0.0587	0.0519	0.0574
	RMSTE (m^2)	0.2902	0.2845	0.2859	0.2648	0.2810

Different combinations of values for m_e, λ and R were selected within the ranges considered for the model calibration. Results are shown in Fig. 5.3, with the corresponding nRMSE, ρ_{mr} and RMSTE presented in Table 5.6. Fig. 5.3 shows that by increasing m_e by an order of magnitude with respect to $m_e = 0.002$ m/s, in combination with different values of λ and R than their reference values, the predicted Δz_{b_f} and C (Fig. 5.3*a* and *b*) are qualitatively comparable to those obtained with $m_e \sim 10^{-1}$ m/s and the other parameters set to their reference values. None of the sets of parameters tested allow to obtain a better prediction of the time series of C. The combination $m_e = 0.01$ m/s, $\lambda = 0.39$ m and $R = 1.5$ was chosen for all the test cases considered in this study because it allows to better capture the magnitude of the deposition in the upper swash

zone and the erosion in the lower swash region. This is confirmed by the lower RMSTE compared to the other values tested.

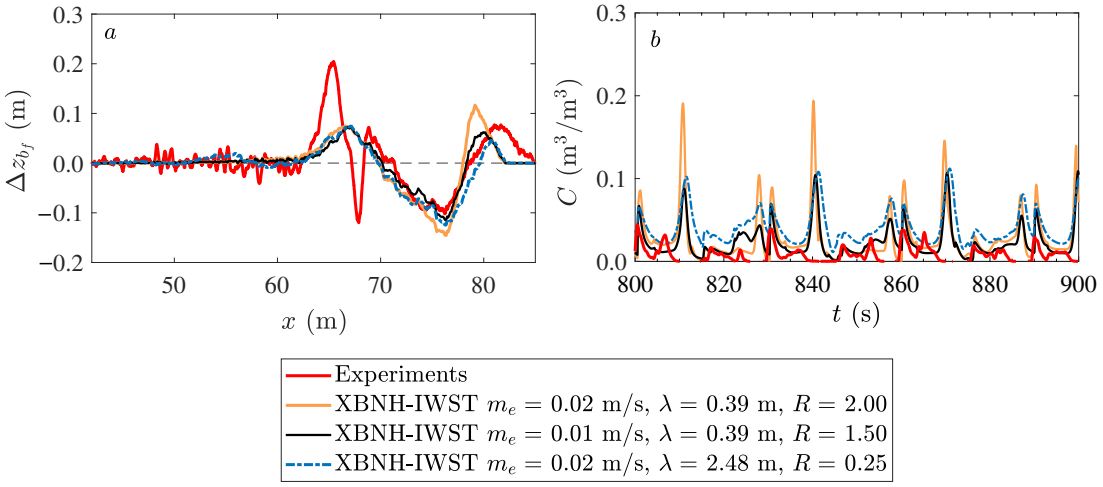

Figure 5.3: a: Δz_{b_f} after SEG1; b: time series of C over SEG1 for BE1_2 for different combinations of values of m_e, R and λ; reference line: grey dashed-line

Table 5.6: nRMSE and ρ_{mr} for C; nRMSE and RMSTE for Δz_{b_f} for different combinations of values of m_e, R and λ

	m_e (m/s)	0.02	0.01	0.02
	λ (m)	0.39	0.39	2.48
	R	2	1.5	0.25
C	nRMSE	2.8873	2.1614	3.0819
	ρ_{mr}	0.0921	0.0913	0.1314
Δz_{b_f}	nRMSE	0.0418	0.0412	0.0404
	RMSTE (m^2)	0.2328	0.2272	0.4221

The effect of varying m_e on suspended load

Suspended load-only simulations were carried out by turning off the bed load in XBNH-IWST. As for the sensitivity analysis illustrated above, TKE effects were not taken into account and $\nu_h = \nu_{h,s}$. Fig. 5.4 shows Δz_{b_f} normalised with the parameter, $M = m_e\sqrt{\lambda/g}/(1-n_p)$, for different values of m_e. λ and R are set to their reference values. The effect of varying m_e, and in turn, M can be seen; for $m_e \leq 0.005$ m/s the normalised Δz_{b_f} (Fig. 5.4*b*) are bigger in amplitude and show more noise, compared to the other values. This indicates that the predicted Δz_{b_f} is likely of the same order of magnitude of the numerical noise in the model for $m_e \leq 0.005$ m/s, and in the combined

load modelling the bed load would be dominating (or at least significant). By increasing m_e, and in turn, M, Δz_{b_f} become larger. In particular, the deposition in the upper swash zone and the erosion in the lower swash region increase as well as the deposition in the surf zone. For $m_e = 0.5$ m/s (i.e., $M = 0.25$ m), Δz_{b_f} are so large that the flow changes significantly because of the magnitude of Δz_{b_f} (Fig. 5.4*a*). Consequently, the normalised Δz_{b_f} (Fig. 5.4*b*) diverge from the results obtained with smaller values of m_e (i.e., $m_e = 0.1$ m/s and $m_e = 0.05$ m/s).

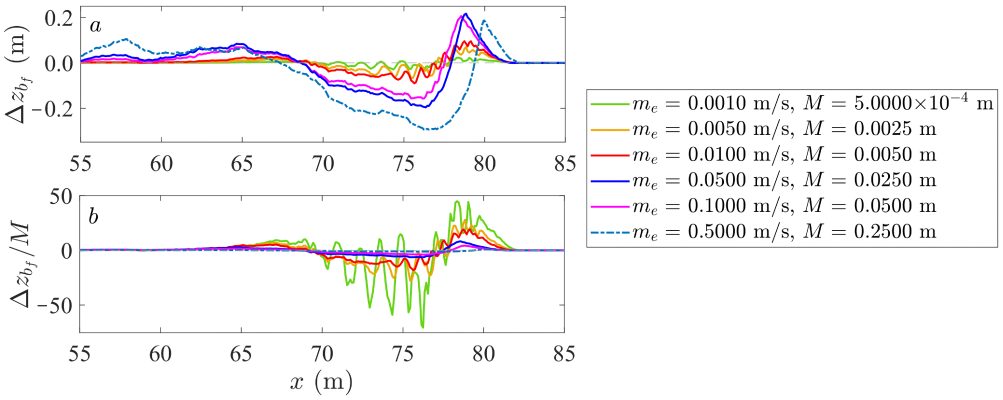

Figure 5.4: *a*: Δz_{b_f}; *b*: $\Delta z_{b_f}/M$ after SEG1 for BE1_2 for different values of m_e. Note that R and λ are set to their reference values; reference line: grey dashed-line

5.3.4 XBNH-IWST modelling of the Alsina et al. (2016) experiments

Figs. 5.5 and 5.6 show the time series of η and the spectral energy density, S_η, at WG4, WG8 and AWG7 for BE1_2 and BE4_2, respectively, with the corresponding nRMSE and ρ_{mr} shown in Table 5.7. According to Ruffini et al. (2020), XBNH is able to identify the super- and sub-harmonics of f_1 and f_2, hence to model the energy transfer between the frequency components for both wave conditions. For the *brkTurb* configuration (the results of which are referred to as XBNH-IWST (*brkTurb*) in the figures), differences are qualitatively significant at AWG7 (i.e., shoreward of the wave breaking point) with respect to the reference modelling configuration (i.e., without the inclusion of TKE effects and $\nu_h = \nu_{h,s}$). For the latter, spurious components are highlighted, especially at the uprush of each event within the wave groups. According to Smit et al. (2013), this noise is likely due to the discrete activation of the HFA which requires the model to adapt to the enforced hydrostatic pressure distribution.

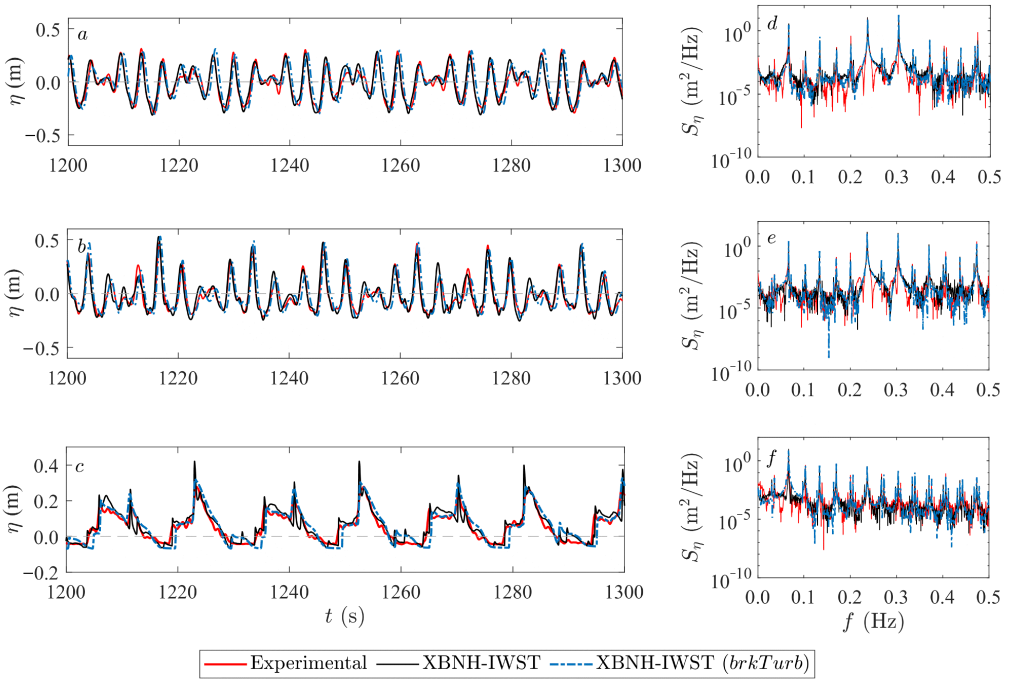

Figure 5.5: Time series and spectra of η at different locations for SEG2 of BE1_2; a and d: at WG4; b and e: at WG8; c and f: at AWG7; reference line: grey dashed-line

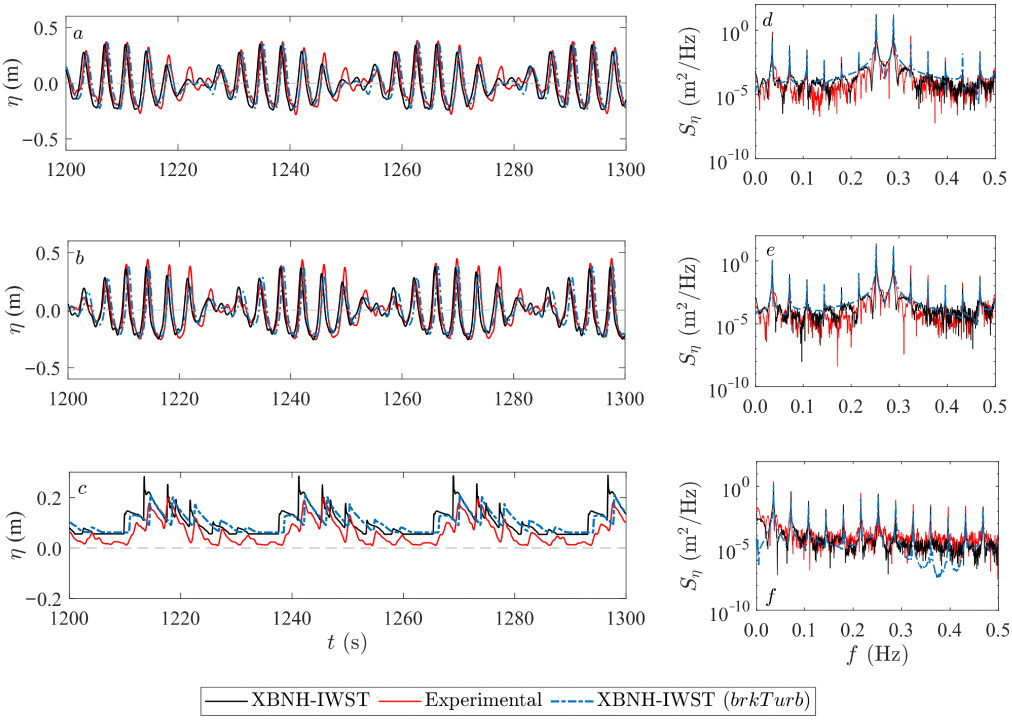

Figure 5.6: Time series and spectra of η at different locations for SEG2 of BE4_2; a and d: at WG4; b and e: at WG8; c and f: at AWG7; reference line: grey dashed-line

Table 5.7: nRMSE and ρ_{mr} for η at three locations: WG4 (x = 44.54 m), WG8 (x = 56.59) and AWG7 (x = 75.81 m), for wave conditions BE1_2 and BE4_2

	XBNH-IWST			
	nRMSE		ρ_{mr}	
	BE1_2	BE4_2	BE1_2	BE4_2
WG4	0.3427	0.2935	0.9434	0.9047
WG8	0.3703	0.3480	0.9319	0.7091
AWG7	0.6343	0.4928	0.8492	0.7387
	XBNH-IWST (*brkTurb*)			
	nRMSE		ρ_{mr}	
	BE1_2	BE4_2	BE1_2	BE4_2
WG4	0.3768	0.3737	0.9308	0.9277
WG8	0.4890	0.4257	0.8838	0.9053
AWG7	0.4802	0.6317	0.9166	0.8028

The effect of the additional horizontal viscosity modelling for the HFA is also highlighted in Figs. 5.7 and 5.8*a*, which show the distribution of H_{rms} across the x-domain for SEG2 of BE1_2 and BE4_2, respectively. For both wave conditions, XBNH-IWST is able to capture the evolution of H_{rms} across the x-domain. The *brkTurb* configuration allows to obtain a more pronounced dissipation throughout the inner surf zone and a higher accuracy by 15% for BE1_2 and 26% for BE4_2 in terms of nRMSE (see Table 5.8) with respect to the reference modelling configuration. z_{b_f} and the bed changes at the end of SEG2, i.e., $\Delta z_{b_f} = z_b(t = t_f, x) - z_b(0, x)$ (with t_f being the time at the end of SEG2), are illustrated in Figs. 5.7 and 5.8*b* and *c*, respectively; Table 5.8 presents the corresponding nRMSE and RMSTE. Numerical results show better performance for BE1_2 than BE4_2 for both modelling configurations. This is indicated by the lower nRMSE for BE1_2 compared to BE4_2. For the former, XBNH-IWST can capture the deposition in the upper swash zone and the erosion in the lower swash region, whereas the development of the breaker bar is not accurately simulated for both wave conditions. H_{rms} is more underestimated in the shoaling zone for BE4_2 than BE1_2. The experimental results suggest that reflection occurred in the shoaling zone due to the bar, therefore, H_{rms} increased more than the predicted one.

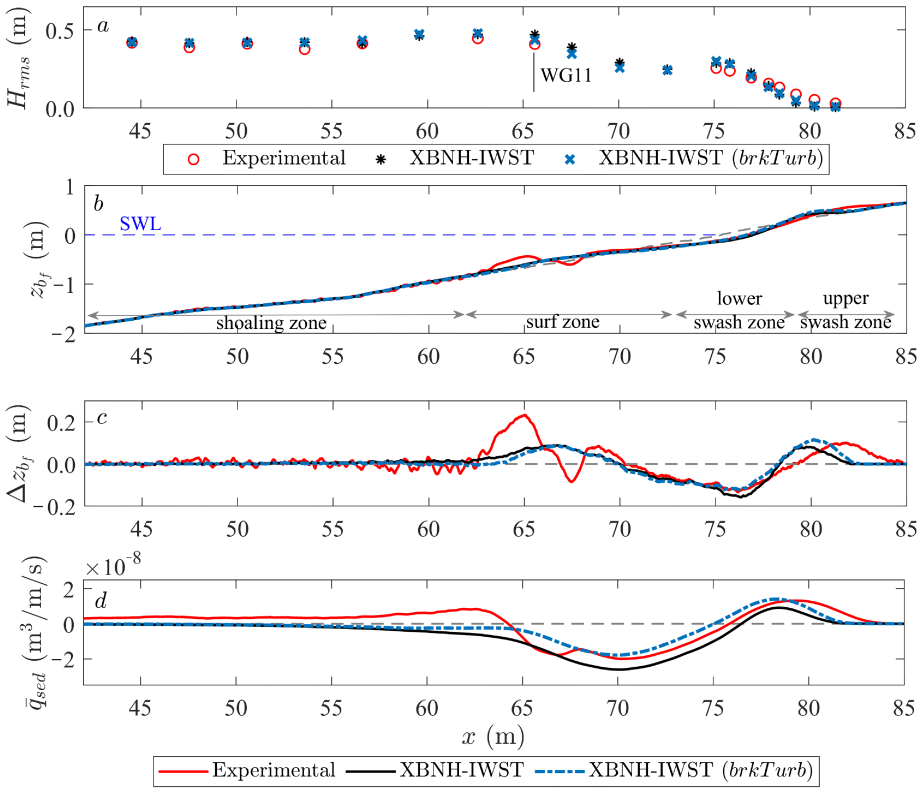

Figure 5.7: *a*: cross-shore profile of H_{rms} over SEG2; *b*: z_{b_f}; *c*: Δz_{b_f} after SEG2; *d*: $\bar{q}_{sed}$ over SEG1-2 for BE1_2; reference line: grey dashed-line

Table 5.8: nRMSE and RMSTE for Δz_{b_f} and H_{rms} across x BE1_2 and BE4_2

	XBNH-IWST			
	nRMSE		RMSTE (m^2)	
	BE1_2	BE4_2	BE1_2	BE4_2
Δz_{b_f}	0.0464	0.0712	0.4078	0.3217
H_{rms}	0.2402	0.3005		
	XBNH-IWST (*brkTurb*)			
	nRMSE		RMSTE (m^2)	
	BE1_2	BE4_2	BE1_2	BE4_2
Δz_{b_f}	0.0501	0.0715	0.3757	0.2972
H_{rms}	0.2041	0.2225		

Results indicate that the *brkTurb* modelling configuration slightly improves the prediction of the beach evolution, especially in the swash zone. The accuracy for Δz_{b_f} in terms

of nRMSE is comparable for the two modelling configurations, while the RMSTE for *brkTurb* is lower by approximately 10% for both BE1_2 and BE4_2 compared to the reference modelling configuration within XBNH-IWST.

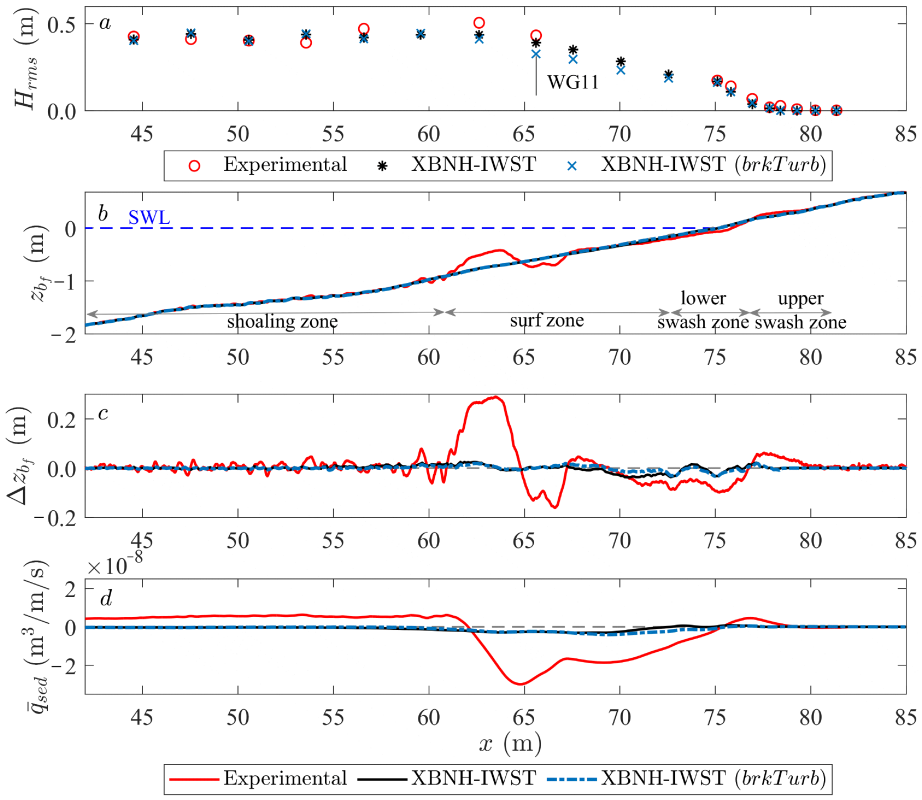

Figure 5.8: *a*: cross-shore profile of H_{rms} over SEG2; *b*: z_{b_f}; *c*: Δz_{b_f} after SEG2; *d*: $\bar{q}_{sed}$ over SEG1-2 for BE4_2; reference line: grey dashed-line

The net sediment transport rate, $\bar{q}_{sed}$, over SEG1 and SEG2 is shown in Figs. 5.7 and 5.8*d* for BE1_2 and BE4_2, respectively. This was computed using a sediment balance, which was numerically integrated over the x-domain between the start of SEG1 and the end of SEG2:

$$\bar{q}_{sed}(x = x_i) = \bar{q}_{sed}(x = x_{i-1}) - (1 - n_p)\frac{\Delta z_{b_{SEG1-2}} \Delta x}{\Delta t_{SEG1-2}}, \tag{45}$$

where q_{sed} is the instantaneous sediment transport and the bar refers to the averaging over the duration of the two segments, Δt_{SEG1-2}; the subscript i refers to the $i-$th point across the x-domain for both the numerical mesh and the experimental domain, where z_b is available. Therefore, $i = 1, ...N$, with i =1 at the onshore boundary of the domain (i.e., landward of the maximum run-up limit), where $q_{sed} = 0$ is assumed and

$i = N$ at the offshore start of the beach. $\Delta z_{b_{SEG1-2}}$ is the difference between z_b at the end of SEG2 and at the start of SEG1.

Fig. 5.7*d* indicates that XBNH-IWST is able to simulate the magnitude of the onshore-directed $\bar{q}_{sed}$ in the upper swash zone and the offshore-directed $\bar{q}_{sed}$ in the lower swash region and in the surf zone up to the crest of the bar located at $x = 65$ m. For BE4_2, the model can capture the sign of $\bar{q}_{sed}$ in the swash zone and up to the bar at $x = 63$ m (Fig. 5.8*d*), but the magnitude is underestimated. This is thought to be explained by the more prominent bar observed in BE4_2 than in BE1_2, which XBNH-IWST cannot simulate properly. Therefore, the exchange of sediment between the swash and surf zones is not well simulated, resulting in a deterioration in the overall modelling of $\bar{q}_{sed}$.

For both wave conditions, some limitations are visible in the shoaling region and surf zone up to the bar crest, where the experimental onshore-directed $\bar{q}_{sed}$ is not predicted by the model. When the experimental $\bar{q}_{sed}$ changes in sign, the modelled one continues being negative for both wave conditions. Note that the modelled θ at the offshore side of the bar is larger than θ_{cr} for the most part of the event. For BE4_2 the observed $\bar{q}_{sed}$ goes to zero at the offshore boundary, which is not shown in Fig. 5.8*d*. However, the positive and quasi-uniform value of the observed $\bar{q}_{sed}$ in the shoaling zone is most likely affected by measurement effects due to the mechanical wheel profiler used to measure the bed level. This instrument has a wheel that is too large to detect individual ripples. Therefore, the change in the bed level is below the sensitivity of the instrument.

The *brkTurb* modelling configuration is found to improve the magnitude of q_{sed} in the surf zone as well as to increase the onshore directed q_{sed} in the swash zone for BE1_2. However, the process of the breaker bar development is not properly described yet. Simulations were also carried out by varying the value of γ_k, however, the results did not show an improvement in the prediction of the beach evolution (see Appendix E).

Additional simulations were carried out by considering the acceleration effects in the computation of the bed shear stress according to Nielsen (2002). This modelling approach was already implemented in XBNH. However, an improvement of the morphodynamics response of XBNH-IWST was not obtained. Therefore, results are not further discussed in this section and the reader is referred to Appendix F. A detailed

analysis of the local sediment transport dynamics within SEG2 at AWG7 (x = 75.81 m) is shown in Figs. 5.9 and 5.10 for BE1_2 and BE4_2, respectively. Note that the experimental u is a local measurement over the vertical direction and herein assumed depth-uniform for comparison with the modelled one.

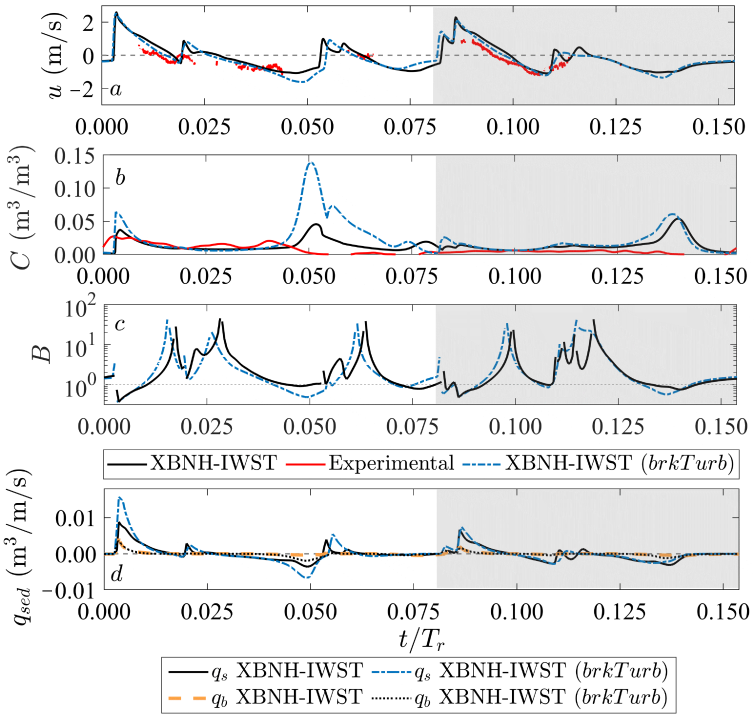

Figure 5.9: Time series of flow and sediment transport variables at AWG7 (x = 75.81 m) over SEG2 for BE1_2; *a*: u; *b*: C; *c*: B; *d*: q_s and q_b; the shaded area distinguishes the two wave groups; reference line: grey-dashed line

For BE1_2, only two groups are selected from the sequence of groups within T_r over SEG2. Fig. 5.9*b* shows the time series of C. The corresponding nRMSE and ρ_{mr} are shown in Table 5.9. XBNH-IWST is able to capture the magnitude of C after the first bore within each group, hence the suspension of the sediment generated by swash-swash interactions. However, the model overestimates the peaks of C corresponding to the first bore and the last backwash events within each group, especially at $t/T_r \sim 0.05$ and $t/T_r \sim 0.1375$. The overestimation of C is larger for the *brkTurb* modelling configuration compared to the reference one. This is thought to be due to the higher magnitude of the predicted peak of u at the aforementioned backwash stages and to the enhanced predicted suspension (i.e., C) at the uprush phase of the flow due to the inclusion of turbulence. Similarly, the magnitude of the corresponding modelled q_s and q_b is higher when *brkTurb* is applied compared to the reference modelling configuration. For both

modelling configurations, q_s is always higher than q_b (Fig. 5.9*d*). In the broad-banded wave condition large backwash events are allowed to develop. Therefore, the sediment suspension is dominant over settling.

Table 5.9: nRMSE and ρ_{mr} for u, C and C_z (at OBS4 and OBS7) at $x = 75.81$ m for BE1_2 and BE4_2

	XBNH-IWST			
	nRMSE		ρ_{mr}	
	BE1_2	BE4_2	BE1_2	BE4_2
u	0.5706	0.8526	0.6443	0.5103
C	1.5428	5.9385	0.1247	0.2696
C_z (OBS4)	1.0665	3.0683	0.3319	0.3033
C_z (OBS7)	1.0805	2.4130	0.1809	0.2148
	XBNH-IWST (*brkTurb*)			
	nRMSE		ρ_{mr}	
	BE1_2	BE4_2	BE1_2	BE4_2
u	0.4428	0.6910	0.6401	0.6852
C	2.8291	5.9464	0.2452	0.2536
C_z (OBS4)	3.2017	2.9574	0.1766	0.2871
C_z (OBS7)	1.5277	2.1436	0.1109	0.2095

BE4_2 (see Fig. 5.10) allows to analyse results within one group over SEG2, since $T_r = T_g$. Note that the observed u was filtered with a low-pass filter (cut-off frequency set to 3 Hz) to remove the noise in the measurements. Similarly to BE1_2, XBNH-IWST is able to capture the order of magnitude of the observed C after the first event due to swash-swash interactions occurring in the group. The accuracy in the prediction of u is higher when *brkTurb* is applied, compared to the reference modelling configuration within XBNH-IWST (see Table 5.9). However, like in the broad-banded wave condition, the model overestimates C during the backwash phase of the flow. For both modelling configurations, the peak of C corresponding to the first wave (at $t/T_r \sim 0.095$) is likely the result of a larger bore-induced transport than the experiments. The use of the *brkTurb* modelling configuration does not improve the description of C. For BE4_2, the accuracy in the prediction of C in terms of nRMSE and ρ_{mr} is found to be comparable

between the two modelling configurations.

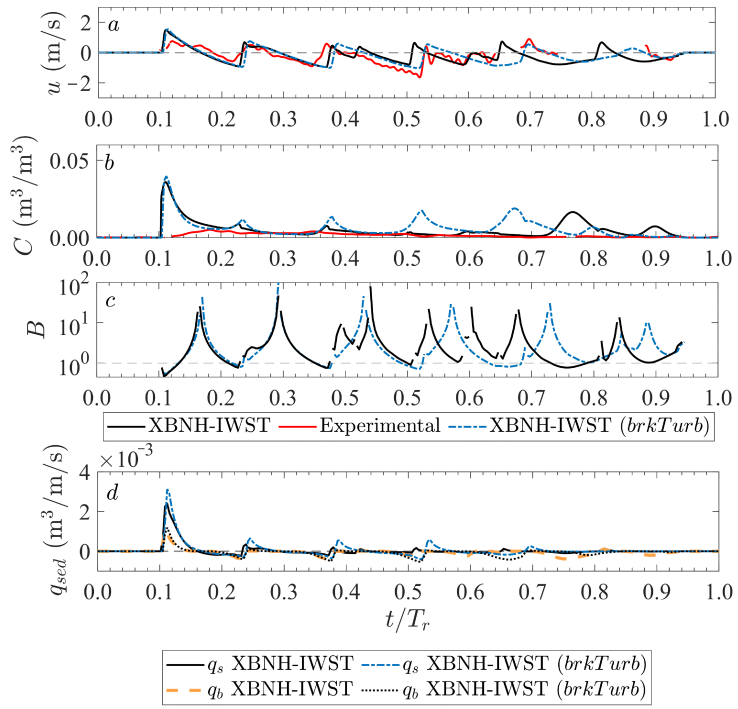

Figure 5.10: Time series of flow and sediment transport variables at AWG7 ($x = 75.81$ m) over SEG2 for BE4_2; *a*: u; *b*: C; *c*: B; *d*: q_s and q_b; reference line: grey-dashed line

In BE4_2 a higher number of swash-swash interactions occurred within each group than in BE1_2. Therefore, the backwashes corresponding to the subsequent events were allowed to develop for a shorter duration compared to the broad-banded wave condition. Consequently, the experimental and modelled C are lower and the difference between the modelled q_s and q_b (Fig. 5.10*d*) is smaller than in BE1_2. $q_b > q_s$ during the backwash events within the group.

Time series of B for both BE1_2 and BE4_2 are shown in Figs. 5.9 and 5.10*d*, respectively. Note that the values corresponding to $u = 0$ m/s were not plotted to avoid the high spikes due to the zero value of u. The trend of B reflects the degree of banding, which characterises the two wave conditions analysed. For BE1_2, a large swash excursion is allowed to develop within the groups, and consequently, large backwashes. In turn, the acceleration of the flow within the backwash allows B to drop below 1, especially when *brkTurb* is applied. $B < 1$ indicates that the turbulent diffusion is dominant with respect to the sediment settling. A strong seaward sediment transport is promoted, which is confirmed by the larger values of C than BE4_2. In the narrow-banded wave condition, except for the first bore, B is mostly higher than 1 for the subsequent events

within the group.

The experimental time series of z_b recorded by the CCM+ tank at $x = 75.81$ m was used to compute C_z for the same d_z as OBS4 and OBS7, respectively, with Eq. (16). Results are shown in Figs. 5.11 and 5.12*b* and *c* for both BE1_2 and BE4_2, with the corresponding nRMSE and ρ_{mr} shown in Table 5.9. Similarly to the results shown in Figs. 5.9 and 5.10, when *brkTurb* is applied C_z is overestimated, especially within the first wave group for BE1_2 and at the first uprush for BE4_2. As expected, the overall accuracy of XBNH-IWST in terms of nRMSE is higher for C_z than C. However, the ρ_{mr} for C_z is affected by the underestimation of C_z close to flow reversal. This indicates that, even when more accurate, the model does not capture the correct behaviour of the parameters in time. The corresponding nRMSE and ρ_{mr} reflect the lower performance of XBNH-IWST in predicting the intra-wave sediment transport compared to the hydrodynamics modelling (see Tables 5.7 and 5.9).

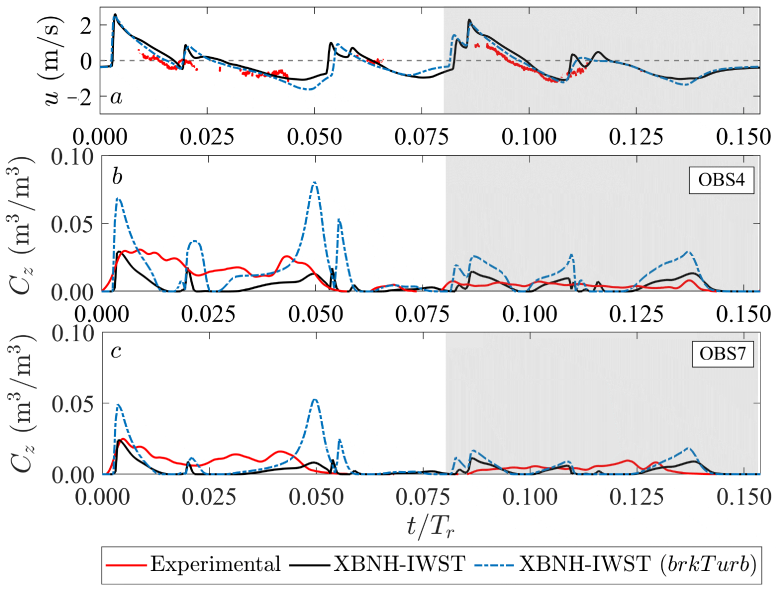

Figure 5.11: Time series of flow and sediment transport variables at AWG7 ($x = 75.81$ m) over SEG2 for BE1_2; *a*: u; *b*: C_z at OBS4; *c*: C_z at OBS7; the shaded area distinguishes the two wave groups; reference line: grey-dashed line

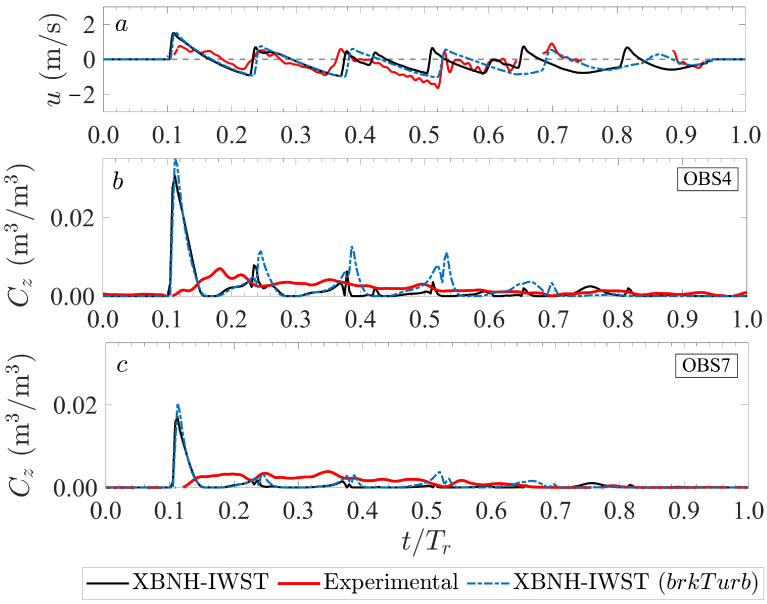

Figure 5.12: Time series of flow and sediment transport variables at AWG7 ($x = 75.81$ m) over SEG2 for BE4_2; *a*: u; *b*: C_z at OBS4; *c*: C_z at OBS7; reference line: grey-dashed line

Figs. 5.13 and 5.14 *b* and *c* show the time series of k and $k_{b_{tot}}$ over SEG2 of BE1_2 and BE4_2, respectively, for XBNH-IWST considering the *brkTurb* modelling configuration.

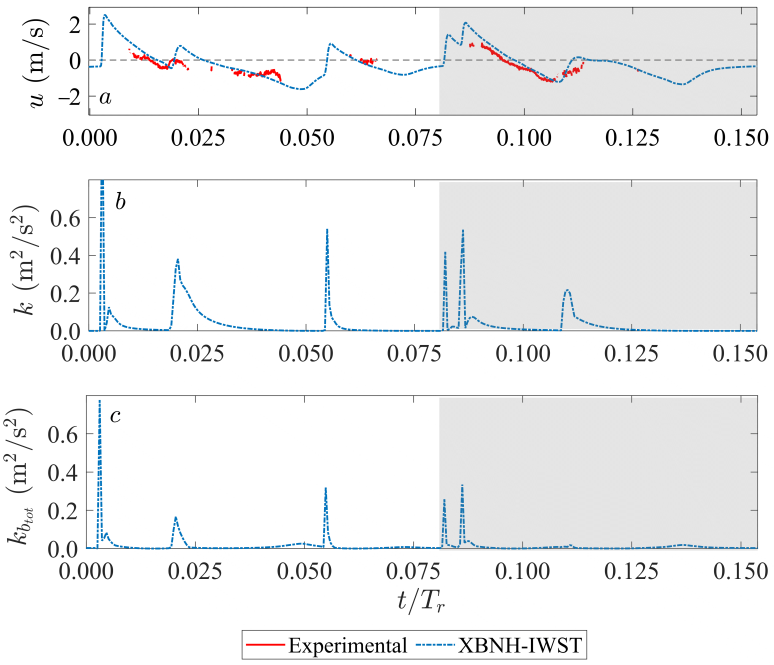

Figure 5.13: Time series of the hydrodynamics at AWG7 ($x = 75.81$ m) over SEG2 for BE1_2; *a*: u; *b*: k; *c*: $k_{b_{tot}}$; reference line: grey-dashed line. Note that the maximum value of k in *b* is 1.26 m^2/s^2.)

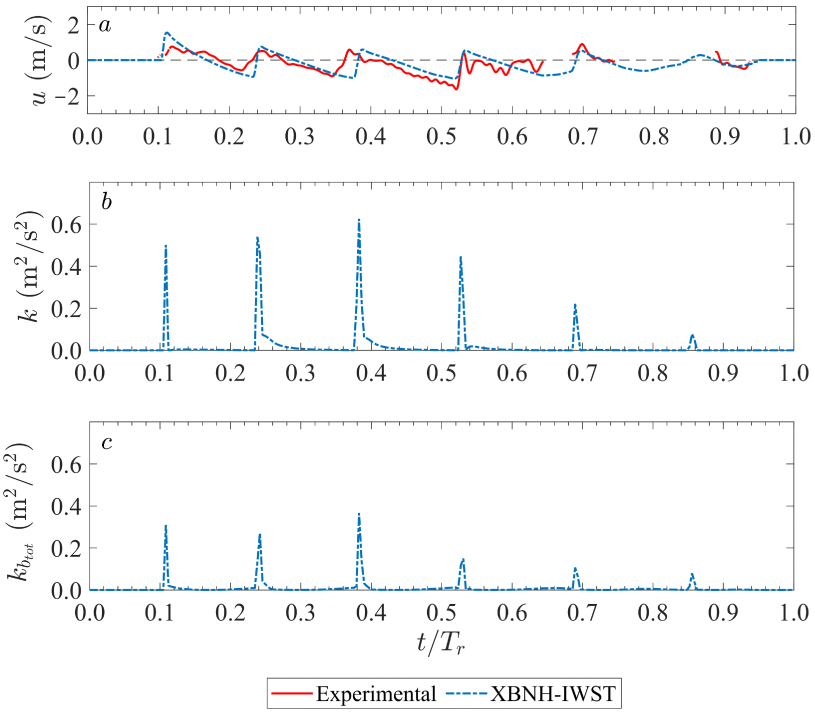

Figure 5.14: Time series of the hydrodynamics at AWG7 ($x = 75.81$ m) over SEG2 for BE4_2; *a*: u; *b*: k; *c*: $k_{b_{tot}}$; reference line: grey-dashed line

For both wave conditions $k_{b_{tot}} > k$ over the latest stage of the backwash events. This means that the turbulence due to bed friction is larger than the wave breaking-induced turbulence. Unlike the reference modelling configuration within XBNH-IWST, the peaks of C_z during the uprush phases of the flow computed with XBNH-IWST when *brkTurb* is used are influenced by the peaks of $k_{b_{tot}}$.

The effect of the diffusion term in the Pritchard and Hogg (2003) transport equation

Fig. 5.15 shows Δz_{b_f} (Fig. 5.15*a*) after SEG1 and the time series of u (Fig. 5.15*b*) and C (Fig. 5.15*c*) over SEG1 of BE1_2 for $D_C = \nu_h$ (see also Section 3.6) and $D_C = 0$. Results show that the effect of the diffusion term in the Pritchard and Hogg (2003) transport equation (see Eq. (11)) is to increase C, especially during the backwash events within the wave groups. The corresponding nRSME is 18% higher compared to $D_C = 0$. However, for $D_C = 0$, the ρ_{mr} is an order of magnitude lower than for $D_C = \nu_h$. For $D_C = 0$, the deposition in the surf zone is slightly shifted onshore than that predicted with $D_C = \nu_h$, however, differences in terms of the overall Δz_{b_f} are difficult to discern; RMSTE = 0.3314 m^2 for the former and RMSTE = 0.3359 m^2 for the latter.

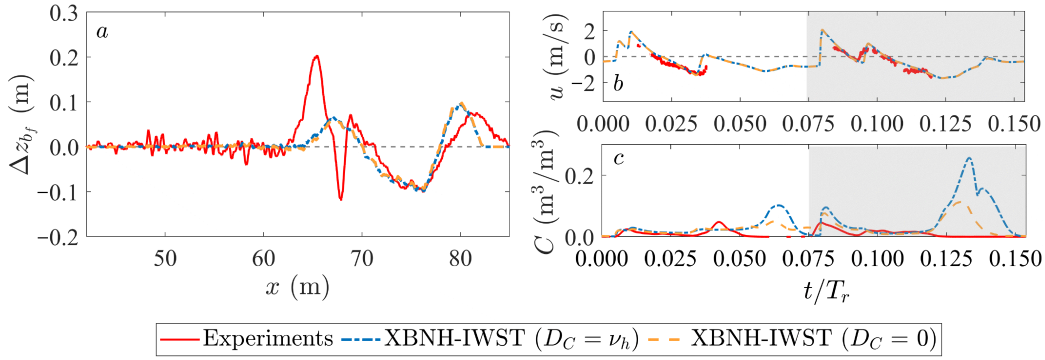

Figure 5.15: *a*: Δz_{b_f} after SEG1 of BE1_2; *b*: time series of u over SEG1 of BE1_2; *c*: time series of C over SEG1 of BE1_2. Comparison between results for $D_C = \nu_h$ and $D_C = 0$; reference line: grey dashed-line; the grey shade distinguishes the two wave groups in *b* and *c*.

Table 5.10: nRMSE and ρ_{mr} for C at $x = 75.81$ m for SEG1 of BE1_2 for $D_C = \nu_h$ and $D_C = 0$

	$D_C = \nu_h$	$D_C = 0$
nRMSE	2.7874	2.2600
ρ_{mr}	−0.1136	0.0147

Numerical modelling of BE4_2-SEG2 with imposed bar

Numerical simulations were carried out for SEG2 of BE4_2 by considering z_{b_f} at the end of SEG1, where the breaker bar was already developed, to analyse the model behaviour and compare it with the results shown previously. Fig. 5.16 shows the time-averaged velocity, $\bar{u}$ (Fig. 5.16*a*), over SEG2, Δz_{b_f} (Fig. 5.16*b*) after SEG2 and $\bar{q}_{sed}$ over SEG2 (Fig. 5.16*c*); the *brkTurb* modelling configuration was used. Note that $\bar{q}_{sed}$ was computed over the duration of SEG2, Δt_{SEG2}. Results indicate that XBNH-IWST, in presence of the bar, improves the predictions of Δz_{b_f} after SEG2 and $\bar{q}_{sed}$ over the same segment. XBNH-IWST better models the erosion and deposition patterns in terms of Δz_{b_f} and $\bar{q}_{sed}$ when the measured z_{b_f} after SEG1 is considered, from a qualitative point of view. However, the development of the breaker bar, and in turn, the gradient of $\bar{q}_{sed}$ in the surf zone (immediately seaward of the bar crest) are not accurately captured. The corresponding RMSTE = 0.2675 m^2 is 11% lower compared to that in Table 5.8. For $x > 68$ m the modelled $\bar{u}$ is similar for the two initial bed configurations, and XBNH-IWST can capture the magnitude of $\bar{u}$ in the upper and lower swash zone. Note that the experimental $\bar{u}$ was computed using the observed time series of u. Differences in the

distribution of $\bar{u}$ are visible in the surf zone for $62 \leq x \leq 68$ m, where the breaker bar developed in the experiments, for the two initial bed configurations. However, measurements of u are not available in the surf zone and a comparison with the experiments in this region cannot be carried out.

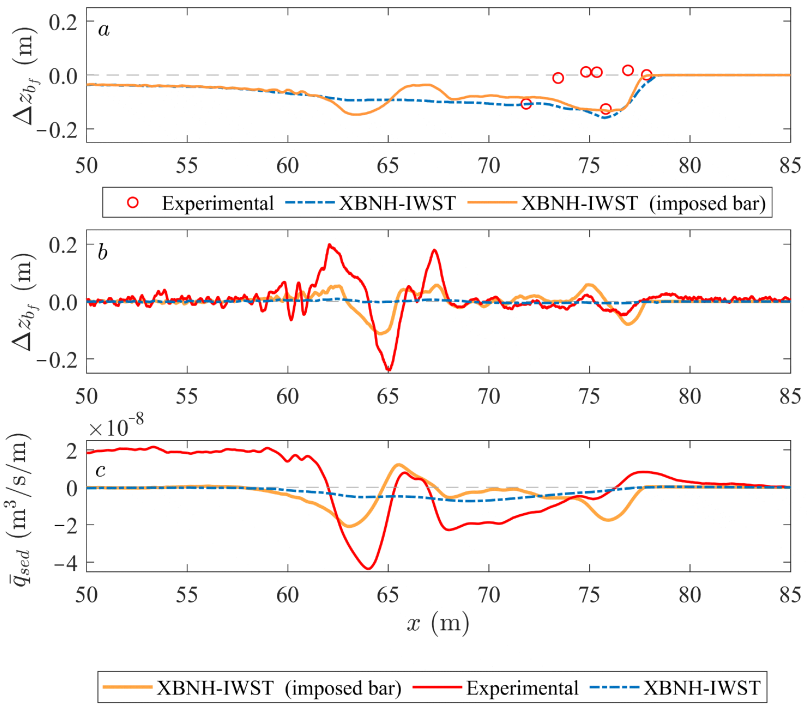

Figure 5.16: a: $\bar{u}$ over SEG2; b: Δz_{b_f} after SEG2; c: $\bar{q}_{sed}$ over SEG2 for BE4_2. Comparison between simulations carried out with the measured z_{b_f} after SEG1 (imposed bar) and with the predicted z_{b_f} after the same segment; reference line: grey dashed-line

Fig. 5.17 illustrates the time series of u (Fig. 5.17a), C (Fig. 5.17b) and huC (Fig. 5.17c) for SEG2 of BE4_2. The first peak of C (i.e., at $t/T_r = 0.11$) is less prominent when the bar is imposed compared to that predicted when the modelled z_{b_f} after SEG1 is used. Consequently, the nRMSE for C shown in Table 5.11 is lower than that for the latter configuration (see also Table 5.9). However, the predicted time histories of C are qualitatively similar for both the initial bed configurations used. For both cases, XBNH-IWST overestimates C during the subsequent backwashes events and values of ρ_{mr} for C are similar (see also Table 5.9). This is also reflected by the time series of huC (Fig. 5.17c).

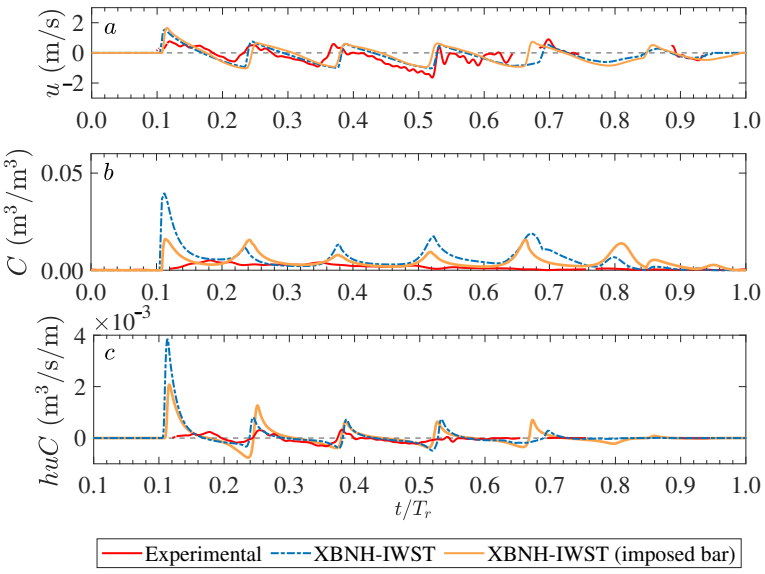

Figure 5.17: Time series of flow and sediment transport variables at AWG7 ($x = 75.81$ m) over SEG2 for BE4_2; *a*: u; *b*: C; *c*: huC. Comparison between simulations carried out with z_{b_f} after SEG1 (imposed bar) and with the predicted z_{b_f} after the same segment; reference line: grey-dashed line

Table 5.11: nRMSE and ρ_{mr} for C at $x = 75.81$ m for SEG2 of BE4_2 when the bar is imposed by considering the measured z_{b_f} after SEG1

	nRMSE	ρ_{mr}
C	4.6241	0.1256

5.3.5 Comparison between XBNH-IWST and XBNH-WAST

In this section results for the sediment transport, and in turn, for the morphodynamics modelling of XBNH-WAST and XBNH-IWST are compared. Similarly to Ruffini et al. (2020), the Van Thiel de Vries (2009) and Van Rijn (2007) sediment transport formulations were used within XBNH-WAST, but unlike the cited study the model was set up as the reference modelling configuration within XBNH-IWST (Ruffini et al., 2020 used $n = 0.02$ m$^{1/3}$s^{-1} and did not considered the diffusion term in the sediment transport equation for the suspended sediment concentration; also, in the cited study $\alpha_{br} = 0.6$ was used). Fig. 5.18 shows the time series of C predicted by XBNH-IWST and XBNH-WAST predictions for SEG2 of BE1_2 and BE4_2, respectively. The corresponding nRMSE and ρ_{mr} in Table 5.12. For XBNH-IWST the nRMSE for C is higher than that

for XBNH-WAST, while ρ_{mr} for C is higher for the former than for the latter. XBNH-IWST is able to obtain the magnitude of the sediment suspension (i.e., C) observed after the first bore generated by swash-swash interactions within each group and C at flow reversal. Similarly to Ruffini et al. (2020), C predicted with XBNH-WAST reaches values close to zero near flow reversal unlike the experiments.

Table 5.12: nRMSE and ρ_{mr} for C for BE1_2 and BE4_2, respectively; comparison between XBNH-IWST and XBNH-WAST

	XBNH-IWST	XBNH-WAST	XBNH-IWST	XBNH-WAST
	BE1_2		BE4_2	
nRMSE	2.8192	1.5101	5.9464	2.4851
ρ_{mr}	0.2452	0.0290	0.2017	0.0139

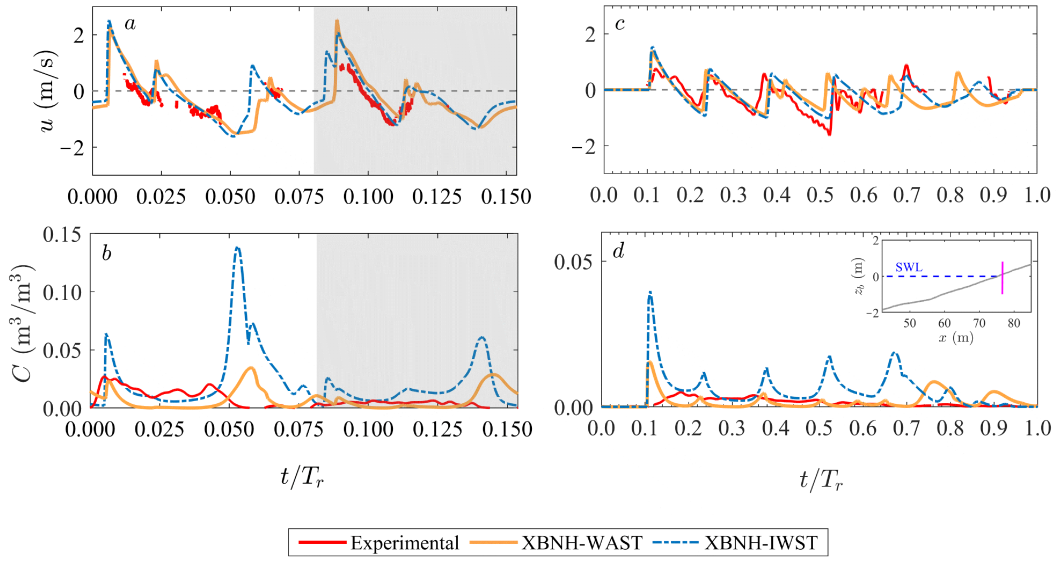

Figure 5.18: Time series of flow and sediment transport variables at AWG7 ($x = 75.81$ m) over SEG2 for BE1_2 (a and b) and BE4_2 (c and d): a and c: u; b and d: C. Comparison between XBNH-IWST and XBNH-WAST; the shaded area distinguishes the two wave groups; reference line: grey-dashed line; the subplot in d shows the x-coordinate across the domain.

Differences in the predictions of C for the two approaches lead in turn, to differences in the simulated Δz_{b_f} (Fig. 5.19a and c).

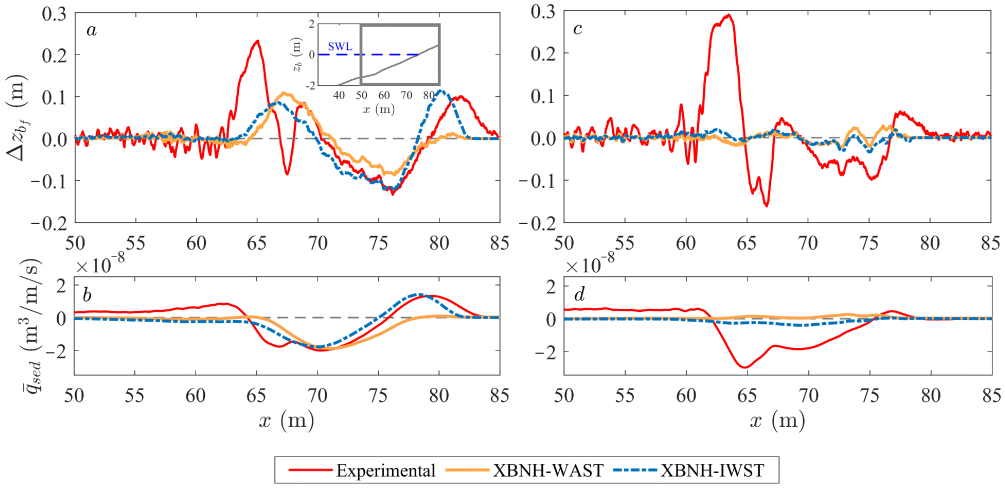

Figure 5.19: a and c: Δz_{b_f} after SEG2; b and d: $\bar{q}_{sed}$ over SEG2 for BE1_2 (a and b) and BE4_2 (c and d), respectively. Comparison between XBNH-IWST and XBNH-WAST; reference line: grey dashed-line; the grey rectangle in a shows the region of the domain selected for the results in the main plots.

XBNH-IWST shows a better performance in the prediction of Δz_{b_f} than XBNH-WAST, especially for BE1_2. The RMSTE for XBNH-IWST is 12% lower than that for XBNH-WAST, while values of the nRMSE are similar for both models (see Table 5.13). XBNH-IWST is capable of simulating the deposition in the upper swash zone and the erosion in the lower swash region. Instead, Δz_{b_f} predicted with XBNH-WAST diverge from the experiments, especially in the upper swash zone. This is likely explained by the behaviour of the sediment transport model in XBNH-IWST near flow reversal, when sediment particles are allowed to settle. The RMSTE for the region shoreward of $x = 72$ m is 56% and 27% lower for XBNH-IWST than for XBNH-WAST for BE1_2 and BE4_2, respectively. The better performance of XBNH-IWST than XBNH-WAST is confirmed by the modelling of $\bar{q}_{sed}$ (Fig. 5.19b and d). XBNH-WAST underestimates the magnitude of $\bar{q}_{sed}$ in the swash zone for BE1_2, and does not capture the sign of $\bar{q}_{sed}$ for BE4_2, unlike XBNH-IWST.

Table 5.13: nRMSE and RMSTE for Δz_{b_f} for BE1_2 and BE4_2, respectively; comparison between XBNH-IWST and XBNH-WAST

	XBNH-IWST	XBNH-WAST	XBNH-IWST	XBNH-WAST
	BE1_2		BE4_2	
nRMSE	0.0501	0.0580	0.0715	0.0762
RMSTE (m^2) total	0.3757	0.4252	0.2972	0.2982
RMSTE (m^2) $x \geq 72$ m	0.0770	0.1766	0.0813	0.1115

5.4 Numerical modelling of consecutive, non-interacting solitary waves over a sloped beach

In this section the performance of XBNH-IWST is further tested with the experiments of an erodible sloped beach exposed to nine consecutive, non-interacting solitary waves presented in Young et al. (2010). As with the Alsina et al. (2016) test case, a comparison between XBNH-IWST and XBNH-WAST performance is also illustrated.

5.4.1 Experimental set-up

Fig. 5.20 shows the experimental set-up and the location of the instrumentation installed in Young et al. (2010) and considered for comparison in this study.

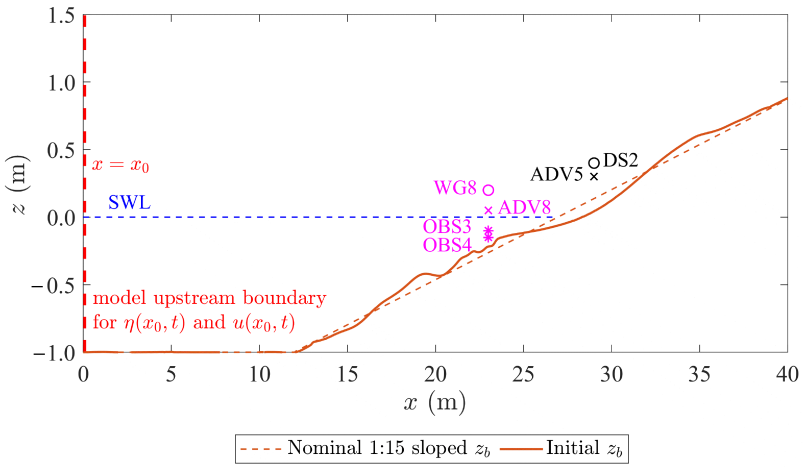

Figure 5.20: Young et al. (2010) experimental domain with instrumentation installed and location of the upstream boundary in the model domain (red-dashed line)

For η, WG8 ($x = 23$ m) and the Distance Sonic, DS2 ($x = 29$ m) sensors were considered. For u, ADV8 ($x = 23$ m) and ADV5 ($x = 29$ m) sensors were selected. For the suspended

sediment concentration OBS3 and OBS4 sensors were considered (x = 23 m). They recorded C_z at two different d_z from the initial z_b (OBS3 at d_z = 0.19 m and OBS4 at d_z = 0.09 m). The initial z_b is a wave-modified 1:15 sloped beach, made of well sorted sand with D_{50} = 0.2 mm and n_p = 0.4. This configuration was the result of previous runs on the nominal 1:15 sloped z_b, such that it can be considered as a near-equilibrium profile beach state.

5.4.2 Model set-up

The model domain was set up following the experimental settings described in detail in Young et al. (2010). The computational domain was $x_0 = 0 \leq x \leq 40$ m and Δx = 0.05 m. Like the previous test case, h_{min} = 0.001 m and α_{br} = 0.4 were chosen. The initial wave-modified z_b was used as the initial z_b in the simulations. As shown in Fig. 5.20, time series of η and u were provided at the upstream boundary located at $x = x_0$ (with a time resolution of 1×10^{-3} s), and were given by Titov and Synolakis (1995), considering a solitary wave over the offshore d = 1 m where the bed is horizontal:

$$\eta(x_0,t) = H\mathrm{sech}^2\left[\sqrt{\frac{3H}{4d^3}}(ct - x_0)\right], \tag{46}$$

where H = 0.60 m and u is:

$$u(x_0,t) = \eta(x_0,t)\sqrt{\frac{g}{h}}. \tag{47}$$

Moreover, to be consistent with the experiments, reflection was taken into account at the upstream boundary (i.e., by using the function ARC = 0 available in XBNH; see also Deltares, 2018). The sediment transport model was set up similarly to the Alsina et al. (2016) test case (see Table 5.2), with $\lambda = H$. c_f was modelled using $n = 0.025$ m$^{1/3}$s^{-1}, which was chosen by matching the simulated maximum run up with the experiments. The maximum excursion point was observed at x = 38.5 m. As in the previous test case, $n_{p,d}$ = 0.6 was defined. Parameters that were not mentioned in this study, were set to their default values defined in Deltares (2018). The reader is referred to Appendix C for the full list of the model parameters and their values. Numerical simulations were performed for the first three waves of the nine experimental runs. Following the experimental procedures, the simulated time for each wave was 900

s, in order to allow the water to calm. As for the previous test case, simulations were carried out with both the reference modelling configuration within XBNH-IWST (i.e., without considering the TKE effects and $\nu_h = \nu_{h,s}$) and by applying *brkTurb* (i.e., the KW92-A09 turbulence model and the S13 viscosity model). For the latter see also Table 5.3. Distinction between the two modelling configurations are considered only in Section 5.4.3. When not specified, the XBNH-IWST model takes into account the effects of the wave breaking-induced TKE and the additional ν_h modelling for the HFA.

5.4.3 XBNH-IWST modelling of the Young et al. (2010) experiments

Fig. 5.21 shows the numerical and experimental time series of η and u within one wave at selected x-locations. The corresponding nRMSE and ρ_{mr} are shown in Table 5.14. In general, XBNH-IWST is able to capture the hydrodynamics for the Young et al. (2010) experiments. However, a shift of 4 s in the prediction of the reflected wave generated by the finite size of the flume is visible. Considering the 99% of the volume contained in a solitary wave, it is possible to compute the corresponding wave length (Dean and Dalrymple, 1991) and in turn, the wave period, which is equal to 7.71 s. Therefore, the aforementioned shift represents, approximately, the 52% of the wave period for the considered solitary wave.

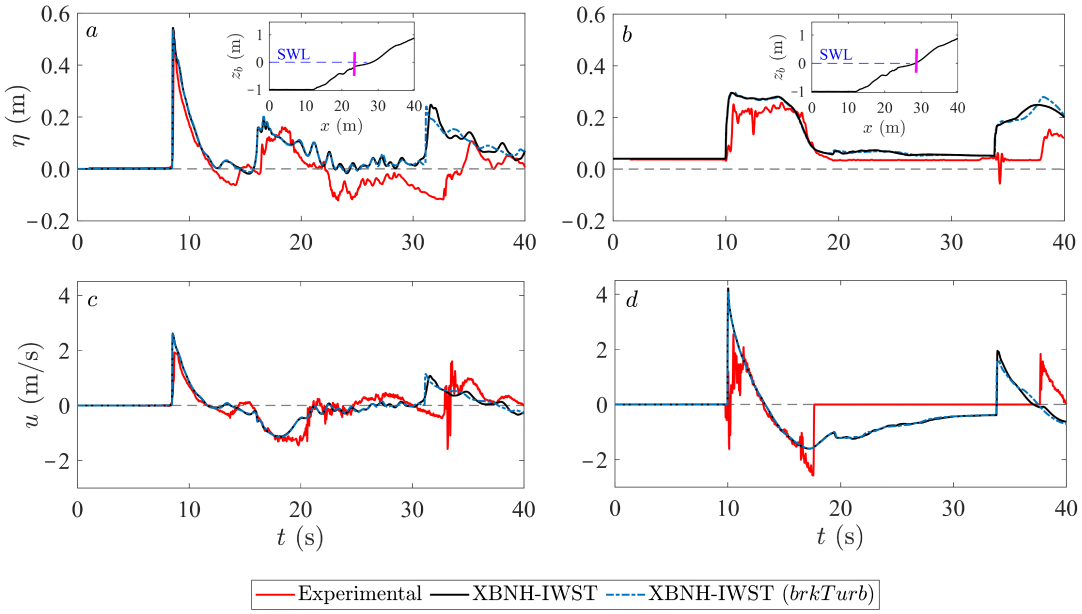

Figure 5.21: Time series of flow variables; *a* and *b*: η at WG8 ($x = 23$ m) and DS2 ($x = 29$ m); *c* and *d*: u at ADV8 ($x = 23$ m) and ADV5 ($x = 29$ m); reference line: grey-dashed line. The two subplots in *a* and *b* show the cross-shore location of the sensors in the model domain.

For WG8 and ADV5, the nRMSE is higher and ρ_{mr} is lower compared to those for other sensors (see Table 5.14). At WG8 (Fig. 5.21*a*) the average overestimation of η after the wave rundown, including the reflected wave (i.e., for $t > 22$ s) is equal to 8% for both modelling configurations. Comparison at ADV5 (Fig. 5.21*d*) is affected by some noise in the collected signal at $t = 10$ s and when the water level dropped down the sensor ($17 < t < 37$ s), hence no signal was recorded.

Table 5.14: nRMSE and ρ_{mr} for η, u and C at selected positions

		XBNH-IWST		XBNH-IWST (*brkTurb*)	
		nRMSE	ρ_{mr}	nRMSE	ρ_{mr}
WG8	η	1.1839	0.5612	1.1494	0.5847
ADV8	u	0.7095	0.7465	0.7593	0.7163
DS2	η	0.9819	0.7642	1.0198	0.7538
ADV5	u	1.4419	0.4609	1.3432	0.4892
OBS3-4	C	5.7473	0.5296	5.8174	0.5303

Fig. 5.22 shows z_{b_f} (Fig. 5.22*a*) and the bed changes after 3 waves (Fig. 5.22*b*), Δz_{b_f} ($z_{b_f} = z_b(x, t_f)$, with t_f being the time at the end of the third run).

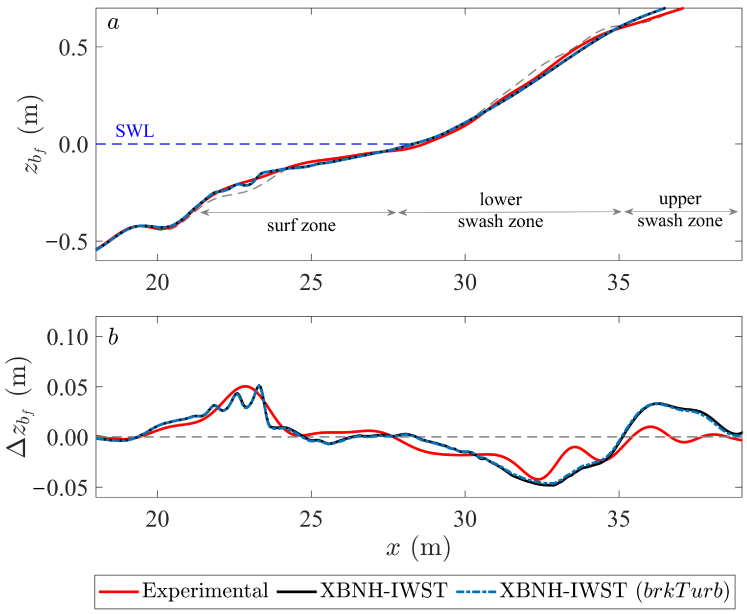

Figure 5.22: *a*: z_{b_f}; *b*: Δz_{b_f} after 3 waves; reference line: grey-dashed line

Despite XBNH-IWST overestimating the deposition in the upper swash zone and the

erosion in the lower swash region for $x > 30.5$ m, XBNH-IWST is able to simulate the observed erosion and deposition patterns. From a quantitative point of view this is confirmed by the corresponding nRMSE and RMSTE, which are shown in Table 5.15. Results indicate that the effects of wave breaking-induced turbulence are almost negligible in terms of morphodynamics response of the model. This is also confirmed by the predictions of the intra-wave sediment dynamics shown in Fig. 5.23.

Table 5.15: nRMSE and RMSTE for Δz_{b_f} after 3 waves

	XBNH-IWST	XBNH-IWST (*brkTurb*)
nRMSE	0.0227	0.0218
RMSTE	0.0866	0.0862

Fig. 5.23 illustrates an analysis of the intra-wave sediment transport within one wave at $x = 23$ m. Time series of C are shown in Fig. 5.23*b*. Note that the experimental C was computed as the average of the observed C_z at OBS3 and OBS4. The corresponding computed nRMSE and ρ_{mr} are shown in Table 5.14.

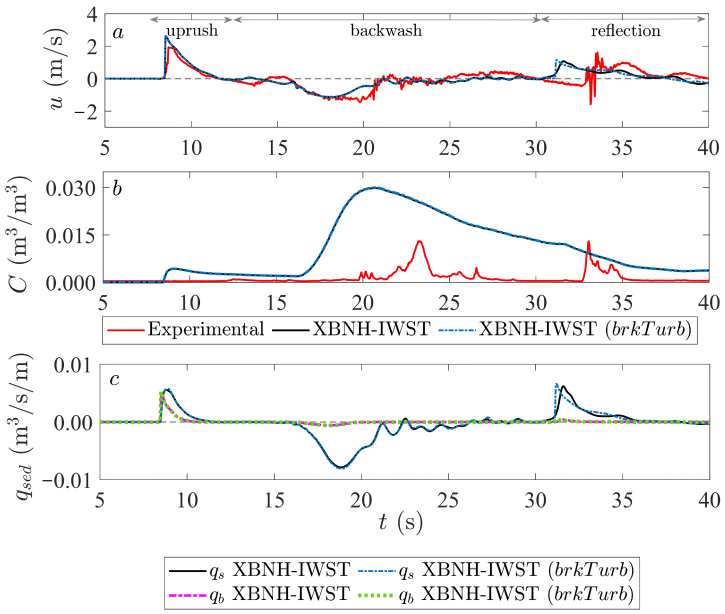

Figure 5.23: Time series of flow and sediment transport variables at $x = 23$ m; *a*: u; *b*: C; *c*: q_s and q_b; reference line: grey-dashed line

For both the experiments and numerical predictions, the largest peak of C corresponds to the backwash phase of the flow. The peak of the experimental C is shifted in time with

respect to the modelled one, possibly due to the shift between the observed and modelled reflection (for $t > 30$ s), which interacted with the wave rundown. As indicated in Young et al. (2010), the suspended sediment concentration was observed to vary a lot along the depth. Therefore, discrepancies between observations and numerical predictions are due to some limitations of the model performance, but uncertainty in the comparison exists because of the low resolution of the measurements. The accuracy in terms of nRMSE and ρ_{mr} for C is similar for the two modelling configurations.

Time series of the modelled q_s and q_b are shown in Fig. 5.23*c*. At the early stage of the uprush $q_b \simeq q_s$. This is consistent with the experiments, since the experimental C is nearly zero at the uprush, which means that sediment motion mainly occurred as near-bed sediment transport. As indicated in Young et al. (2010), the OBS sensors were located seaward of the wave plunging point (see also Fig. 5.20). As the stirred up sediment is entrained in the water column, the contribution of the modelled q_s also increases. Close to flow reversal sediment settling occurs and both predicted q_s and q_b decrease. Then, the magnitude of q_b and q_s increase until $q_s > q_b$ in the later stage of the backwash.

Time series of the modelled k and $k_{b_{tot}}$ at $x = 23$ m and $x = 29$ m are shown in Figs. 5.24*a* and *b* and 5.24*c* and *d*, respectively. At both selected x-coordinates ($x = 23$ m in the inner surf zone and $x = 29$ m in the swash zone), $k_{b_{tot}} > k$ for most part of the wave cycle, except for the peaks at the uprush and at the backwash events (the latter only at $x = 23$ m).

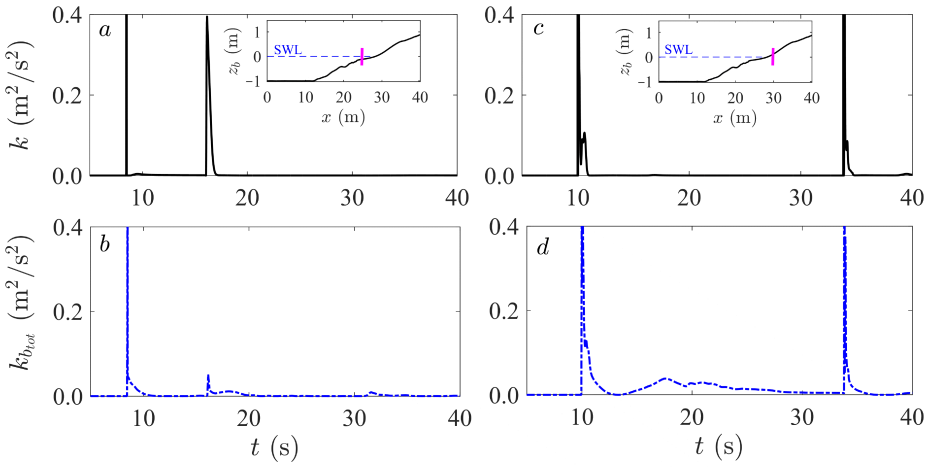

Figure 5.24: Time series of k and $k_{b_{tot}}$ at different x-coordinates; *a* and *b*: at $x = 23$ m; *c* and *d*: at $x = 29$ m; the subplots in *a* and *c* show the cross-shore locations in the model domain.

A peak of k is also predicted at the arrival of the reflected wave at $x = 29$ m. $k_{b_{tot}} > k$ indicates that the effect of the bed-induced turbulence is dominant over the wave breaking-generated one. This could explain the almost indiscernible difference between the two modelling configurations in terms of Δz_{b_f} and C.

5.4.4 Comparison between XBNH-IWST and XBNH-WAST

In this section the predictions of XBNH-IWST, using *brkTurb*, are compared to those obtained with the XBNH-WAST model. XBNH-WAST was set up as the reference modelling configuration within XBNH-IWST and as for the Alsina et al. (2016) case study, the Van Thiel de Vries (2009) and Van Rijn (2007) sediment transport formulations were used.

Fig. 5.25*a* and *b* shows z_{b_f} and Δz_{b_f} after 3 waves, with the corresponding nRMSE and RMSTE in Table 5.16. Results show that unlike XBNH-IWST, XBNH-WAST is not able to model the erosion and deposition patterns accurately in terms of Δz_{b_f}. For the XBNH-WAST approach, the nRMSE is 35% higher and the RMSTE is 84% higher than those computed for XBNH-IWST. Differences in terms of Δz_{b_f} are in turn, due to differences in the predictions of the intra-wave C between the two models.

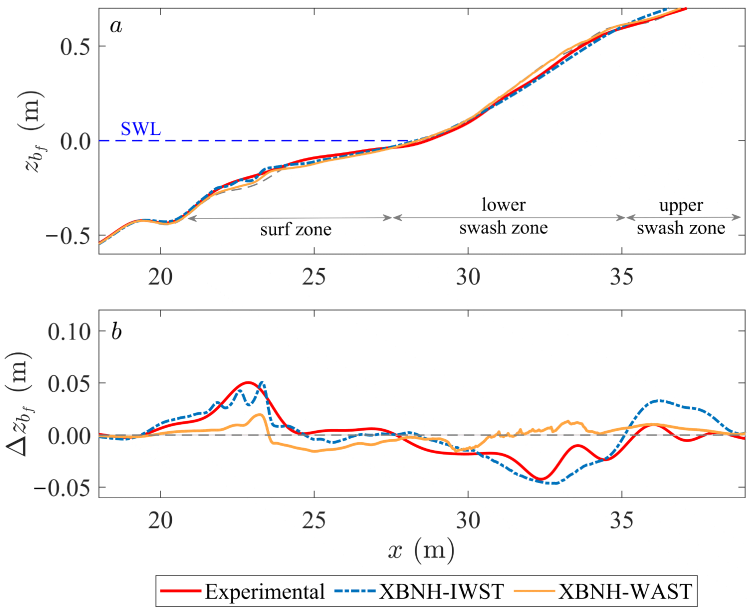

Figure 5.25: *a*: z_{b_f}; *b*: Δz_{b_f} after 3 waves; reference line: grey-dashed line

Table 5.16: nRMSE and RMSTE for Δz_{b_f} after 3 waves; comparison between XBNH-IWST and XBNH-WAST

	XBNH-IWST	XBNH-WAST
nRMSE	0.0218	0.0338
RMSTE	0.0862	0.5512

Fig. 5.26 shows the time series of u (Fig. 5.26a), C (Fig. 5.26b) and q_{sed} (Fig. 5.26c), with the corresponding nRMSE and ρ_{mr} in Table 5.17. The accuracy of the modelled C is higher for XBNH-WAST compared to XBNH-IWST. However, C predicted with XBNH-WAST drops to nearly zero values close to flow reversal unlike the experiments.

Table 5.17: nRMSE and ρ_{mr} for u and C at ADV8 and OBS3-4, respectively

		XBNH-WAST		XBNH-IWST	
		nRMSE	ρ_{mr}	nRMSE	ρ_{mr}
ADV8	u	0.7623	0.7128	0.7593	0.7163
OBS3-4	C	1.1436	0.1395	5.8174	0.5303

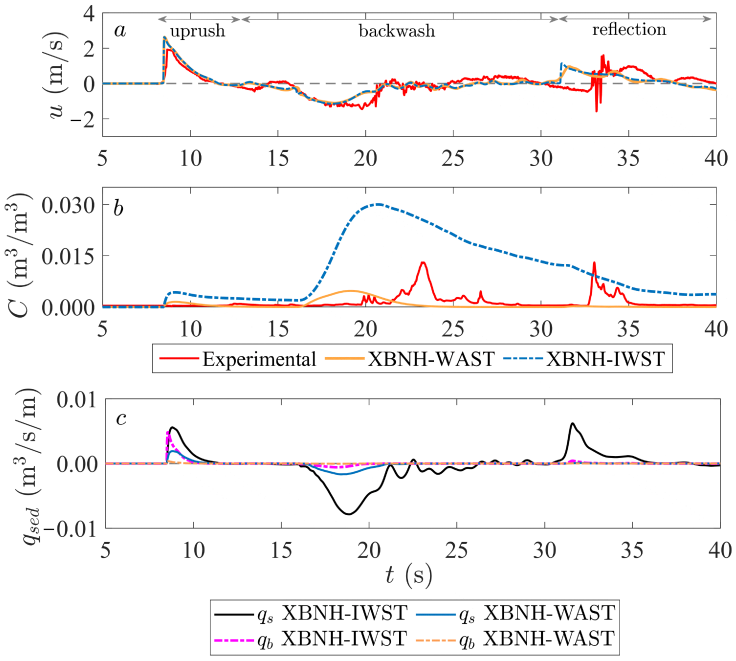

Figure 5.26: Time series of flow and sediment transport variables at $x = 23$ m; a: u; b: C; c: q_s and q_b; reference line: grey-dashed line

5.5 Numerical modelling of plunging breaking waves over a barred beach

In this section the performance of XBNH-IWST is tested with the Van der Zanden et al. (2016) experiments conducted within the and Transport under Irregular and Breaking Wave Conditions (SINBAD) project sponsored jointly by the EPSRC in the UK and by STW in the Netherlands. The experiments focused on the effects of wave breaking-induced TKE, including the near-bed TKE, on suspended sediment transport over a barred sandy beach. Therefore, the modelling of wave breaking-generated turbulence by XBNH-IWST and its morphodynamics response in the surf zone were assessed, and results are here illustrated.

5.5.1 Experimental set-up

The laboratory experiments of Van der Zanden et al. (2016) involved regular plunging breaker waves with $T = 4$ s and $H = 0.85$ m at the initial offshore $d = 2.55$ m over an erodible barred beach made of sand ($D_{50} = 0.24$ mm, $D_{10} = 0.15$ mm, $D_{90} = 0.37$ mm and $w_s = 0.034$ m/s). Waves were generated using the first-order wave theory.

Fig. 5.27 shows the experimental domain with the installed instruments considered for comparison with XBNH-IWST. The initial bed profile is a barred beach, which is the result of previous runs conducted starting with an horizontal flat bed. The trough of the bar is followed by a mildly 1:95 sloping bed ($57.5 \leq x \leq 68$ m). Shoreward of the test section ($x > 68$ m), the mobile bed profile was followed by a non-erodible 1:7.5 sloping structure made of slabbed concrete in order to reduce wave reflection and promote wave energy dissipation.

The water surface elevation was measured with Pressure Transducers (PT) and resistive WG; the flow velocity was measured with ADV sensors at three outer flow elevations (i.e., higher than 10 cm above the bed) and near the bed (i.e., below 10 cm above the bed) with Acoustic Concentration and Velocity Profilers (ACVP). Measurements of time-varying near-bed sediment concentrations were obtained with the ACVP sensors. The ADV and ACVP sensors were installed on a mobile measuring frame. Measurements of suspended sediment concentration obtained with OBS sensors were not reliable due to the presence of air bubbles at most locations (see also Cáceres et al., 2020). Time-varying k and $k_{b_{tot}}$ were obtained from the velocity measurements performed with the

ADV and ACVP sensors, respectively.

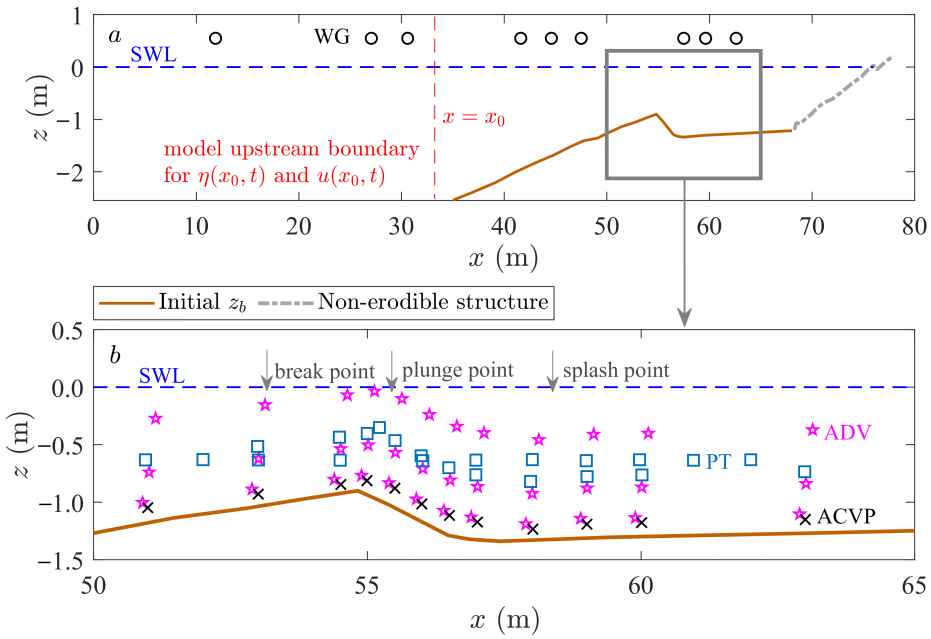

Figure 5.27: Van der Zanden et al. (2016) experimental domain with instrumentation installed and considered for comparison with this study; *a*: whole domain; *b*: zoom-in of the test section used for the instruments installed on the mobile frame

The experiments consisted of 6 runs of 15 mins each. The bed profile was measured prior to the first run and after every 30 minutes (i.e., at $t = 0$, 30, 60 and 90 min). The experiments were repeated 12 times, each time the mobile frame was moved to a different cross-shore location. A standing wave was induced by the flume seiching but it was removed from all the post-processed data provided for the present study. The reader is referred to Van der Zanden et al. (2016) for a detailed description of the experimental procedures.

5.5.2 Model set-up

XBNH-IWST used the same physical parameters as in the previous test cases described in Chapter 5 (see also Table 5.2 for the sediment transport modelling), except for m_{cr} in the KW92-A09 turbulence model and μ in the S13 viscosity model for the HFA; $m_{cr} = 0.4$ and $\mu = 0.5$ were chosen because they allow to better represent the observed turbulence and hydrodynamics compared to the values used in the previous test cases. Table 5.18 summarises the values of the parameters for the TKE model and the ν_h model

for the HFA, respectively. As for the previous cases, $\alpha_{br} = 0.4$ was used. $\Delta x = 0.1$ m and $n = 0.02$ m$^{1/3}$s^{-1} for the computation of c_f were chosen. Time series of η and u were obtained with the one-layer version of the SWASH model and they were provided at the upstream boundary located at $x = x_0 = 33$ m (with a time resolution of $1{\times}10^{-3}$ s). The SWASH model was used to obtain the time series of η and u at x_0 by using the experimental time series of η at $x = 31.6$ m and considering a flat bad with a sponge layer extending from the downstream boundary for a total length of three times the offshore wave length, L. Note that the time series of η at $x = 31.6$ m were obtained by using the experimental post-processed time-varying, phase-averaged η at $x = 31.6$ m. The performance and robustness of XBNH-IWST was further assessed by carrying out simulations for different boundary conditions and bed configurations (see also Appendix G).

Table 5.18: Main parameters in the TKE model and the horizontal viscosity models

Parameters		Values
m_{cr}	=	0.4
γ_d	=	0.4
γ_k	=	1
μ	=	0.5

5.5.3 XBNH-IWST modelling of the Van der Zanden et al. (2016) experiments

Comparison with the experiments is shown for the measurements obtained during the first segment i.e., for the first 15 minutes of the bed profile development, since as indicated in Van der Zanden et al. (2016), the later stages of the bar development showed qualitatively similar behaviour in terms of hydrodynamic processes.

η_{max} and $\bar{u}$ across the domain are shown in Fig. 5.28a and b, respectively, with the corresponding nRMSE in Table 5.19. Similarly to the Ting and Kirby (1994) case study (see also Section 4.3.6), XBNH-IWST anticipates the breaking point, which was at approximately $x = 53$ m in the experiments (see also Fig. 5.27). The model is able to simulate the wave energy dissipation after breaking in terms of η_{max}. However, XBNH-IWST is not able to obtain a gradient of the same magnitude observed in the distribution

of the experimental $\bar{u}$. The nRMSE for η_{max} is lower by 76%, compared to that for $\bar{u}$. The experimental $\bar{u}$ decreases from $x = 55$ m; it reaches its maximum negative value at $x = 57$ m, and remains negative in the inner surf zone, whereas the modelled $\bar{u}$ increases shoreward of the bar crest (i.e., over the nearly flat shelf extending for $57 \leq x \leq 68$ m). In fact, the distribution of the modelled $\bar{u}$ is similar to that obtained using the shallow water theory. Similar results were obtained for the other boundary conditions and bed configurations considered (see Appendix G).

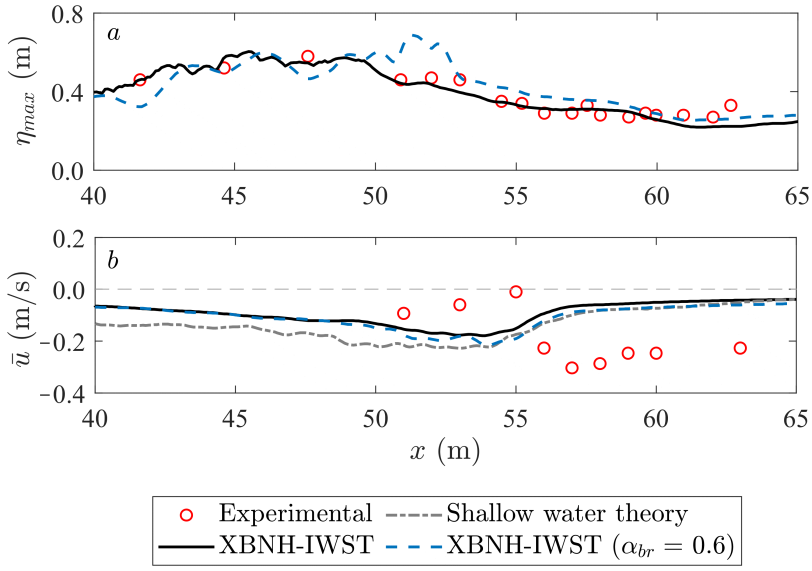

Figure 5.28: Distribution of flow variables across the x-domain; a: η_{max}; b: $\bar{u}$; grey-dashed line: reference line

Table 5.19: nRMSE for η_{max}, $\bar{u}$, $\bar{k}$, $\bar{k}_{b_{tot}}$ and $\bar{C}_{nb}$ across the x-domain

	nRMSE
η_{max}	0.4143
$\bar{u}$	1.7186
$\bar{k}$	20.7799
$\bar{k}_{b_{tot}}$	2.6539
$\bar{C}_{nb}$	27.7610

Simulations were also carried out by increasing α_{br}. As shown in Fig. 5.28, for $\alpha_{br} = 0.6$ the modelled breaking point is shifted shoreward and it is closer to the observed one than for $\alpha_{br} = 0.4$. However, η_{max} is overestimated for $51 \leq x \leq 59$ m. The nRMSE

for η_{max} with $\alpha_{br} = 0.6$ is equal to 0.8679 and it is higher by 52% than the nRMSE for $\alpha_{br} = 0.4$. Furthermore, the increase of α_{br} does not improve the prediction of $\bar{u}$, both qualitatively and quantitatively. The nRMSE for $\bar{u}$ with $\alpha_{br} = 0.6$ is equal to 1.6537, therefore, comparable to that for $\alpha_{br} = 0.4$ (see Table 5.19).

Fig. 5.29 illustrates the time-varying phase-averaged η and u at different x-coordinates. Note that the experimental u was obtained by computing the average of the time-varying phase-averaged velocities measured at different $z-$locations (see also Fig. 5.27). The corresponding nRMSE and ρ_{mr} are shown in Table 5.20. Note also that for u the collected signals at $x = 55$ m were affected by the wave plunge and splash (see also Fig. 5.27).

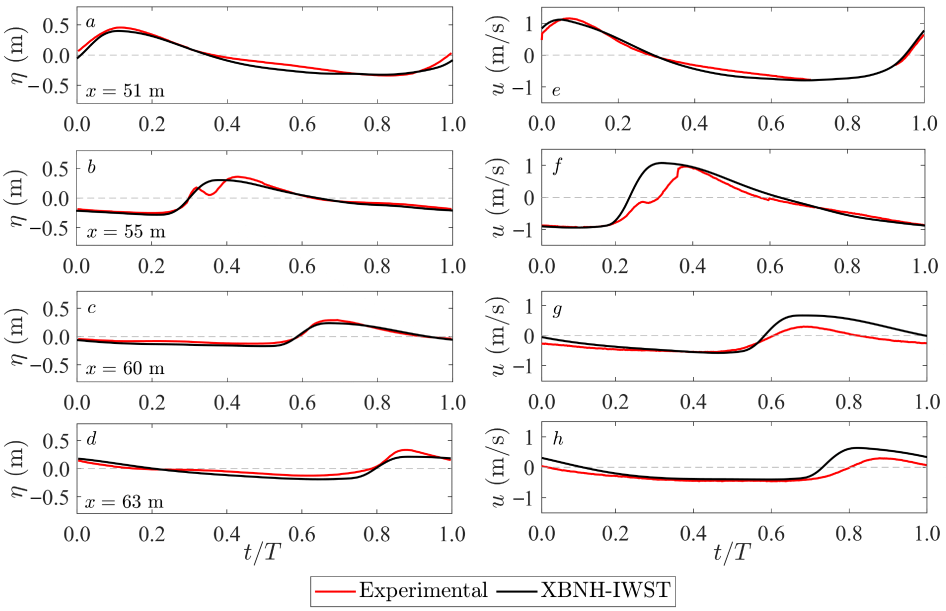

Figure 5.29: Time-varying phase-averaged η and u at different x-coordinates; a and e: $x = 51$ m; b and f: $x = 55$ m; c and g: $x = 60$ m; d and h: $x = 63$ m; grey-dashed line: reference line

Table 5.20: nRMSE and ρ_{mr} for the time-varying phase-averaged η, u, $k^{0.5}$ and $k_{b_{tot}}^{0.5}$

	η		u		$k^{0.5}$		$k_{b_{tot}}^{0.5}$	
	nRMSE	ρ_{mr}	nRMSE	ρ_{mr}	nRMSE	ρ_{mr}	nRMSE	ρ_{mr}
$x = 51$ m	0.2876	0.9273	0.1604	0.9888	33.6183	0.0847	4.0676	0.5081
$x = 55$ m	0.2997	0.9607	0.4916	0.9550	14.1135	0.6626	1.4247	0.7695
$x = 60$ m	0.2863	0.9839	1.0293	0.9765	37.6116	−0.2869	2.3485	0.3910
$x = 63$ m	0.4831	0.9348	0.9390	0.9609	39.1585	−0.4397	0.6898	0.7746

Results confirm the better performance of XBNH-IWST in terms of η than u, especially in the inner surf zone until $x = 60$ m, whereas a mismatch between model predictions and experiments is found for both η and u at $x = 63$ m. In particular, ρ_{mr} for η and u is close to 1 at all the x-coordinates considered. Instead, for η the nRMSE increases at $x = 63$ m, and for u the nRMSE increases at $x = 60$, 63 m compared to the other x-coordinates. The model is able to simulate the shape of η and u over the wave-cycle, however, it is not able to properly describe the dissipation in terms of u for the locations shoreward of the bar crest (i.e., $x > 55$ m). Fig. 5.30a and b shows the distribution of $\bar{k}$ and $\bar{k}_{b_{tot}}$ across the x-domain.

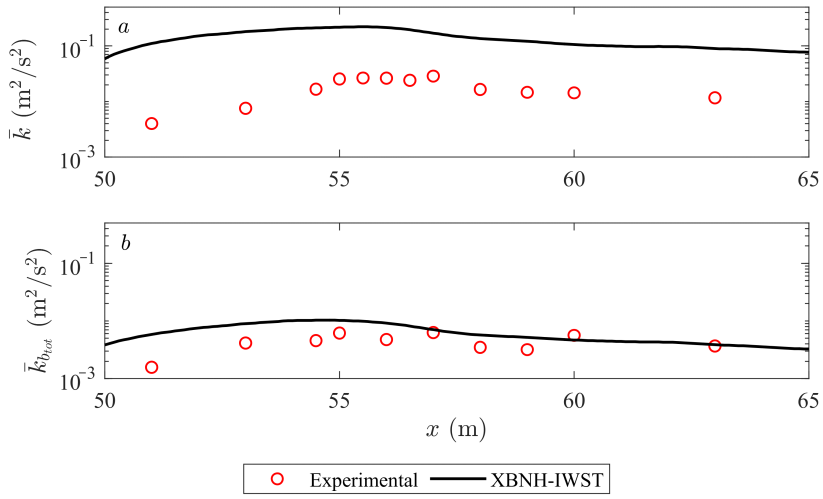

Figure 5.30: Distribution of turbulence across the x-domain; a: $\bar{k}$; b: $\bar{k}_{b_{tot}}$

XBNH-IWST overestimates both $\bar{k}$ and $\bar{k}_{b_{tot}}$, and in turn, predicts a lower gradient for both $\bar{k}$ and $\bar{k}_{b_{tot}}$ at the x-coordinates across the seaward slope of the bar (i.e., for $x < 55$ m). This is likely due to the breaking point predicted at a location seaward of the observed one. The present model is able to capture the decrease of $\bar{k}$ and $\bar{k}_{b_{tot}}$ in the inner-surf zone. However, XBNH-IWST overestimates $\bar{k}$ by an order of magnitude in the breaking zone and throughout the inner surf zone, while the order of magnitude of $\bar{k}_{b_{tot}}$ is well captured by the model. This is important for the XBNH-IWST performance, because $k_{b_{tot}}$ directly affects the bed shear stress modelling (i.e., the hydrodynamics and the sediment transport modelling with XBNH-IWST). Results illustrated in Fig. 5.30a and b are in turn, confirmed by the values of nRMSE in Table 5.19. The nRMSE for $\bar{k}_{b_{tot}}$ is an order of magnitude lower than that for $\bar{k}$. Note that the nRMSE for $\bar{k}$ is

higher than those for the other variables not only due the lower accuracy of the model in predicting k compared to η_{max} and $\bar{u}$, but also to the low standard deviation of $\bar{k}$ (see also Eq. (40)).

The intra-wave phase-averaged $k^{0.5}$ and $k^{0.5}_{b_{tot}}$ at different x-coordinates are shown in Figs. 5.31 and 5.32, respectively. As previously mentioned for u, measurements for $55 \leq x \leq 57$ m were affected by the wave plunge and splash (see also Fig. 5.27).

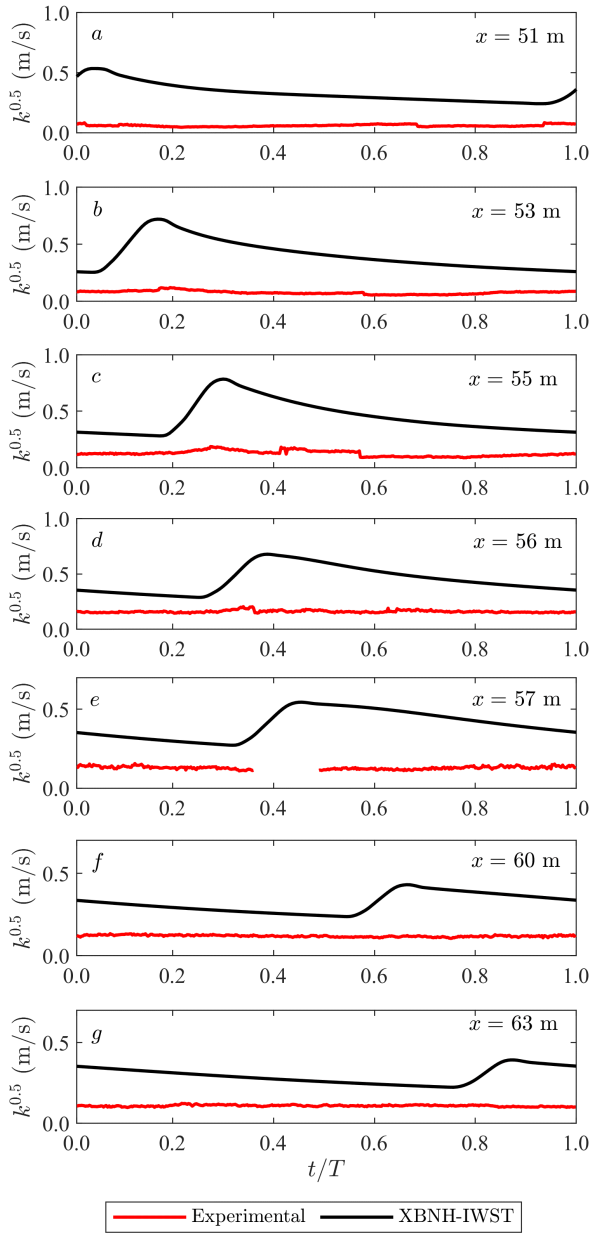

Figure 5.31: Time-varying phase-averaged $k^{0.5}$ at different x-coordinates; a: $x = 51$ m; b: $x = 53$ m; c: $x = 55$ m; d: $x = 56$ m; e: $x = 57$ m; f: $x = 60$ m; g: $x = 63$ m; grey-dashed line: reference line

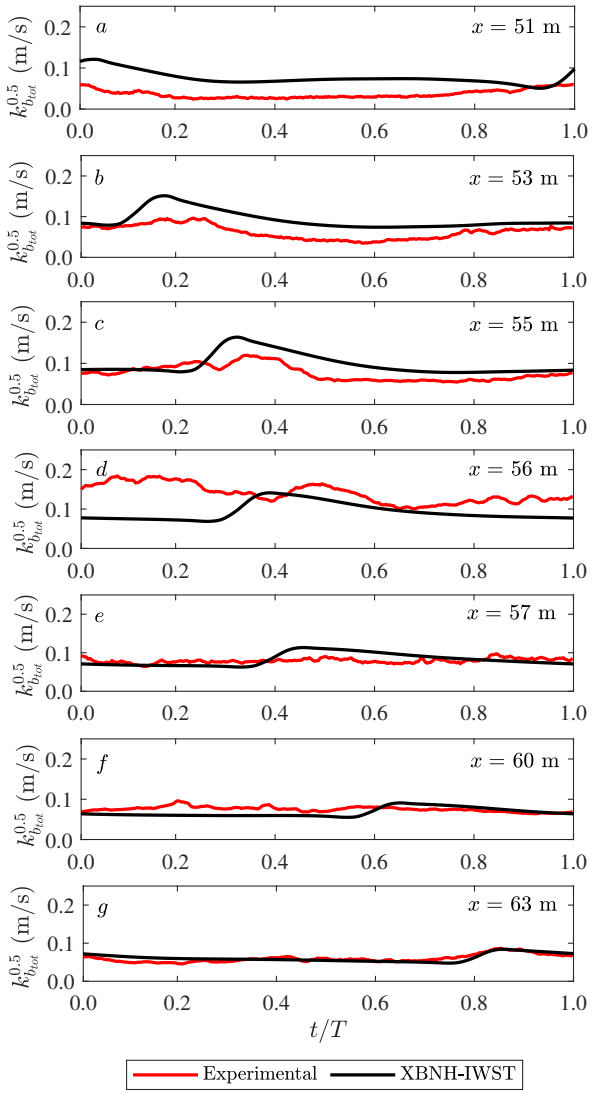

Figure 5.32: Time-varying phase-averaged $k_{b_{tot}}^{0.5}$ at different x-coordinates; *a*: $x = 51$ m; *b*: $x = 53$ m; *c*: $x = 55$ m; *d*: $x = 56$ m; *e*: $x = 57$ m; *f*: $x = 60$ m; *g*: $x = 63$ m; grey-dashed line: reference line

The nRMSE and ρ_{mr} for selected x-coordinates are shown in Table 5.20. XBNH-IWST overestimates $k^{0.5}$, whereas the model is able to capture the order of magnitude of $k_{b_{tot}}^{0.5}$ at the intra-wave resolution. Similarly to the time-averaged quantities, the nRMSE for $k_{b_{tot}}^{0.5}$ is one order of magnitude higher than that for $k_{b_{tot}}^{0.5}$. Additionally, ρ_{mr} for $k_{b_{tot}}^{0.5}$ is always higher than 0.5, except for $x = 60$ m. XBNH-IWST is able to capture the phase of $k_{b_{tot}}^{0.5}$ both in the breaking region (i.e., at $x = 55$ m) and where bed-generated turbulence was observed to be dominant (i.e., for $x \leq 53$ m and $x = 63$ m; see also Van der Zanden et al., 2016).

Since measurements of C_z are not available at locations above the near-bed re-

gion, the modelled and experimental C cannot be compared. A comparison between the distributions of the computed and experimental time-averaged near-bed sediment concentration, $\bar{C}_{nb}$, is shown in Fig. 5.33*a*. As for $\bar{u}$, $\bar{k}$ and $\bar{k}_{b_{tot}}$, $\bar{C}_{nb}$ is computed by averaging C_{nb} over the first segment of 15 minutes.

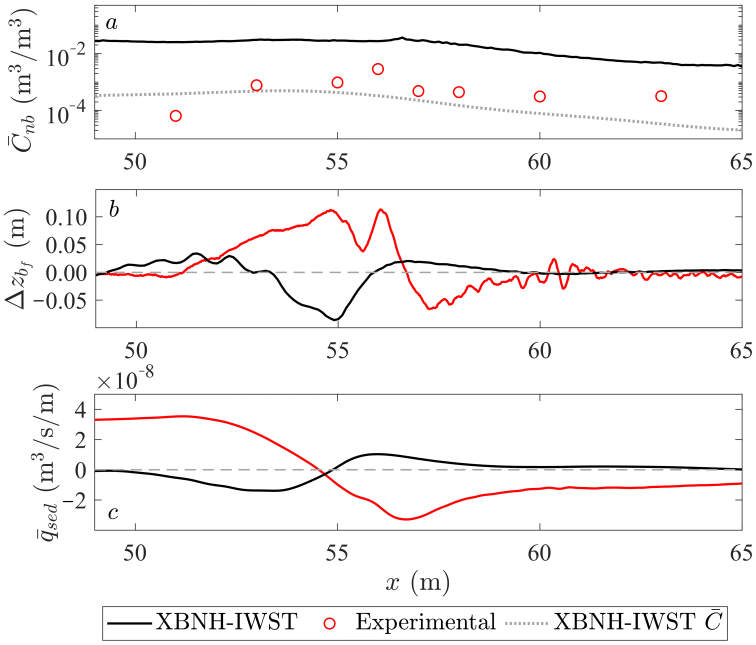

Figure 5.33: *a*: $\bar{C}_{nb}$ for 15 minutes of simulation; *b*: Δz_{b_f} after 30 minutes; *c*: $\bar{q}_{sed}$ for 30 minutes of simulation; grey-dashed line: reference line

Results show that the computed $\bar{C}_{nb}$ is larger than the experimental one, especially seaward of the observed breaking point (see also Fig. 5.27). The experimental $\bar{C}_{nb}$ decreases with a more pronounced slope in the offshore direction starting from the peak of $\bar{C}_{nb}$ at $x = 56$ m. This distribution is similar to that of the experimental $\bar{k}_{b_{tot}}$ (see Fig. 5.30*b*). For $x < 56$ m the experimental $\bar{C}_{nb}$ rapidly decreases unlike the computed one. XBNH-IWST is able to obtain the negative gradient of $\bar{C}_{nb}$ in the inner-surf zone (i.e., for $x > 56$ m), but $\bar{C}_{nb}$ is overestimated. The nRMSE for $\bar{C}_{nb}$ is of the same order of magnitude of that for $\bar{k}$ (see Table 5.19). Fig. 5.33*a* also illustrates the predicted $\bar{C}$. As expected, $\bar{C}$ is lower than $\bar{C}_{nb}$, and decreases shoreward of the bar crest.

The final bed changes after 30 minutes, i.e., Δz_{b_f} ($z_{b_f} = z_b(x, t_f)$, with $t_f = 30$ min) and $\bar{q}_{sed}$ computed over 30 minutes of simulation are shown in Fig. 5.33*b* and *c*, respectively. Results indicate that Δz_{b_f} predicted with XBNH-IWST do not agree with

the observed Δz_{b_f}; the RMSTE is 0.3328 m^2. The experimental Δz_{b_f} show a growth and an onshore migration of the bar crest and an increasing depth of the bar trough. Instead, XBNH-IWST predicts a reduction of both the height of the bar and depth of the bar trough. This is reflected by $\bar{q}_{sed}$ in Fig. 5.33*c*. The experimental $\bar{q}_{sed}$ is onshore-directed for $x < 54.5$ m (i.e., until the bar crest) and offshore-directed for $x > 54.5$ m, while the modelled $\bar{q}_{sed}$ shows the opposite sign, compared to the experimental one.

6 Discussion

This chapter presents a discussion of the results obtained in this study. First, the modelling improvements achieved by using the wave-resolving sediment transport formulations within XBNH-IWST with respect to XBNH-WAST are discussed. Then, a discussion focused on the XBNH-IWST modelling of the wave breaking-generated TKE and the additional horizontal viscosity for the HFA is presented. The performance of XBNH-IWST in predicting the process of breaker bars development is finally discussed.

6.1 XBNH-IWST modelling improvements with respect to XBNH-WAST

The proposed wave-resolving sediment transport formulations within XBNH-IWST (i.e., the modified Pritchard and Hogg, 2003 equation and the Meyer-Peter and Müller, 1948 relationship), allow to obtain a more accurate morphodynamics response compared to the available XBNH-WAST model (see Sections 5.3.5 and 5.4.4). For both the Alsina et al. (2016) and Young et al. (2010) test cases, the performance of the Meyer-Peter and Müller (1948) formulation is consistent with the results of previous studies (see e.g., Xiao et al., 2010, Postacchini et al., 2012). As shown in Mancini et al. (2021), where the wave breaking-generated TKE and the additional viscosity modelling for the HFA were not taken into account, and then further analysed in this thesis, XBNH-IWST shows an improvement in predicting the intra-wave suspended sediment concentration and bed changes, compared to XBNH-WAST. For both wave trains and isolated waves over sloped beaches (i.e., the Alsina et al., 2016 and Young et al., 2010 test cases), the model herein developed is able to simulate the order of magnitude of the sediment suspension (i.e., C) near flow reversal. Instead, consistently with Ruffini et al. (2020), C predicted by XBNH-WAST is nearly zero in the same aforementioned conditions, unlike the experiments (see Figs. 5.18 and 5.26). Differences in the predicted C lead, in turn, to differences in the modelled Δz_{b_f} and $\bar{q}_{sed}$. Results shown in Chapter 5 indicate that XBNH-IWST is able to simulate the deposition in the upper swash zone and the erosion in the lower swash region for both wave trains where swash-swash interactions are clearly present and isolated waves. Instead, XBNH-WAST significantly underestimates the deposition in the upper swash zone for the Alsina et al. (2016) case (see Fig.

5.19), and does not properly simulate the observed deposition and erosion patterns in terms of bed changes for the Young et al. (2010) case (see Fig. 5.25). Moreover, results obtained with XBNH-IWST for the Young et al. (2010) case study are comparable to those of Kranenborg et al. (2020) that used the depth-resolving RANS model presented in Jacobsen et al. (2014) and Jacobsen and Fredsoe (2014), based on OpenFOAM®, to simulate the same laboratory experiments. Unlike XBNH-IWST, the modelled bed changes obtained by Kranenborg et al. (2020) are slightly shifted in the onshore direction with respect to the observed ones.

Regarding the location of the predicted deposition in the upper swash zone for the Alsina et al. (2016) case (see Fig. 5.7), results obtained in this study are consistent with those presented in Van Rooijen et al. (2012). The slightly offshore-shifted deposition modelled with XBNH-IWST, compared to the observed one, is likely due to the underestimation of the wave run-up by XBNH for more complex wave conditions than isolated waves, and which therefore, could not be overcome by calibrating the bed friction coefficient.

6.2 XBNH-IWST modelling of TKE and additional horizontal viscosity for the HFA

The contribution of turbulence effects in the hydrodynamics and sediment transport modelling is allowed by the the inclusion of the wave breaking-generated TKE model (i.e., k), together with the near-bed TKE model (i.e., k_b) in XBNH-IWST.

XBNH-IWST well captures the phase and order of magnitude of k in the inner-surf zone for both the spilling and plunging breakers conditions for the Ting and Kirby (1994) case, whereas the model overestimates k for the plunging breakers simulated in the Van der Zanden et al. (2016) experiments. The experimental k for the Van der Zanden et al. (2016) case is smaller than k for the Ting and Kirby (1994) experiments (see Figs. 4.16 and 5.31) and does not change significantly over the wave-cycle. As indicated in Van der Zanden et al. (2016), this difference is likely related to the presence of the bar in their study. Moreover, unlike the previous study of Reniers et al. (2013), leading to the turbulence model referred in this thesis to as R13, XBNH-IWST can capture the tail of the intra-wave $k_{b_{tot}}$ observed after the wave-crest and over the wave-trough for the Van der Zanden et al. (2016) experiments (see Fig. 5.32).

Results shown in Section 5.5 indicate that, for the Van der Zanden et al. (2016) case, XBNH-IWST better models $k_{b_{tot}}$ than k (values of the nRMSE for $k_{b_{tot}}$ are an order of magnitude lower than those for k and $\rho_{mr} > 0.5$ for $k_{b_{tot}}$ for most of the x-coordinates considered, unlike for k; see Tables 5.19 and 5.20). For $51 \leq x \leq 55$ m the gradient of both the modelled $\bar{k}$ and $\bar{k}_{b_{tot}}$ is lower than that of the experimental $\bar{k}$ and $\bar{k}_{b_{tot}}$ (see Fig. 5.30). This mismatch is thought to be due to the predicted wave breaking point by XBNH-IWST being offshore with respect to the observed one. The overall model overestimation of $\bar{k}$ is found to be similar to the results obtained in other studies, e.g., the Schnitzler (2015)'s MSc thesis where the Delft3D model (Lesser et al., 2004) was used. Therefore, this mismatch is thought to depend on either the accuracy of measurements or the XBNH-IWST performance. As shown in Section 4.3.4, the order of magnitude of k could be decreased/increased by varying γ_d in the TKE balance equation (see also Eq. (29)). However, a decrease of k would lead to an underestimation of k_b, which is used in the computation of the bed shear stress.

For the Alsina et al. (2016) case the inclusion of the wave breaking-induced TKE effects and the additional horizontal viscosity for the HFA qualitatively improves the prediction of $\bar{q}_{sed}$ and the accuracy in predicting Δz_{b_f} by 10% in terms of RMSTE for both the broad- and narrow-banded wave conditions (see Figs. 5.7, 5.8 and Table 5.8). However, the simulation of the breaker bar development, which is further discussed in the following, is not accurate yet.

Differences between the morphodynamic predictions obtained by including the effects of wave breaking-induced TKE and without the TKE modelling are difficult to discern for the Young et al. (2010) case (see Section 5.4.3). Results for this case are likely explained by the dominance of the bed-induced turbulence over the breaking-generated one for the most part of the wave-cycle except for the peak of turbulence at the wave-crest (see Fig. 5.24).

According to Smit et al. (2013), for the Alsina et al. (2016) test case the additional horizontal viscosity for the HFA allows to better describe the dissipation after wave breaking by preventing the formation of higher frequencies noise generated by the enforced hydrostatic pressure, especially in terms of time series of η and u at AWG7 (i.e., in the swash zone; see Tables 5.7 and 5.9).

6.3 XBNH-IWST modelling of breaker bars development

The performance of XBNH-IWST in modelling the process of breaker bars development depends greatly on the accuracy of the model in predicting u, which conversely is one of the more important variables in determining C.

A note of caution should be provided regarding the parameters of the Pritchard and Hogg (2003) transport equation. The sensitivity analysis presented in Section 5.3.3 showed that m_e is the parameter that mostly influences the prediction of Δz_{b_f} and C (see Table 5.4 and Fig. 5.2). However, because no field data are available to provide its estimates, the only comparison with the findings of the present study are previous numerical studies, such that Zhu and Dodd (2015). The value of m_e that showed best modelling in this study is an order of magnitude larger than that used by Zhu and Dodd (2015) for a single solitary wave in well-mixed conditions (i.e., $K_C = 1$). Moreover, the choice of the values of m_e selected in Section 5.3.3 was supported by the results obtained from the back computation of the parameter m_e using the CoSSedM experimental data (see Appendix D) where $K_C \geq 1$ was considered (i.e., K_C is computed by XBNH-IWST). The optimal m_e found was used in combination with $R = 1.5$ (R being an arbitrary numerical parameter), λ equal to the considered wave height at the upstream boundary. To simplify the choice of the values corresponding to the parameters considered in the Pritchard and Hogg (2003) expression, $\tau_{b,cr}$ was set equal to zero. This choice was justified following Zhu and Dodd (2015) who pointed out that the effect of a threshold for suspended load is not significant for sandy beaches morphodynamics. λ is an arbitrary length scale, which in turn, affects the other scale parameter, τ_{ref}. Therefore, representative values of λ were selected for the model calibration (see Section 5.3.3). τ_{ref} was computed similarly to Zhu and Dodd (2015) for all the simulations carried out. As shown in Section 5.3.3, although the proposed set of parameters allows to obtain a lower RMSTE and a better prediction of the erosion and deposition patterns than the other combinations tested (see Table 5.6), the prediction of C, and in turn, of Δz_{b_f} with XBNH-IWST are still inaccurate. Moreover, results obtained for both the Alsina et al. (2016) and Young et al. (2010) test cases indicate that the new parametrisation proposed in this study, to account for the effects of k_b in the sediment transport modelling, does not improve the accuracy of XBNH-IWST in predicting C (see Tables 5.9 and 5.14) and the description of the breaker bar development (see Figs.

5.7 and 5.8). The numerical modelling of the uprush and backwash dynamics should be discussed separately, due to the different nature of the two flow stages. The mismatch between the modelled and experimental u is likely to influence mainly the modelling of C at the uprush stages (see e.g., Fig. 5.10 at $t/T_r \sim 0.1$). Instead, the high peaks of the predicted C corresponding to the backwash events within the wave groups, diverging from the experimental C (see Figs. 5.9 and 5.10), indicate that XBNH-IWST seems not to be able to properly model the saturation of the thin layer of the backwash flow.

Results shown in this thesis point out that XBNH-IWST performs better when the initial bed profile has already evolved with respect to simulations carried out for uniform sloping beaches. These results are favourable because in field cases uniform slopes are rear occurrences. For BE4_2 of the Alsina et al. (2016) case, results show that by using the measured z_{b_f} after SEG1 as the initial z_b to simulate SEG2 (i.e., by imposing the bar at the start of the segment) the overall morphodynamic response of XBNH-IWST improves compared to the simulations carried out using the modelled z_{b_f} after SEG1, both qualitatively (see Fig. 5.16) and quantitatively (by 11% in terms of RMSTE). Despite measurements of u in the surf zone being not available, the modelled $\bar{u}$ in this region (i.e., for $62 \leq x \leq 68$ m) are qualitatively different for the two initial bed configurations considered. XBNH-IWST can capture the distribution of $\bar{u}$ in the swash zone for the two alternative initial bed configurations used. When the bar is imposed, XBNH-IWST can obtain the magnitude of $\bar{q}_{sed}$ as in the experiments. However, the model is still not able to properly simulate the change of sign of $\bar{q}_{sed}$ at $x \sim 62$ m (i.e., seaward of the bar crest). Moreover, the intra-wave C predicted with XBNH-IWST, when the bar is imposed, is qualitatively similar to that obtained using the modelled z_{b_f} after SEG1 (see Fig. 5.17). Also, for both the two alternative initial bed configurations used XBNH-IWST overestimates C at the first uprush within the wave group (i.e., at $t/T_r \sim 0.1$) and during the backwash events.

For the Young et al. (2010) experiments, where the initial z_b was the results of previous runs on the nominal 1:15 sloped bed, such that it can be considered as a near-equilibrium profile beach state, Δz_{b_f} predicted with XBNH-IWST show lower nRMSE and RMSTE than for the Alsina et al. (2016) case by 60% and by 70%, respectively.

A different performance was obtained for the Van der Zanden et al. (2016) test case, where the initial z_b is a barred beach. Unlike the Alsina et al. (2016) experiments, which

are characterised by an initial monotonic sloping beach, the Van der Zanden et al. (2016) initial z_b presents a nearly flat shelf shoreward of the bar trough, which allows a long bore-like propagation. XBNH-IWST can simulate the dissipation shoreward of the wave breaking point in terms of η_{max}, however, the model cannot capture the experimental gradient magnitude of $\bar{u}$ across the x-domain (see Fig. 5.28). In particular, XBNH-IWST is not able to describe the dissipation in terms of u throughout the inner-surf zone (i.e., across the shelf). The modelled $\bar{u}$ is found to be qualitatively similar to that obtained using the shallow water theory. According to Van Der Zanden et al. (2017a), an accurate modelling of the near-bed sediment concentration greatly relies on the accuracy of the modelled near-bed TKE. The Pearson's correlation coefficient (computed as in Eq. (4.1)) between the modelled $\bar{k}_{b_{tot}}$ and $\bar{C}_{nb}$ is equal to 0.5491, which is 13% lower than the value obtained by Van Der Zanden et al. (2017c) for the experimental $\bar{k}_{b_{tot}}$ and $\bar{C}_{nb}$ for the Van der Zanden et al. (2016) experiments. Considering the nature of the sediment transport advection-diffusion equation used in this study, the accurate prediction of C, and in turn, of Δz_{b_f}, relies on the model performance in predicting u, and in turn, $k_{b_{tot}}$. Consequently, results for the Van der Zanden et al. (2016) case show poor morphodynamics predictions in terms of Δz_{b_f}, and therefore, of $\bar{q}_{sed}$ (see Fig. 5.33*b* and *c*). Both the experimental and predicted $\bar{q}_{sed}$ change sign at approximately $x = 54.5$ m, which is the x-coordinate where the gradient of both the experimental and modelled $\bar{u}$ (see also Fig. 5.28*b*) is found to change, but with different slopes.

Following the results discussed above, the inaccuracy of the sediment transport model proposed in this study in addition to the lack of modelling processes that have a vertical structure (i.e., vertical structure the flow and suspended sediment concentration) are thought to be the cause of the surf zone morphodynamics mismatch between XBNH-IWST and the experiments for the Alsina et al. (2016) and Van der Zanden et al. (2016) case studies.

7 Conclusions

This thesis aims at improving the numerical modelling of the intra-wave sediment transport on sandy beaches, and therefore, the simulation of the exchange of sediments between the swash and surf zones, which feeds the development of breaker bars under storms.

A wave-resolving, non-hydrostatic depth-averaged model based on the open-source Non-Hydrostatic XBeach (XBNH) framework was investigated for the use in coastal engineering practice. It was found in the literature that the morphodynamics response of XBNH lacked a validation in the context of sandy beaches. Indeed, the available sediment transport formulations within XBNH were originally developed and validated to solve the Wave-Averaged Sediment Transport (XBNH-WAST). Therefore, in this study the Pritchard and Hogg (2003) transport equation for the depth-averaged suspended sediment concentration was newly implemented in XBNH to solve the Intra-Wave Sediment Transport (XBNH-IWST). The aforementioned expression includes both advection and diffusion terms. XBNH-IWST uses the Meyer-Peter and Müller (1948) formula to compute the bed load transport rate. Verification (Chapter 4) against Zhu and Dodd (2015) indicates that the Pritchard and Hogg (2003) transport equation performs qualitatively and quantitatively well when compared with a high-accuracy numerical solution of Non-Linear Shallow Water Equations (NLSWE) (the normalised Root-Mean-Square Error, nRMSE, is equal to 0.0085 for the bed changes and the Root-Mean-Square Transport Error, RMSTE, is equal to 0.003 m^2; the nRMSE for the depth-averaged suspended sediment concentration is on average equal to 0.2671). Therefore, this modelling approach is suitable for solving the intra-swash sediment transport in the context of wave-resolving models.

XBNH-IWST also includes a newly implemented wave breaking-generated turbulence model based on a depth-averaged Turbulent Kinetic Energy (TKE) balance, together with a near-bed TKE model similar to that proposed by Roelvink and Stive (1989). Two alternative models were considered to solve the production and dissipation of TKE in the balance equation: the turbulence model, referred in this thesis to as R13, is based on the roller surface model for the wave energy dissipation used in Reniers et al. (2013), while the turbulence model, referred in this study to as KW92-A09, is based on

the time-dependent wave energy model proposed by Kobayashi and Wurjanto (1992) and the study of Alsina et al. (2009). The effects of the modelled turbulence are taken into account both in the hydrodynamics and sediment transport modelling through the bed shear stress. For the modelling of wave breaking, similarly to Smit et al. (2013), an additional horizontal viscosity model for the Hydrostatic Front Approximation (HFA) was included in XBNH-IWST. Two alternative models were implemented to compute the horizontal viscosity when the enforced hydrostatic pressure is activated: the viscosity model, herein referred to as K42-P45, is based on the theories of Kolmogorov (1942) and Prandtl (1945), whereas the viscosity model, referred in this thesis to as S13, is based on the mixing length method used in Smit et al. (2013). The hydrodynamics response of XBNH-IWST, including the wave breaking-generated TKE and additional horizontal viscosity models for the HFA, was verified against the Ting and Kirby (1994) experiments (Chapter 4), which involved plunging and spilling breaking waves over a uniform sloped fixed bed. Results of the verification indicate that XBNH-IWST is able to describe the dissipation due to breaking for Ting and Kirby (1994). XBNH-IWST can obtain the shape and the order of magnitude of the intra-wave TKE for both the spilling and plunging breakers. The near-bed TKE modelling was tested with the Van der Zanden et al. (2016) experiments in Chapter 5.

XBNH-IWST was validated against two test cases (Chapter 5) involving wave trains where swash-swash interactions were present (i.e., the Alsina et al. (2016) experiments) and isolated waves (i.e., the Young et al. (2010) experiments), respectively, over monotonic sloped sandy beaches. A further case was selected for the testing of XBNH-IWST on the simulation of plunging breaking waves over a barred sandy beach (i.e., the Van der Zanden et al. (2016) experiments). In the latter simulations data-model comparison was carried out only for surf zone dynamics. A preliminary sensitivity analysis provided the best modelling set of parameters included in the Pritchard and Hogg (2003) equation and the performance of the resulting model was assessed with the aforementioned test cases.

Numerical simulations of the Alsina et al. (2016) and Young et al. (2010) laboratory experiments show that XBNH-IWST is able to simulate the order of magnitude of the intra-wave depth-averaged suspended sediment concentration close to flow reversal unlike XBNH-WAST. Consequently, XBNH-IWST improves the modelling of final bed

changes, especially in the swash zone, with respect to XBNH-WAST by 42% and 84% in terms of RMSTE, for the Alsina et al. (2016) and Young et al. (2010) cases, respectively.

7.1 Limitations and outlook on future research

This study shows that there are still limitations in the qualitative and quantitative representation of the sediment transport rate and consequently, of the morphological evolution of beaches by XBNH-IWST. In particular, for the Alsina et al. (2016) and Young et al. (2010) cases the prediction of time series of the depth-averaged suspended sediment concentration with XBNH-IWST is not accurate yet, especially at the backwash stage of the flow. The missing explicit representation of processes such as phasing effects of the velocity in the Bottom Boundary Layer (BBL) is certainly a factor that concurs to the inaccuracy of the proposed model in predicting the intra-wave suspended sediment concentration. Moreover, for both wave trains and isolated waves over monotonic beaches, XBNH-IWST performs better when the initial bed level is closer to the morphodynamic equilibrium (i.e., the bed has already evolved) than for an initial uniform sloped bed. These results are reassuring because in the field the latter configuration is of rear occurrence compared to the former one. On the other hand, results for the Van der Zanden et al. (2016) experiments, where the initial bed configuration is a barred beach with a nearly flat shelf extending shoreward of the bar trough, show that XBNH-IWST is not able to properly obtain the experimental spatial gradient of the flow velocity in the surf zone. The model is capable of predicting the dissipation due to breaking in terms of water surface elevation, however, the gradient of the velocity across the domain is not accurately captured. Consequently, the accretion of the bar crest and the increasing depth of the bar trough are not modelled by XBNH-IWST. The model accounts for a depth-averaged net return current (see Appendix H). However, XBNH-IWST lacks the representation of the vertical structure of the flow and sediment concentration, which if present, would allow to include the vertical structure of the net return current. Possible strategies for wave-resolving models to include the depth-variable undertow current for depth-averaged models based on Boussinesq-type equations are that by Lynett (2006) and that by Veeramony and Svendsen (2000) and Briganti et al. (2004). However, these approaches rely on the polynomial decomposition of the horizontal velocity in Boussinesq-type models. XBNH-IWST is based on the

one-layer version of the SWASH model, in which the horizontal and vertical velocities are numerically computed, without a closed form description of the velocity along the water column, hence these approaches cannot be used.

Moreover, since this study focuses on the cross-shore direction, a further development is required to obtain a two-dimensional horizontal (2DH) version of XBNH-IWST. 2DH equations for the flow have been already implemented in XBNH (see Smit et al., 2010). Therefore, the XBNH-IWST sediment transport governing equations need to be extended to account for the longshore direction.

This thesis advances the potential of nearshore simulations, including intra-swash dynamics on sandy beaches, by implementing a wave-resolving sediment transport formulation, which takes into account the effects of wave breaking-generated TKE, in an open-source non-hydrostatic, depth-averaged framework. However, this study also reveals that more sophisticated models are necessary to accurately predict the mutual feedback between the surf and swash zones, which feeds the development of breaker bars. Additionally, depth-resolving morphodynamics models (e.g., RANS model, such as OpenFOAM®) can be used to better understand the vertical structure of intra-wave sediment dynamics. These insights can be used to improve the parametrisations considered to simulate the sediment transport with other multi-layered and depth-integrated models (e.g., XBeach, Delft3D), which require lower computational time with respect to depth-resolving models, for the use among the community of coastal engineers.

A Available sediment transport model in Non-hydrostatic XBeach

The available sediment transport model in Non-Hydrostatic XBeach (Deltares, 2018), up-to-date until Mancini et al. (2021), uses a depth-averaged advection-diffusion transport equation according to Galappatti (1983):

$$\frac{\partial hC}{\partial t} + \frac{\partial\left[\left(huC + D_C h\frac{\partial C}{\partial x}\right)S_{sl}\right]}{\partial x} = \frac{hC_{eq} - hC}{T_s} = E - D, \tag{48}$$

where C is the depth-averaged suspended sediment concentration, T_s is the adaptation time, which represents the entrainment of the sediment, depending on h and the sediment fall velocity, w_s and C_{eq} is the total sediment equilibrium concentration. E and D are the erosion and deposition rate, respectively. When $E = D$, nor erosion or deposition occurs; as a consequence $C_{eq} = C$. D_C is the sediment diffusion coefficient and S_{sl} represents the bed slope effects computed following Deltares (2018). Therefore, the sediment transport rate, q_s, is computed as $q_s = \left(huC + D_C h\frac{\partial C}{\partial x}\right)S_{sl}$. The available sediment transport formulations in Non-Hydrostatic XBeach (e.g., Van Rijn et al., 2007; Van Thiel de Vries, 2009 and Soulsby, 1997; Van Rijn, 1984) calculate the equilibrium concentration for bed load and for suspended load separately, and then the total one. For both the bed load and the suspended load, referred to as b and s, respectively, the equilibrium concentrations, $C_{eq,b}$ and $C_{eq,s}$, depend on u and the root-mean-square wave orbital velocity, u_{rms}, as:

$$C_{eq,b,s} = \frac{A_{b,s}}{h}\left(\sqrt{u^2 + \gamma_1 u_{rms}^2} - u_{cr}\right)^{\gamma_2}, \tag{49}$$

where $A_{b,s}$ represents the bed load and suspended load coefficients, depending on sediments grain size and flow properties, γ_1 and γ_2 are two coefficients depending on the sediment transport formulation considered, respectively, and u_{cr} is the critical velocity determined as a function ("ϕ") of u and u_{rms}: $u_{cr} = \phi(|u|/(|u| + u_{rms}))$. The bed load transport rate, q_b, is computed as $q_b = uhC_{eq,b}S_{sl}$. Since aforementioned sediment transport formulations were originally developed for the surf-beat approach within XBeach, where the short wave energy is solved in a wave action balance, separately from the

wave-averaged flow, several issues arise when these formulations are used in combination with a wave-resolving approach:

- D_C is determined as the sum of the Smagorinsky (1963) constant, C_s and the contribution of the wave-averaged roller energy dissipation. Thus, when Non-Hydrostatic XBeach is used, then the contribution of the roller energy model is equal to zero and $D_C = C_s$;

- u_{rms} is computed as a parametrisation of the short wave energy Roelvink et al. (2009). Non-Hydrostatic XBeach solves the intra-wave flow through the extended NLSWE, and the total intra-wave cross-shore velocity is included in the term "u". Thus, when the phase-resolving version of XBeach is used, the term "u_{rms}" in Eq. (49) is equal to zero;

- the wave breaking-induced turbulence modelling in XBeach is based on a parametrisation of the short wave energy, thus, applicable only to the wave-averaged version of the model (Deltares, 2018). Consequently, there is no direct effect of turbulence in the available sediment transport modelling within Non-Hydrostatic XBeach.

A third approach for the available sediment transport modelling within Non-hydrostatic XBeach uses the Van Rijn et al. (1993) equations. This approach distinguishes between sediment transport below a reference height above the bed at which sediment is treated as bed load and above the reference height which is considered as suspended load. However, this approach was developed for the wave-averaged version of XBeach. Indeed, the numerical implementation follows the method used in the Delft3D model (see Deltares, 2018 and Deltares, 2006 for a more detailed description of the Van Rijn et al., 1993 approach). Moreover, in the XBeach-G model (McCall et al., 2014) for gravel beaches, several other sediment transport formulations are available for the bed load transport (see also Deltares, 2018).

B Roller energy balance modelling

The roller energy model herein described is based on the computation of the roller surface by using a roller energy balance similar to Svendsen (1984), which was originally developed for a wave-averaged framework. The roller energy balance (Svendsen, 1984) is solved as follows:

$$\frac{dE_r}{dt} = \frac{\partial E_r}{\partial t} + \frac{\partial E_r c}{\partial x} = Source_r - Sink_r, \tag{50}$$

where E_r is the kinetic roller energy normalised by the density, $Source_r$ is the loss of organised wave motion due to breaking and is computed using the time-varying wave energy model following Kobayashi and Wurjanto (1992) (i.e., Eqs. (23)-(27)); therefore, $Source_r = D_b$. $Sink_r$ is formulated in terms of the roller energy dissipation, D_r, which can be expressed as a function of E_r:

$$D_r = 2\beta\frac{g}{c}E_r, \tag{51}$$

where β is a dissipation coefficient given by the angle of inclination of the roller and set to 0.07; therefore, $Sink_r = D_r$. δ_R is computed using the roller volume, A_R, and it is computed (Svendsen, 1984) as:

$$\delta_R = \sqrt{A_R} = \sqrt{\frac{2E_r T_{rep}}{c}}, \tag{52}$$

where T_{rep} is the representative wave period.

The model described above was implemented in a MATLAB routine, which was used to compute E_r and δ_R by using the hydrodynamics computed with XBNH-IWST as inputs. In particular, inputs were derived from the simulations of the Ting and Kirby (1994) experiments for the plunging breaker with wave height, $H = 0.128$ m, and wave period, $T = 5$ s. To obtain the input variables for the roller energy balance model, XBNH-IWST was set up according to the experimental procedures and without including the effects of turbulence. Therefore, ν_h was modelled using the Smagorinsky (1963) model (Deltares, 2018). Time series of η and u were provided at the upstream boundary located 10 m from the toe of the sloped bed. η was determined using the 2^{nd}-order cnoidal wave theory as Svendsen (2006); u was given by the theory of shallow

water. A x-grid size, $\Delta x = 0.05$ m, was used. $c_f = 0.002$ was chosen following Reniers et al. (2013) and a minimum water depth, $h_{min} = 0.001$ m, was defined, below which a grid cell is considered dry. $\alpha_{br} = 0.4$, following the recommendations of Deltares (2018). Parameters, which are not mentioned are set to their default values.

Fig. B.1 shows the time series of h and $h - \delta_R$ at $x = 10.5$ m (i.e., approximately 2 m shoreward of the observed breaking point). Note that h does not take into account the effects of the wave breaking-generated turbulence. Results show that δ_R is not modelled properly. Therefore, this approach is found not suitable for a wave-resolving framework.

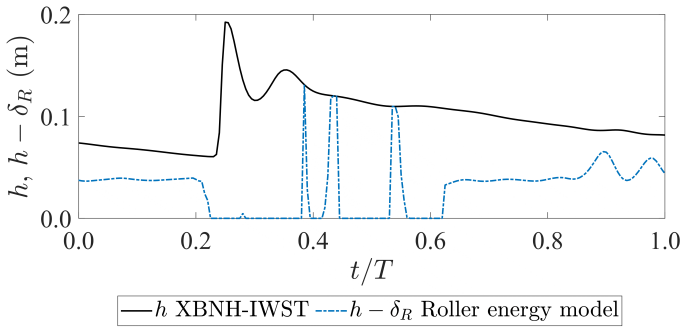

Figure B.1: Time series of h and $h - \delta_R$ at $x = 10.5$ m

C XBNH-IWST output file and model parameters

An example of the file called "xbeach.log", which lists all the parameters set prior to the numerical simulations, including those parameters which are set at their default values is herein shown. This file is generated for each numerical simulation. The reader is referred to Deltares (2018) for a detailed description of the keywords used for the model parameters and their recommended range of values.

```
************************************************************
Welcome to XBeach
version 1.23.5526 XBeachX release
URL:https://svn.oss.deltares.nl/repos/xbeach/branches/XBNH-Mancini
************************************************************
Simulation started: YYYYMMDD    hh:mm:ss     time zone (UTC)
                    20201106    17:55:05     -0000
General Input Module
Reading input parameters:
XBeach reading fromparams.txt
--------------------------------
Physical processes:
wavemodel = nonh
cyclic = 0.0000
swave = 0.0000
lwave = 0.0000
flow = 1.0000
sedtrans = 1.0000
morphology = 1.0000
avalanching = 1.0000
gwflow = 0.0000
vegetation = 0.0000
setbathy = 0.0000
viscosity = 1.0000
advection = 1.0000 (no record found, default value used)
```

```
--------------------------------
Grid parameters:
gridform =xbeach (no record found, default value used)
xori = 0.0000
yori = 0.0000 (no record found, default value used)
alfa = 0.0000
nx = 545.0000
ny = 0.0000
posdwn = 1.0000
depfile = bottom_newdown.txt
vardx = 1.0000
dx = -1.0000 (no record found, default value used)
dy = -1.0000 (no record found, default value used)
xfile = xd_down.txt
yfile = None specified
nz = 1.0000 (no record found, default value used)
--------------------------------
Model time parameters:
CFL = 0.7000
dtset = 0.0000 (no record found, default value used)
tstop = 1840.1900
maxdtfac = 500.0000 (no record found, default value used)
--------------------------------
Physical constants:
rho = 1025.0000
g = 9.8100
depthscale = 5.0000
--------------------------------
Initial conditions:
zsinitfile = None specified
--------------------------------
Wave boundary condition parameters:
```

```
wbctype = ts_nonh
taper = 100.0000
nmax = 0.8000 (no record found, default value used)
lateralwave = neumann
--------------------------------
Flow boundary condition parameters:
front = nonh_1d
left = wall
right = wall
back = abs_1d
ARC = 1.0000 (no record found, default value used)
order = 2.0000
highcomp = 0 (no record found, default value used)
freewave = 0 (no record found, default value used)
epsi = -1.0000 (no record found, default value used)
--------------------------------
Tide boundary conditions:
tideloc = 0.0000 (no record found, default value used)
zs0 = 0.0000 (no record found, default value used)
--------------------------------
Discharge boundary conditions:
disch_loc_file = None specified
disch_timeseries_file = None specified
ndischarge = 0.0000 (no record found, default value used)
ntdischarge = 0.0000 (no record found, default value used)
beta = 0.1000
--------------------------------
Flow parameters:
bedfriction = manning
bedfricfile = None specified
bedfriccoef = 0.0180
droot = 0.5000 (no record found, default value used)
```

```
dstem = 0.5000 (no record found, default value used)
maxcf = 0.0400 (no record found, default value used)
nuh = 0.1000 (no record found, default value used)
nuhfac = 1.0000
smag = 1.0000
friction_turbulence = 1.0000
gamma_turb = 1.0000
--------------------------------
Non-hydrostatic correction parameters:
solver =tridiag (no record found, default value used)
nodynamiccorrection = 0.0000
kdmin = 0.0000 (no record found, default value used)
Topt = 10.0000 (no record found, default value used)
nonhq3d = 0.0000
nhbreaker = 1.0000
nuh_mod = 4.0000
dispc = -1.0000 (no record found, default value used)
breakviscfac = 1.5000 (no record found, default value used)
maxbrsteep = 0.4000
reformsteep = 0.1000 (no record found, default value used)
nhturb = 1.0000
sourcesink_nhturb = 2.0000
sink_nhturb_kj = 0.0000
kb_nonh = 2.0000
facsw = 1.0000 (no record found, default value used)
facsr = 1.0000 (no record found, default value used)
facadv = 1.0000 (no record found, default value used)
rhoturb = 1.0000
facTaukb = 0.0000
facBedk = 0.0000
Dk = 0.3000 (no record found, default value used)
facML = 0.3000
```

```
facdyn = 1.0000
turbadv = lagrangian
--------------------------------
Sediment transport parameters:
form = pritchard_hogg_mpm_gm
sus = 1.0000
bed = 1.0000 (no record found, default value used)
bulk = 0.0000 (no record found, default value used)
facsl = 0.1500 (no record found, default value used)
z0 = 0.0060
smax = -1.0000 (no record found, default value used)
me_ph = 0.0100
n_ph = 1.5000
taubcr = 0.0000 (no record found, default value used)
taub_ref = 17.1000
facTaubref = 1.0000 (no record found, default value used)
vonkar = 0.4000 (no record found, default value used)
Trep = 1.0000 (no record found, default value used)
lengthref = 0.3900
bdslpeffmag = roelvink_total
bdslpeffini = total
bdslpeffdir = none (no record found, default value used)
reposeangle = 30.0000 (no record found, default value used)
tsfac = 0.1000 (no record found, default value used)
Tsmin = 0.5000
facDc = 1.0000
lwt = 0.0000
betad = 1.0000
dilatancy = 0.0000 (no record found, default value used)
--------------------------------
Bed composition parameters:
ngd = 1.0000 (no record found, default value used)
```

```
nd = 3.0000 (no record found, default value used)
por = 0.3600
D50 = 0.0002
D90 = 0.0004
rhos = 2650.0000
dzg = 0.1000 (no record found, default value used)
dzg1 = 0.1000 (no record found, default value used)
dzg2 = 0.1000 (no record found, default value used)
dzg3 = 0.1000 (no record found, default value used)
sedcal = 1.0000 (no record found, default value used)
ucrcal = 1.0000 (no record found, default value used)
--------------------------------
Morphology parameters:
morfac = 1.0000
morfacopt = 1.0000
morstart = 0.0000
morstop = 1840.1900 (no record found, default value used)
wetslp = 0.3000
dryslp = 1.0000
hswitch = 0.1000 (no record found, default value used)
dzmax = 0.0500 (no record found, default value used)
struct =0 (no record found, default value used)
--------------------------------
Output variables:
timings = 1.0000 (no record found, default value used)
tunits = None specified
tstart = 0.0000
tint = 1.0000 (no record found, default value used)
tsglobal = None specified
tintg = 0.1000
tspoints = None specified
tintp = 0.0250
```

```
tsmean = None specified
tintm = 1840.1900 (no record found, default value used)
nglobalvar = 10
nglobalvar: Will generate global output for variable:zs
nglobalvar: Will generate global output for variable:zb
nglobalvar: Will generate global output for variable:ue
nglobalvar: Will generate global output for variable:Susg
nglobalvar: Will generate global output for variable:Subg
nglobalvar: Will generate global output for variable:ccg
nglobalvar: Will generate global output for variable:cctot
nglobalvar: Will generate global output for variable:hh
nglobalvar: Will generate global output for variable:kturb
nglobalvar: Will generate global output for variable:kb
nrugdepth = 1.0000 (no record found, default value used)
rugdepth = 0.0000 (no record found, default value used)
nmeanvar = 0.0000 (no record found, default value used)
outputformat = fortran
remdryoutput = 0.0000 (no record found, default value used)
--------------------------------
Output projection:
projection = None specified
rotate = 1.0000 (no record found, default value used)
--------------------------------
Wave numerics parameters:
scheme =nupwind_2
snells = 0.0000
--------------------------------
Flow numerics parameters:
eps = 0.0050 (no record found, default value used)
eps_sd = 0.5000 (no record found, default value used)
umin = 0.0000 (no record found, default value used)
hmin = 0.2000 (no record found, default value used)
```

```
secorder = 1.0000
--------------------------------
Sediment transport numerics parameters:
thetanum = 1.0000 (no record found, default value used)
sourcesink = 1.0000
cmax = 0.4000
--------------------------------
Bed update numerics parameters:
frac_dz = 0.7000 (no record found, default value used)
nd_var = 2.0000 (no record found, default value used)
split = 1.0100 (no record found, default value used)
merge = 0.0100 (no record found, default value used)
--------------------------------
Finished reading input parameters
--------------------------------
Warning: input parameters eps, hmin, hswitch and dzmax are scaled with
depthscale to:
eps = 0.0010
hmin = 0.0400
hswitch = 0.0200
dzmax = 0.0045
maxerror = -24.6000
-----------------------------------
Building Grid and Bathymetry
-----------------------------------
Initializing .....
Fortran outputformat
Setting up boundary conditions
Boundary conditions complete, starting computation
Average dt  0.003 seconds
Duration   :  601.9844 seconds
Timesteps  :  658143
```

```
Average dt :  2.7960E-003 seconds

Unit speed :  1.6752E-006 seconds/1

End of program xbeach
```

D Back calculation of m_e from laboratory experiments

The parameter m_e is the least well determined parameter among the parameters included in the Pritchard and Hogg (2003) transport equation because there are no empirical formulations which can describe it. However, because no field data are available to provide its estimates, the only comparison with the findings of the present study are previous numerical studies (see e.g., Zhu and Dodd, 2015 and Incelli, 2016). Therefore, in this section an attempt to find a more detailed description of m_e is illustrated. In particular, m_e was back computed by using the experimental data of the CoSSedM project (Alsina et al., 2016). Then, the values obtained were analysed by considering the flow and the sediment transport conditions.

Computation of m_e was carried out for SEG2 (i.e., far from the morphodynamic equilibrium) and SEG7 (i.e., close to the morphodynamic equilibrium) of BE1_2. Each term of Eq. 11 was computed considering two locations at different x-coordinates in the swash zone (i.e., $x = x_1 = 75.36$ m and $x = x_2 = 75.81$ m; see also Fig. 5.1) and using a discretization in space and time; then m_e was computed. x_1 and x_2 are the closest x-coordinates where measurements of C_z were available. At x_1 the OBS sensor is located at $d_z = 0.05$ m, while at x_2 two OBS sensors were located at $d_z = 0.03$ m and $d_z = 0.08$ m. Therefore, for x_2, the average of the two measurements, C, was considered. The computation of each term of Eq. (11) was carried out over a sequence of 195 s (i.e., over T_r) at each instance, considering a sampling interval of 0.01 s. For simplicity, the diffusion term and the bed slope effects were not considered. λ and R were considered to their reference values, i.e., $\lambda = 1$ m and $R = 1$.

In Fig. D.1 m_e is plotted against u at x_2 for SEG2 (Fig. D.1*a*) and SEG7 (Fig. D.1*b*). Fig. D.2 shows m_e plotted against huC at x_2 for SEG2 (Fig. D.2*a*) and SEG7 (Fig. D.2*b*). For both segments, results show an increasing order of magnitude of m_e in the proximity to flow reversal (i.e., $u = 0$ m/s). When u reaches a zero value, the sediment is not stirred up by the bed shear stress, which is in turn close to zero as well. Differences in the values of m_e between SEG2 and SEG7 in Fig. D.1 are mostly visible for the backwash phase of the flow (i.e., $u < 0$ m/s), whereas during the uprush stage (i.e., $u > 0$ m/s) there is not a clear distinction between the two segments. In particular, for the largest orders of magnitude of u during the backwash the order of magnitude

of m_e ranges between 10^{-3} and 10^{0} for SEG2, while it ranges between 10^{-4} and 10^{-1} for SEG7. For the highest values of u during the uprush the order of magnitude of m_e converges to 10^{-1} for both segments.

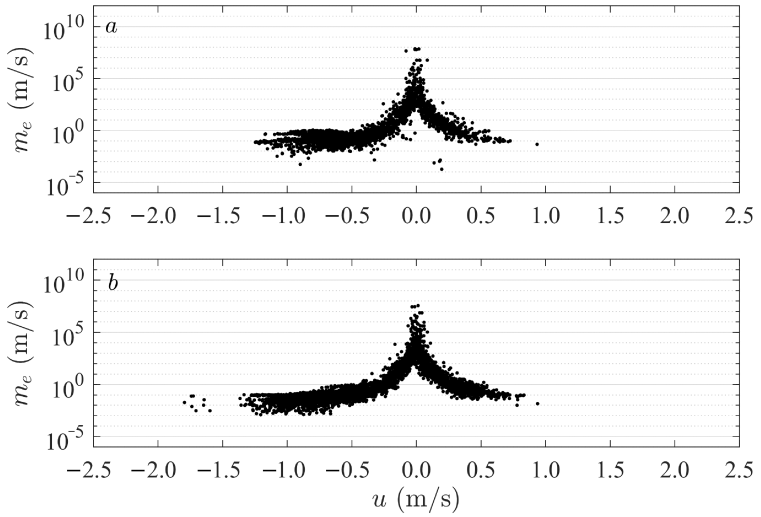

Figure D.1: m_e plotted against u for BE1_2; *a*: SEG2; *b*: SEG7

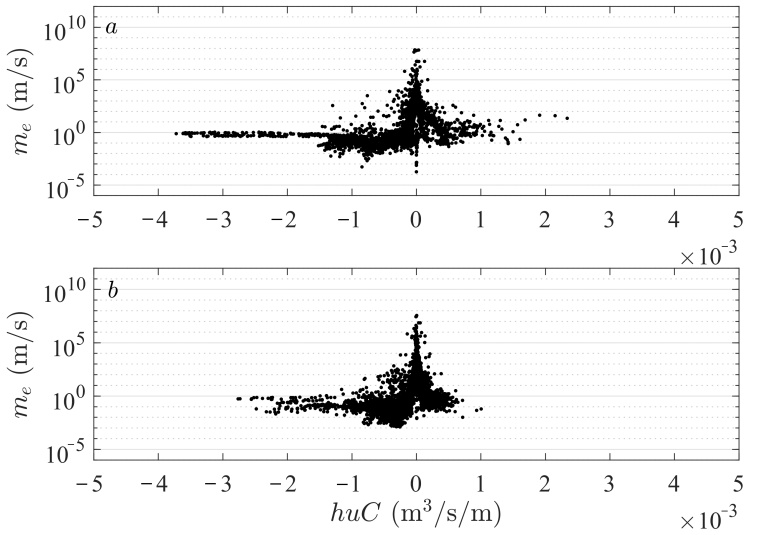

Figure D.2: m_e plotted against huC for BE1_2; *a*: SEG2; *b*: SEG7

Fig. D.2 shows that m_e increases when the order of magnitude of huC increases in both the uprush and backwash phases of the flow for both SEG2 and SEG7. As expected, the order of magnitude of huC is lower for SEG7 than SEG2, which is farther from the equilibrium in terms of bed evolution than SEG7. Consequently, the order of magnitude of m_e ranges between lower values for SEG7 than SEG2, especially for the backwash

phase of the flow. Results shown in this appendix were used to choose the range of values for m_e in the sensitivity analysis carried out in Section 5.3.3.

E Morphodynamic sensitivity to the variation of γ_k

Fig. E.1 shows Δz_{b_f} predicted by using the *brkTurb* modelling configuration by varying the value of γ_k, with the corresponding nRMSE and RMSTE in Table E.1. By increasing γ_k, the deposition in the upper swash zone increase as well, however, results show that variation of the γ_k within the range of values considered does not improve the prediction of the beach evolution. This is confirmed by the similar values of nRMSE and RMSTE for the three cases considered.

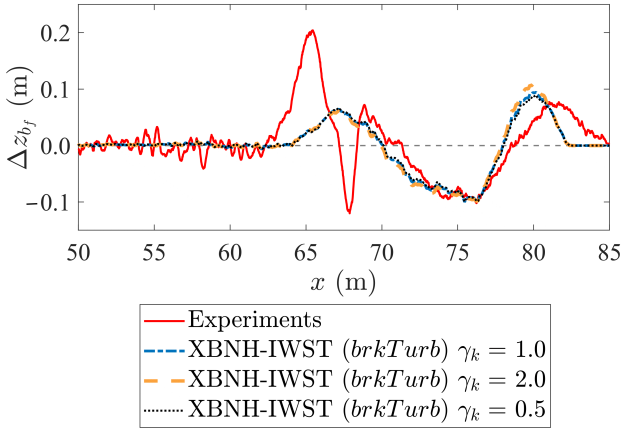

Figure E.1: Δz_{b_f} after SEG1 of BE1_2 for different values of γ_k

Table E.1: nRMSE and RMSTE for Δz_{b_f} after SEG1 of BE1_2 for different values of γ_k.

γ_k	nRMSE	RMSTE (m^2)
0.5	0.0429	0.3333
1	0.0433	0.3359
2	0.0440	0.3331

F Morphodynamic response using the Nielsen (2002) formula

In XBNH the effects of flow acceleration in the computation of the bed shear stress can be taken into account either by using the McCall (2015) formulation or the Nielsen (2002) expression. The former was developed and validated for gravel beaches, therefore it is not considered in this study. The Nielsen (2002) expression allows to include the effects of flow acceleration on sediment transport in the computation of the bed shear stress as:

$$\tau_b = \rho c_f \left(\cos\phi_t u + \frac{1}{\omega_{rep}} \sin\phi_t \frac{\partial u}{\partial t} \right)^2 \text{sign}(u), \tag{53}$$

where $\omega_{rep} = 1/T_{rep}$ is the representative wave angular frequency and ϕ_t represents the phase shift between the flow velocity and bed shear stress. By increasing ϕ_t a stronger bed shear stress is generated under the higher accelerated part of the event (i.e., uprush). Hence, a landward sediment transport is promoted. Instead, when $\phi_t = 0°$, the effect of the inertia term is equal to zero and $\tau_b = \rho c_f u|u|$. The recommended value of ϕ_t is 25° (Deltares, 2018). Fig. F.1*a*, *b* and *c* shows the z_{b_f}, Δz_{b_f} and $\bar{q}_{sed}$, respectively, over SEG1 of BE1_2 obtained with XBNH-IWST including the Nielsen (2002) formula, which is referred to as XBNH-IWST (Nielsen) in Fig. F.1.

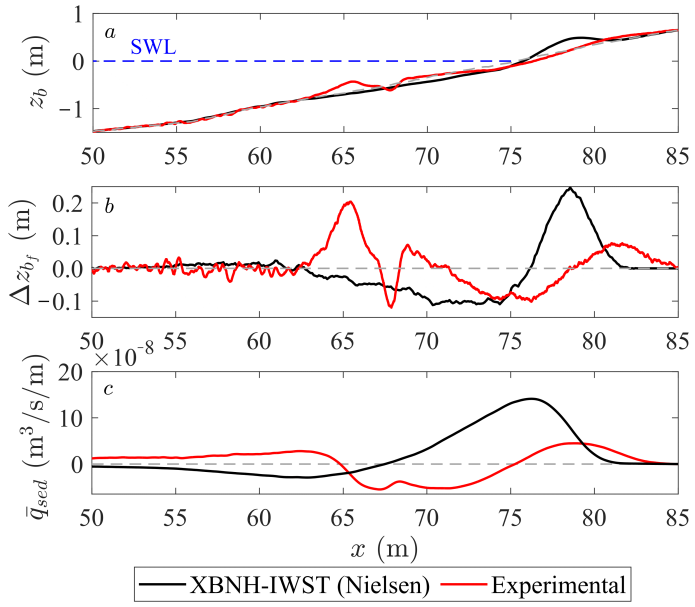

Figure F.1: *a*: z_{b_f} after SEG1 of BE1_2; *b*: Δz_{b_f} after SEG1 of BE1_2; *c*: $\bar{q}_{sed}$ over SEG1 of BE1_2

Results show that the inclusion of the Nielsen (2002) formula does not improve numerical predictions in terms of beach evolution and sediment transport rate from a qualitative point of view. Indeed, The model overestimates the deposition in the upper swash zone and the breaker bar in the surf zone is not obtained. In turn, the modelled $\bar{q}_{sed}$ is found to be always higher than zero in the lower swash zone, unlike the observations.

G XBNH-IWST and SWASH modelling of the Van der Zanden et al. (2016) velocity for different boundary conditions

Different Boundary Conditions (BC) were considered to further assess the performance of the velocity modelling with XBNH-IWST for the Van der Zanden et al. (2016) experiments. Two additional BC were considered for the forcing conditions provided at the model upstream boundary:

- "BC_0 - LWT": time series of η and u were provided at the upstream boundary located at the position of the wave paddle in the wave flume (i.e., $x = 0$ m), by using the Linear Wave Theory (LT) and the target $T = 4$ s and $H = 0.85$ m.
- "BC_{51} - EXP": time series of η and u were provided at the upstream boundary located at $x = 51$ m (i.e., on the seaward bar slope), considering the experimental post-processed phase-averaged η and u measured at the same x-coordinate.

If not specified, the BC applied is that used in Section 5.5.3. Additionally, simulations were carried out for different bed configurations (see also Fig. G.1). The non-erodible structure was removed and the plateau, located shoreward of the bar (for $x > 57.5$ m), was extended (referred to as "*extended plateau*"). The extension of the aforementioned plateau was reduced and the length of the sloping structure was increased (referred to as "*reduced plateau*"). For one of the alternative bed configurations, the structure was also considered as erodible (referred to as "*erodible structure*").

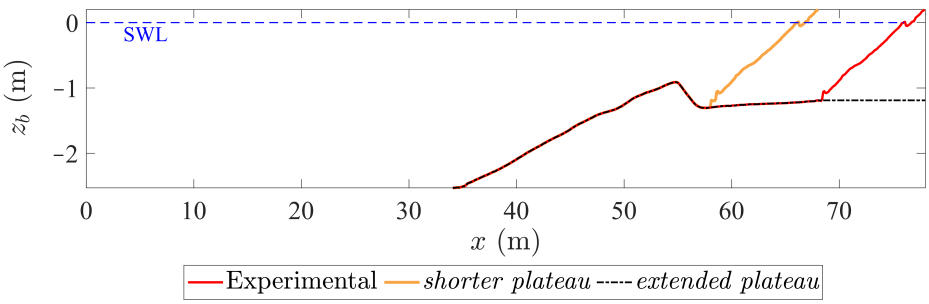

Figure G.1: Initial z_b for different bed configurations

Simulations were also carried out using the SWASH model. For the latter simulations, the model was set up similarly to XBNH-IWST and 3 layers were used.

Fig. G.2 shows the distribution of $\bar{u}$ for XBNH-IWST and SWASH. The comparison is herein illustrated only from a qualitative point view. Results show that the XBNH-IWST predicted distribution of $\bar{u}$ are similar for all the modelling configurations considered. $\bar{u}$ modelled with SWASH by using 3 layers is qualitatively similar to those obtained with XBNH-IWST.

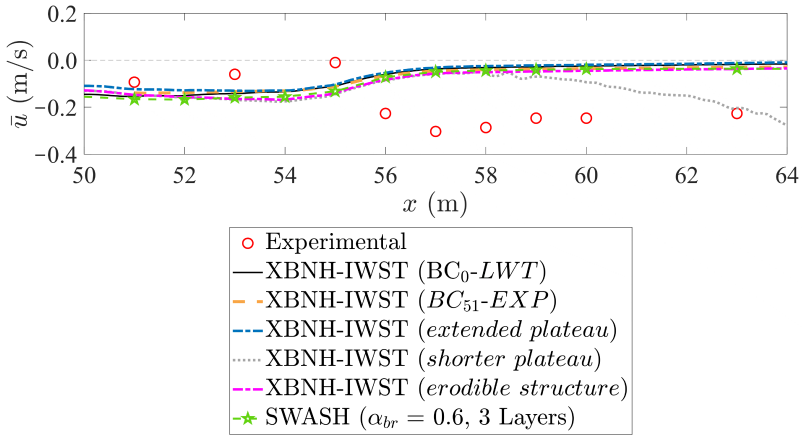

Figure G.2: Distribution of $\bar{u}$ across the x-domain for different BCs and bed configuration; grey-dashed line: reference line

H Representation of the net return flow in XBNH-IWST

Since the hydrodynamics modelling in XBNH-IWST is based on the one-layer version of the SWASH model, no vertical discretization of the velocity profile is available. Therefore, only a depth- and phase-averaged net current can be obtained from the model. Results show that the predicted net current is directed offshore. Fig. H.1 shows the modelled and experimental u for SEG1 of BE1_2 for the Alsina et al. (2016) case and the wave-averaged velocity over the wave group period, $T_g = 15$ s, u_{mean}; $u_{mean} = -0.53$ m/s for XBNH-IWST and $u_{mean} = -0.48$ m/s for the experiments. Fig. H.1 also shows the modelled $q_{tot} = q_s + q_b$ for the same segment. q_{tot} is also depth-averaged, and the presence of a net depth-averaged velocity leads to net mean offshore transport, $q_{tot,mean} = -0.0019$ m^3/m/s, even if entrainment is considered.

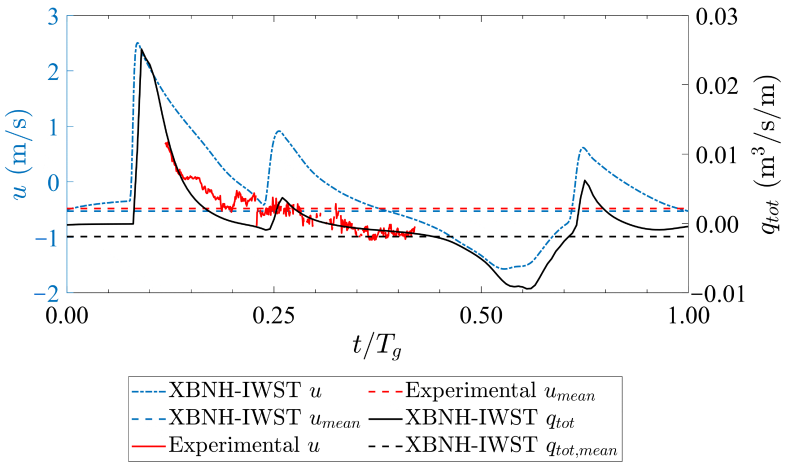

Figure H.1: Time series of u and q_{tot} at $x = 75.81$ m; and u_{mean} and $q_{tot,mean}$ at $x = 75.81$ m over T_g for SEG1 of BE1_2

References

Aagaard, T., Kroon, A., Hughes, M.G., Greenwood, B., 2008. Field observations of nearshore bar formation. *Earth Surface Processes and Landforms* 33(7), 1021–1032.

Ahrens, J.P., 2000. A fall-velocity equation. *Journal of Waterway, Port, Coastal, and Ocean Engineering* 126(2), 99–102.

Alsina, J.M., Cáceres, I., Brocchini, M., Baldock, T.E., 2012. An experimental study on sediment transport and bed evolution under different swash zone morphological conditions. *Coastal Engineering* 68, 31–43.

Alsina, J.M., Falchetti, S., Baldock, T.E., 2009. Measurements and modelling of the advection of suspended sediment in the swash zone by solitary waves. *Coastal Engineering* 56(5-6), 621–631.

Alsina, J.M., Padilla, E.M., Cáceres, I., 2016. Sediment transport and beach profile evolution induced by bi-chromatic wave groups with different group periods. *Coastal Engineering* 114, 325–340.

Alsina, J.M., Van der Zanden, J., Caceres, I., Ribberink, J.S., 2018. The influence of wave groups and wave-swash interactions on sediment transport and bed evolution in the swash zone. *Coastal Engineering* 140, 23–42.

Antuono, M., Soldini, L., Brocchini, M., 2012. On the role of the Chezy frictional term near the shoreline. *Theoretical and Computational Fluid Dynamics* 26(1-4), 105–116.

Bagnold, R.A., 1956. The flow of cohesionless grains in fluids. *Philosophical Transactions of the Royal Society of London. Series A, Mathematical and Physical Sciences* 249(964), 235–297.

Bai, Y., Yamazaki, Y., Fai Cheung, K., 2018. Convergence of multilayer nonhydrostatic models in relation to boussinesq-type equations. *Journal of Waterway, Port, Coastal, and Ocean Engineering* 144(2), 06018001.

Baldock, T., Birrien, F., Atkinson, A., Shimamoto, T., Wu, S., Callaghan, D., Nielsen, P., 2017. Morphological hysteresis in the evolution of beach profiles under sequences of wave climates-part 1; observations. *Coastal Engineering* 128, 92–105.

Baldock, T., Manoonvoravong, P., Pham, K.S., 2010. Sediment transport and beach morphodynamics induced by free long waves, bound long waves and wave groups. *Coastal Engineering* 57(10), 898–916.

Barnes, M., Baldock, T., 2010. A lagrangian model for boundary layer growth and bed shear stress in the swash zone. *Coastal Engineering* 57(4), 385–396.

Battjes, J.A., 1975. Surf similarity, *in: Coastal Engineering 1974*, pp. 466–480.

Bosboom, J., Mol, M., Reniers, A., Stive, M., de Valk, C., 2020. Optimal sediment transport for morphodynamic model validation. *Coastal Engineering* 158, 103662.

Briganti, R., Dodd, N., Incelli, G., Kikkert, G., 2018. Numerical modelling of the flow and bed evolution of a single bore-driven swash event on a coarse sand beach. *Coastal Engineering* 142, 62–76.

Briganti, R., Dodd, N., Kelly, D., Pokrajac, D., 2012. An efficient and flexible solver for the simulation of the morphodynamics of fast evolving flows on coarse sediment beaches. *International Journal for Numerical Methods in Fluids* 69(4), 859–877.

Briganti, R., Dodd, N., Pokrajac, D., O'Donoghue, T., 2011. Non linear shallow water modelling of bore-driven swash: Description of the bottom boundary layer. *Coastal Engineering* 58(6), 463–477.

Briganti, R., Musumeci, R., Bellotti, G., Brocchini, M., Foti, E., 2004. Boussinesq modeling of breaking waves: Description of turbulence. *Journal of Geophysical Research: Oceans* 109(C7).

Briganti, R., Torres-Freyermuth, A., Baldock, T.E., Brocchini, M., Dodd, N., Hsu, T.J., Jiang, Z., Kim, Y., Pintado-Patiño, J.C., Postacchini, M., 2016. Advances in numerical modelling of swash zone dynamics. *Coastal Engineering* 115, 26–41.

Brocchini, M., 2013. A reasoned overview on Boussinesq-type models: the interplay between physics, mathematics and numerics. *Proceedings of the Royal Society A: Mathematical, Physical and Engineering Sciences* 469(2160), 20130496.

Brocchini, M., Baldock, T.E., 2008. Recent advances in modeling swash zone dynamics: Influence of surf-swash interaction on nearshore hydrodynamics and morphodynamics. *Reviews of Geophysics* 46(3).

Cáceres, I., Alsina, J.M., van Der Zanden, J., Ribberink, J.S., Sánchez-Arcilla, A., et al., 2020. The effect of air bubbles on optical backscatter sensor measurements under plunging breaking waves. *Coastal Engineering* 159, 103721.

Chardón-Maldonado, P., Pintado-Patiño, J.C., Puleo, J.A., 2016. Advances in swash-zone research: Small-scale hydrodynamic and sediment transport processes. *Coastal Engineering* 115, 8–25.

Ciavola, P., Coco, G., 2017. Coastal storms: processes and impacts. John Wiley & Sons, Chichester, UK.

Coco, G., Senechal, N., Rejas, A., Bryan, K.R., Capo, S., Parisot, J., Brown, J.A., MacMahan, J.H., 2014. Beach response to a sequence of extreme storms. *Geomorphology* 204, 493–501.

Dean, R.G., Dalrymple, R.A., 1991. Water wave mechanics for engineers and scientists. Volume 2. World Scientific Publishing Company, Singapore.

Deigaard, R., et al., 1992. Mechanics of coastal sediment transport. Volume 3. World Scientific, Singapore.

Deltares, 2006. Delft3D-FLOW-User Manual. WL Delft Hydraulics, The Netherlands.

Deltares, 2018. XBeach Documentation: Release XBeach v1.23.5527 XBeachX FINAL, <https://xbeach.readthedocs.io> .

Dingemans, M.W., 1994. Water wave propagation over uneven bottoms. *Ph.D thesis.* Delft University of Technology.

Dubarbier, B., Castelle, B., Marieu, V., Ruessink, G., 2015. Process-based modeling of cross-shore sandbar behavior. *Coastal Engineering* 95, 35–50.

Eichentopf, S., Cáceres, I., Alsina, J.M., 2018. Breaker bar morphodynamics under erosive and accretive wave conditions in large-scale experiments. *Coastal Engineering* 138, 36–48.

Eichentopf, S., Van der Zanden, J., Cáceres, I., Baldock, T.E., Alsina, J.M., 2020. Influence of storm sequencing on breaker bar and shoreline evolution in large-scale experiments. *Coastal Engineering* 157, Article 103659.

Galappatti, R., 1983. A depth integrated model for suspended transport. *Communications on Hydraulics, 1983-07* .

Gallagher, E.L., Elgar, S., Guza, R., 1998. Observations of sand bar evolution on a natural beach. *Journal of Geophysical Research: Oceans* 103(C2), 3203–3215.

Gourlay, M., Van Der Meulen, 1969. Beach and dune erosion tests. *Proceedings of the 11th Conference on Coastal Engineering, London, UK* 1, 701–707.

Hoefel, F., Elgar, S., 2003. Wave-induced sediment transport and sandbar migration. *Science* 299(5614), 1885–1887.

Howe, D., Blenkinsopp, C.E., Turner, I.L., Baldock, T.E., Puleo, J.A., 2019. Direct measurements of bed shear stress under swash flows on steep laboratory slopes at medium to prototype scales. *Journal of Marine Science and Engineering* 7(10), 358.

Hsu, T.J., Elgar, S., Guza, R., 2006. Wave-induced sediment transport and onshore sandbar migration. *Coastal Engineering* 53(10), 817–824.

Incelli, G., 2016. A fully-coupled coastal hydro-morphodynamical numerical solver. *Ph.D Thesis.* University of Nottingham.

Incelli, G., Dodd, N., Blenkinsopp, C.E., Zhu, F., Briganti, R., 2016. Morphodynamical modelling of field-scale swash events. *Coastal Engineering* 115, 42–57.

Jacobsen, N.G., Fredsoe, J., 2014. Formation and development of a breaker bar under regular waves. part 2: Sediment transport and morphology. *Coastal Engineering* 88, 55–68.

Jacobsen, N.G., Fredsoe, J., Jensen, J.H., 2014. Formation and development of a breaker bar under regular waves. part 1: Model description and hydrodynamics. *Coastal Engineering* 88, 182–193.

Kennedy, A.B., Chen, Q., Kirby, J.T., Dalrymple, R.A., 2000. Boussinesq modeling of wave transformation, breaking, and runup. i: 1d. *Journal of Waterway, Port, Coastal, and Ocean Engineering* 126(1), 39–47.

Kim, D.H., Sanchez-Arcilla, A., Caceres, I., 2017. Depth-integrated modelling on onshore and offshore sandbar migration: Revision of fall velocity. *Ocean Modelling* 110, 21 – 31.

Kim, Y., Mieras, R.S., Cheng, Z., Anderson, D., Hsu, T.J., Puleo, J.A., Cox, D., 2019. A numerical study of sheet flow driven by velocity and acceleration skewed near-breaking waves on a sandbar using sedwavefoam. *Coastal Engineering* 152, 103526.

Kobayashi, N., Wurjanto, A., 1992. Irregular wave setup and run-up on beaches. *Journal of Waterway, Port, Coastal, and Ocean Engineering* 118(4), 368–386.

Kolmogorov, A., 1942. Equations of motion of an incompressible turbulent fluid. *Izvestiya Akademii Nauk SSSR, Ser.* 6(6), 56–58.

Kranenborg, J., Campmans, G., Jacobsen, N., Werf, J.v.d., McCall, R., Reniers, A., Hulscher, S., 2020. RANS modelling of cross-shore sediment transport and morphodynamics in the swash-zone. *Coastal Engineering Proceedings* (36v), sediment.14.

Kranenborg, J., Campmans, G., van der Werf, J., Reniers, A., Hulscher, S., 2019. Depth-resolving vs depth-averaged modelling of swash zone hydrodynamics. *Coastal Structures 2019* , 834–840.

Larsen, B.E., van der Zanden, J., Ruessink, G., Fuhrman, D.R., et al., 2020. Stabilized RANS simulation of surf zone kinematics and boundary layer processes beneath large-scale plunging waves over a breaker bar. *Ocean Modelling* 155, 101705.

Launder, B.E., Spalding, D.B., 1972. Mathematical models of turbulence. Academic Press, New York.

Lesser, G.R., Roelvink, J.a., van Kester, J.a.T.M., Stelling, G.S., 2004. Development and validation of a three-dimensional morphological model. *Coastal Engineering* 51, 883–915.

Li, J., Qi, M., Fuhrman, D.R., 2019. Numerical modeling of flow and morphology induced by a solitary wave on a sloping beach. *Applied Ocean Research* 82, 259–273.

Longuet-Higgins, M.S., Stewart, R., 1962. Radiation stress and mass transport in gravity waves, with application to surf beats. *Journal of Fluid Mechanics* 13(4), 481–504.

Luijendijk, A., Hagenaars, G., Ranasinghe, R., Baart, F., Donchyts, G., Aarninkhof, S., 2018. The state of the world's beaches. *Scientific Reports* 8(1), 1–11.

Lynett, P.J., 2006. Wave breaking velocity effects in depth-integrated models. *Coastal Engineering* 53(4), 325–333.

Mancini, G., Briganti, R., McCall, R., Dodd, N., Zhu, F., 2021. Numerical modelling of intra-wave sediment transport on sandy beaches using a non-hydrostatic, wave-resolving model. *Ocean Dynamics* 71(1), 1–20.

Masselink, G., Gehrels, R., 2014. Coastal environments and global change. John Wiley & Sons, Chichester, UK.

Masselink, G., Puleo, J.A., 2006. Swash-zone morphodynamics. *Continental Shelf Research* 26(5), 661–680.

McCall, R., Masselink, G., Poate, T., Roelvink, J., Almeida, L., 2015. Modelling the morphodynamics of gravel beaches during storms with XBeach-G. *Coastal Engineering* 103, 52–66.

McCall, R., Masselink, G., Poate, T., Roelvink, J., Almeida, L., Davidson, M., Russell, P., 2014. Modelling storm hydrodynamics on gravel beaches with XBeach-G. *Coastal Engineering* 91, 231–250.

McCall, R.T., 2015. Process-based modelling of storm impacts on gravel coasts. *Ph.D Thesis.* Plymouth University.

McCormack, R., 1969. The effect of viscosity in hypervelocity impact cratering. *AIAA Hyper Velocity Impact Conference* (69-354).

Mei, C.C., 1989. The applied dynamics of ocean surface waves. World Scientific, Singapore.

Meyer-Peter, E., Müller, R., 1948. Formulas for bed-load transport, *in: Proceedings of the Internationl Association for Hydraulic Research, 2nd meeting, Stockholm. Appendix 2*, IAHR.

Mieras, R.S., Puleo, J.A., Anderson, D., Cox, D.T., Hsu, T.J., 2017. Large-scale experimental observations of sheet flow on a sandbar under skewed-asymmetric waves. *Journal of Geophysical Research: Oceans* 122(6), 5022–5045.

Nielsen, P., 2002. Shear stress and sediment transport calculations for swash zone modelling. *Coastal Engineering* 45(1), 53–60.

O'Donoghue, T., Kikkert, G.A., Pokrajac, D., Dodd, N., Briganti, R., 2016. Intra-swash hydrodynamics and sediment flux for dambreak swash on coarse-grained beaches. *Coastal Engineering* 112, 113–130.

Postacchini, M., Brocchini, M., Mancinelli, A., Landon, M., 2012. A multi-purpose, intra-wave, shallow water hydro-morphodynamic solver. *Advances in Water Resources* 38, 13–26.

Prandtl, L., 1945. Uber ein neues Formelsystem für die ausgebildete Turbulenz. *Nachrichten von der Akademie der Wissenschaft in Göttingen* 6, 6–19.

Pritchard, D., Hogg, A.J., 2003. Suspended sediment transport under seiches in circular and elliptical basins. *Coastal Engineering* 49(1-2), 43–70.

Pritchard, D., Hogg, A.J., 2005. On the transport of suspended sediment by a swash event on a plane beach. *Coastal Engineering* 52(1), 1–23.

Puleo, J., Beach, R., Holman, R.A., Allen, J., 2000. Swash zone sediment suspension and transport and the importance of bore-generated turbulence. *Journal of Geophysical Research: Oceans* 105(C7), 17021–17044.

Puleo, J.A., Blenkinsopp, C., Conley, D., Masselink, G., Turner, I.L., Russell, P., Buscombe, D., Howe, D., Lanckriet, T., McCall, R., et al., 2014. Comprehensive field study of swash-zone processes. i: Experimental design with examples of hydrodynamic and sediment transport measurements. *Journal of Waterway, Port, Coastal, and Ocean Engineering* 140(1), 14–28.

Reniers, A., Gallagher, E., MacMahan, J., Brown, J., Van Rooijen, A., de Vries, J.v.T., Van Prooijen, B., 2013. Observations and modeling of steep-beach grain-size variability. *Journal of Geophysical Research: Oceans* 118(2), 577–591.

Rijnsdorp, D.P., Smit, P.B., Zijlema, M., Reniers, A.J., 2017. Efficient non-hydrostatic modelling of 3D wave-induced currents using a subgrid approach. *Ocean Modelling* 116, 118–133.

Roelvink, D., McCall, R., Mehvar, S., Nederhoff, K., Dastgheib, A., 2018. Improving predictions of swash dynamics in XBeach: The role of groupiness and incident-band runup. *Coastal Engineering* 134, 103–123.

Roelvink, D., Reniers, A., Van Dongeren, A., de Vries, J.v.T., McCall, R., Lescinski, J., 2009. Modelling storm impacts on beaches, dunes and barrier islands. *Coastal Engineering* 56(11), 1133–1152.

Roelvink, J., Stive, M., 1989. Bar-generating cross-shore flow mechanisms on a beach. *Journal of Geophysical Research: Oceans* 94(C4), 4785–4800.

Ruffini, G., Briganti, R., Alsina, J., Brocchini, M., Dodd, N., McCall, R., 2020. Numerical modelling of flow and bed evolution of bichromatic wave groups on an intermediate beach using non-hydrostatic XBeach. *Journal of Waterway, Port, Coastal, and Ocean Engineering* 146(1), 04019034.

Schnitzler, B., 2015. Modeling sand transport under breaking waves. *MSc Thesis.* University of Twente.

Smagorinsky, J., 1963. General circulation experiments with the primitive equations: I. the basic experiment. *Monthly Weather Review* 91(3), 99–164.

Smit, P., Stelling, G., Roelvink, D., Van Thiel de Vries, J., McCall, R., van Dongeren, A., Zwinkels, C., Jacobs, R., 2010. XBeach: Non-hydrostatic model. *Technical Report.* Delft University of Technology and Deltares.

Smit, P., Zijlema, M., Stelling, G., 2013. Depth-induced wave breaking in a non-hydrostatic, near-shore wave model. *Coastal Engineering* 76, 1–16.

Soulsby, R., 1997. Dynamics of marine sands: a manual for practical applications. Thomas Telford, London, UK.

Stelling, G., Zijlema, M., 2003. An accurate and efficient finite-difference algorithm for non-hydrostatic free-surface flow with application to wave propagation. *International Journal for Numerical Methods in Fluids* 43(1), 1–23.

Sumer, B., Jensen, B., Fredsøe, J., 1987. Turbulence in oscillatory boundary layers, *in: Advances in Turbulence*. Springer, Heidelberg, Germany, pp. 556–567.

Svendsen, I.A., 1984. Wave heights and set-up in a surf zone. *Coastal Engineering* 8(4), 303–329.

Svendsen, I.A., 2006. Introduction to nearshore hydrodynamics. Volume 24. World Scientific, Singapore.

Svendsen, I.A., Schäffer, H.A., Hansen, J.B., 1987. The interaction between the undertow and the boundary layer flow on a beach. *Journal of Geophysical Research: Oceans* 92(C11), 11845–11856.

Symonds, G., Huntley, D.A., Bowen, A.J., 1982. Two-dimensional surf beat: Long wave generation by a time-varying breakpoint. *Journal of Geophysical Research: Oceans* 87(C1), 492–498.

Ting, F.C., Kirby, J.T., 1994. Observation of undertow and turbulence in a laboratory surf zone. *Coastal Engineering* 24(1-2), 51–80.

Titov, V.V., Synolakis, C.E., 1995. Modeling of breaking and nonbreaking long-wave evolution and runup using VTCS-2. *Journal of Waterway, Port, Coastal, and Ocean Engineering* 121(6), 308–316.

Toimil, A., Losada, I., Nicholls, R., Dalrymple, R., Stive, M., 2020. Addressing the challenges of climate change risks and adaptation in coastal areas: A review. *Coastal Engineering* 156, 103611.

Turner, I.L., Masselink, G., 1998. Swash infiltration-exfiltration and sediment transport. *Journal of Geophysical Research: Oceans* 103(C13), 30813–30824.

Van Der Zanden, J., Alsina, J.M., Cáceres, I., Buijsrogge, R.H., Ribberink, J.S., 2015. Bed level motions and sheet flow processes in the swash zone: Observations with a new conductivity-based concentration measuring technique (ccm+). *Coastal Engineering* 105, 47–65.

Van Der Zanden, J., Fernandezx-Mora, A., van der A, D., Hurther, D., Caceres, I., O'Donoghue, T., Ribberink, J.S., 2017a. Incusion of wave breaking turbulence in

reference concenration models. *Coastal Dynamics 2017, Helsingør, Denmark* , 629–641Paper 188.

Van Der Zanden, J., Hurther, D., Caceres, I., O'Donoghue, T., Hulscher, S.J., Ribberink, J.S., et al., 2017b. Bedload and suspended load contributions to breaker bar morphodynamics. *Coastal Engineering* 129, 74–92.

Van Der Zanden, J., Hurther, D., Caceres, I., O'Donoghue, T., Hulscher, S.J., Ribberink, J.S., et al., 2017c. Suspended sediment transport around a large-scale laboratory breaker bar. *Coastal Engineering* 125, 51–69.

Van Rijn, L., Ruessink, G., Grasmeijer, B., Van der Werf, J., Ribberink, J., 2007. Wave-related transport and nearshore morphology, *in: Coastal Sediments' 07*, pp. 1–14.

Van Rijn, L.C., 1984. Sediment transport, part ii: suspended load transport. *Journal of Hydraulic Engineering* 110(11), 1613–1641.

Van Rijn, L.C., 2007. Unified view of sediment transport by currents and waves. i: Initiation of motion, bed roughness, and bed-load transport. *Journal of Hydraulic Engineering* 133(6), 649–667.

Van Rijn, L.C., et al., 1993. Principles of sediment transport in rivers, estuaries and coastal seas. Volume 1006. Aqua Publications, The Netherlands.

Van Rooijen, A., Reniers, A., Van Thiel de Vries, J., Blenkinsopp, C., McCall, R., 2012. Modeling swash zone sediment transport at truc vert beach, *in: ICCE 2012: Proceedings of the 33rd International Conference on Coastal Engineering, Santander, Spain, 1-6 July 2012*, Coastal Engineering Research Council.

Veeramony, J., Svendsen, I.A., 2000. The flow in surf-zone waves. *Coastal Engineering* 39(2-4), 93–122.

Van Thiel de Vries, J., 2009. Dune erosion during storm surges. IOS Press, The Netherlands.

Walstra, D., Van Rijn, L., Van Ormondt, M., Brière, C., Talmon, A., 2007. The effects of bed slope and wave skewness on sediment transport and morphology. *Coastal Sediments' 07, New Orleans, USA* , 137–150.

Wenneker, I., van Dongeren, A., Lescinski, J., Roelvink, D., Borsboom, M., 2011. A Boussinesq-type wave driver for a morphodynamical model to predict short-term morphology. *Coastal Engineering* 58(1), 66–84.

Wong, P.P., Losada, I.J., Gattuso, J.P., Hinkel, J., Khattabi, A., McInnes, K.L., Saito, Y., Sallenger, A., et al., 2014. Coastal systems and low-lying areas. *Climate Change* 2104, 361–409.

Xiao, H., Young, Y.L., Prévost, J.H., 2010. Hydro-and morpho-dynamic modeling of breaking solitary waves over a fine sand beach. part ii: Numerical simulation. *Marine Geology* 269(3-4), 119–131.

Young, Y.L., Xiao, H., Maddux, T., 2010. Hydro-and morpho-dynamic modeling of breaking solitary waves over a fine sand beach. part i: Experimental study. *Marine Geology* 269(3-4), 107–118.

Van der Zanden, J., Van Der A, D., Hurther, D., Caceres, I., O'Donoghue, T., Ribberink, J., 2016. Near-bed hydrodynamics and turbulence below a large-scale plunging breaking wave over a mobile barred bed profile. *Journal of Geophysical Research: Oceans* 121(8), 6482–6506.

Zhang, Q., Liu, P.L.F., 2008. A numerical study of swash flows generated by bores. *Coastal Engineering* 55(12), 1113–1134.

Zhu, F., Dodd, N., 2015. The morphodynamics of a swash event on an erodible beach. *Journal of Fluid Mechanics* 762, 110–140.

Zhu, F., Dodd, N., Briganti, R., 2012. Impact of a uniform bore on an erodible beach. *Coastal Engineering* 60, 326–333.

Zijlema, M., Stelling, G., Smit, P., 2011. Swash: An operational public domain code for simulating wave fields and rapidly varied flows in coastal waters. *Coastal Engineering* 58(10), 992–1012.